Development of an enhanced drivetrain model in HAWC2

Thesis report

Simon Lackner

TU Delft

Development of an enhanced drivetrain model in HAWC2

Master's Thesis Report

by

Simon Lackner

Master of Science in Wind Energy

Technical University of Denmark

&

Master of Science in Aerospace Engineering

Delft University of Technology

September, 2025

Thesis Committee:

Chair: Prof. Dr. S. J. Watson, TU Delft - Associate Professor
External examiner: Prof. M. H. Hansen, SDU - Associate Professor
Supervisors: Dr. D. Zappalá, TU Delft - Assistant Professor
D. R. Verelst PhD, DTU - Senior Researcher
Prof. Dr. Y. Guo , Clemson University - Associate Professor

Student Number: TU Delft 6082416, DTU 233828

An electronic version of this thesis is available at
http://repository.tudelft.nl/

"I don’t know where I’m going from here, but I promise it won’t be boring."

— David Bowie

Preface

Two years and four months ago, I did not know where I was going. I made the spontaneous decision to apply for the EWEM Master's program, driven by my stubbornness to pursue a career in the wind energy sector. Returning to university was not an easy choice: I had already completed a Master's degree in Mechanical Engineering and had been working for a while. Yet, after two years, two countries, four different accommodations, thirteen exams, twenty-four assignments, twenty-eight organizational forms, one Master's thesis, and countless sleepless nights, I can confidently say that it was the right decision. I am proud that I took this step, even though it meant leaving behind the comfort and security of my life at that time. More than that, however, I feel deeply grateful to live in an environment where unconventional and economically unwise decisions like this are possible—something I do not take for granted.

For this, I owe my greatest gratitude to my parents, Silvia and Markus, who supported me wholeheartedly from the very beginning. Their encouragement helped me overcome all remaining doubts and gave me the confidence to follow this unconventional path.

I would also like to express heartfelt thanks to Bea, who offered continuous support and belief in me during this journey, despite the challenges and complications this decision brought. Special thanks also go to my sisters and my friends, who never questioned my choice but instead encouraged me to follow my instinct.

Although the past two years were full of exciting discoveries, new experiences, and unforgettable adventures, they occasionally brought me to my personal limits. I am unsure I could have maintained my motivation and energy through these stormy phases without the great team spirit within the EWEM group (and a good amount of coffee). I am sincerely grateful to my study colleagues, new friends, and all the wonderful people I met in Denmark and the Netherlands, who made these two years an extraordinary and unforgettable period of my life.

Finally, I would like to thank my supervisors, David Verelst, Donatella Zappalá, and Yi Guo. They not only provided invaluable academic guidance and expertise throughout this thesis project but also offered encouragement, kindness, and a genuinely supportive atmosphere that made working on this project both enriching and enjoyable.

Abstract

The rapid technological progression of wind turbines not only imposes design challenges but also necessitates continuous advancements in modeling approaches, particularly holistic methods capable of accurately capturing turbine coupling effects. A well-established modeling tool in the wind energy sector is the aero-servo-elastic code HAWC2. Although it is widely used to predict the overall turbine response across a broad range of operating conditions, the drivetrain is typically represented as a single beam.

In the presented work, a more realistic and comprehensive drive train model was developed in HAWC2 to account for additional flexibility effects associated with increasing turbine dimensions and enable the estimation of the main bearing reaction loads. First, a detailed literature review was conducted to analyze current trends regarding drivetrain technology, essential components, and modeling approaches of modern wind turbine drivetrains.

The DTU 10 MW RWT and a high-fidelity SIMPACK drivetrain model, developed by researchers from NTNU, were identified as references for the implementation. Additionally, the theoretical foundations of Timoshenko beam elements and multibody formulation used in HAWC2 were studied, as both are essential for constructing a turbine model in HAWC2. In the implementation phase, the overall drivetrain structure and fundamental drivetrain properties, such as the stiffness properties of the main bearings, were extracted from the SIMPACK model and incorporated into HAWC2 through the introduction of additional beam elements. To further increase the fidelity, the first torsional eigenfrequency of the derived structure was tuned to match the dynamics of the reference models. As a final step, the simple HAWC2 drivetrain representation was adjusted to reflect the mass distribution of the developed structure, enabling a direct comparison between the two.

The developed model showed strong performance in predicting main bearing loads under steady conditions, thereby achieving a clear improvement in fidelity compared with the original setup. In contrast, reduced agreement was observed for the torque arms response and under turbulent simulations. The study concludes with a critical evaluation of the model, addressing its limitations and outlining potential directions for further accuracy improvements.

Contents

Nomenclature

Symbols

Table 1: List of symbols used in this report.

Symbol	Definition	Unit
f	Frequency	Hz
g	Gravity	m/s^2
k	Shear factor	-
$k_{t,eq}$	Equivalent torsional stiffness constant	Nm/rad
l	Length	m
m	Mass	kg
m_s	Mass per unit length	kg/m
n	Rotational speed ratio	-
r	Radius	m
$r_{ix/iy}$	Radius of gyration in x/y-direction	m
s	Curved length distance	m
t	Time	s
x	Spatial coordinate	m
y	Spatial coordinate	m
z	Spatial coordinate	m
A	Area	m^2
A_0	Amplitude	dep.
$C_{x/y/z}$	Longitudinal damping in respective direction	Ns/m
$C_{\alpha/\beta/\gamma}$	Torsional damping about respective axis	Nms/rad
E	Young's Modulus	N/m^2
F	Force	N
G	Shear modulus	N/m^2
I	Area moment of inertia	m^4
I_p	Polar moment of inertia	m^4
J	Mass moment of inertia	kgm^2
K	Polar moment of inertia	m^4
$K_{x/y/z}$	Longitudinal stiffness in respective direction	N/m
$K_{\alpha/\beta/\gamma}$	Torsional stiffness about respective axis	Nm/rad
M	Moment	Nm
R	Radius	m
α	Rotation about the x-axis	°
β	Rotation about the y-axis	°
γ	Rotation about the z-axis	°
δ	Bending deformation	m
Δ	Difference	-
θ	Torsional deformation	rad
θ_z	Structural pitch	rad
ν	Poisson's Ratio	-
ξ	Logarithmic damping coefficient	-
ω	Angular frequency	rad/s

Abbreviations

Table 2: List of abbreviations used in this report.

Abbreviation	Definition
AC	Alternating current
BEM	Blade element momentum
CG	Center of gravity
DC	Direct current
DT	Drivetrain
DFIG	Doubly fed induction generator
DLL	Dynamic Link Library
DOF	Degree of freedom
EOM	Equation of motion
FE	Finite element
FPC	Full power converter
HSS	High-speed shaft
H2	HAWC2
LSS	Low-speed shaft
MB	Main bearing
MBS	Multibody system
PMSG	Permanent magnet synchronous generator
PPC	Partial power converter
RQ	Research question
SP	SIMPACK
TA	Torque arm
TC	Tower clearance
WRIG	Wound rotor induction generator
WRSG	Wound rotor synchronous generator
WT	Wind turbine

List of Figures

List of Tables

Introduction

Wind turbines have experienced rapid technological advancement throughout the past decades. The abundance and free accessibility to the resource wind, the flexible deployment, and the environmental benefits of wind power have led to a significant increase in global demand. Not only has this development led to a successive boost in installed turbines worldwide, but it has also resulted in a continuous growth in turbine size as shown in Figure 1a and Figure 1b[1][2][3].

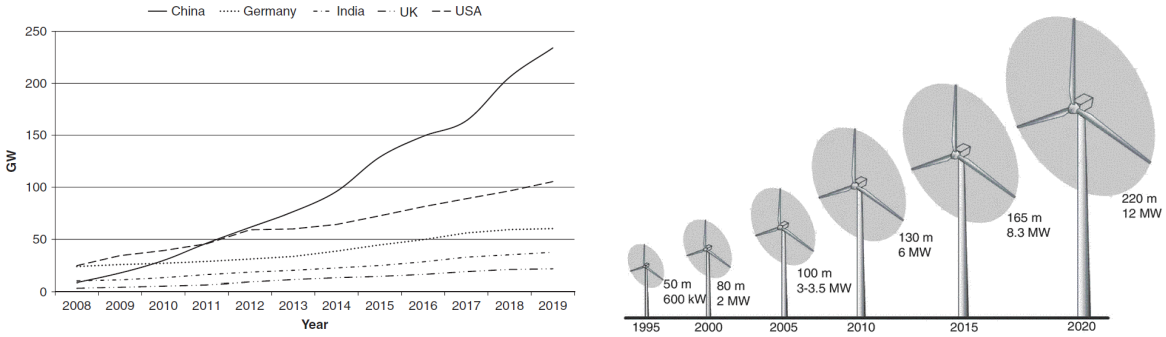

(a) Wind power capacity trends for selected countries.

(b) Development of wind turbine sizes.

Figure 1: General trends in the wind energy sector [3].

Among other factors, the following four drivers have contributed — and are likely to continue contributing — to an increase in dimensions. First, the cubic dependency of the power on the wind speed, and the gradually increasing wind speeds with the distance to the ground, make higher hub heights desirable. Second, the power output has a quadratic dependency on the rotor diameter. Third, using larger machines, the same power capacity can be achieved using fewer turbines. Consequently, less space is required and the overall installation effort is reduced, even if the handling of large single turbines gets more complicated. Lastly, the emerging offshore market fosters the development of large multi-MW turbines due to the relaxed space and transportation constraints [3].
These factors have led to a significant reduction in costs per installed wind capacity [4]. However, the trend to develop larger rotor diameters entails various new challenges regarding competitiveness, transport, and engineering, leading to a continuous debate about optimal wind turbine dimensions [3].
One engineering-related challenge deals with the question of how to simulate multi-MW turbines accurately and efficiently. Modeling the entire turbine with high-fidelity methods, such as FE or CFD software, is not feasible in an industrial setting, especially in early product development stages. Compromises must be made between reliability and computational cost. Consequently, in the iterative development of a wind turbine, various calculation tools are required, each being designed for a specific discipline, and each building on the results of the others. Moreover, as turbine dimensions and performance requirements continue to grow, modeling entire systems becomes increasingly complex [5]. It is therefore crucial to continuously advance existing modeling tools.

Relevance

HAWC2, a versatile aero-servo-elastic code developed at the Technical University of Denmark (DTU), is one of the primary tools used to simulate the overall wind turbine response in the time domain under different operational conditions. As such, it is widely employed in academia, as well as for wind turbine certification and industrial applications, where the resulting load estimations serve as input for higher-fidelity, component-specific design tools [6]. This master's thesis focuses on developing an enhanced drivetrain representation within HAWC2, thereby aiming to improve the fidelity of its simulation results. Apart from the importance of continuously upgrading existing tools, additional aspects related to current turbine trends further underline the relevance of this work.

Component flexibility

The importance of modeling the entire turbine as a coupled system due to the dynamic interaction between the different components is underlined in [7]. Since turbines operate under a wide range of external conditions and are subjected to a stochastic environment, the whole structure needs to be well synchronized. Holistic modeling tools are therefore essential to guarantee a smooth operation, minimize loads and optimize the energy yield. As turbines grow in size, the structural flexibility of their components increases, and design margins decrease [5]. As a consequence, in applications that aim to model the entire turbine, structural simplifications and assumptions made for smaller turbines are no longer valid [4][8]. Although research has shown that its contribution to the overall system's dynamics is significant, the drivetrain is often modeled in a simplified way. A prominent example is the DTU 10 MW RWT as discussed in [9].
In HAWC2, usually, a simple beam model is used to represent the entire drivetrain. Especially with components becoming bigger, this inadequately captures the true characteristics and neglects the complex interdependencies between the rotor, drivetrain, and tower.

Load predictability and lifetime optimization

With turbines getting bigger, they are also becoming increasingly valuable assets, making it more crucial to meet design lives or even extend lifetimes [4]. However, it has been noticed that larger turbines entail increasing failure rates in drivetrain components, leading to higher O&M costs [10]. In this context, improvements in mapping the overall structural dynamics lead to insights that are beneficial for the stability analysis of the turbine and consequently help avoid harmful operational conditions [5]. Moreover, experience in operating large-scale wind turbines, especially in harsh environmental conditions, is limited, and some of the standards used are outdated and no longer sufficient [4].
In light of these considerations, a deeper understanding of the entire turbine and the interdependencies among its various components is essential, and further insights into coupling effects are important for the ongoing development of modern wind turbines. This master's thesis aims to address specific gaps in the modeling of drivetrain dynamics coupled with aero-servo-elastic simulations and seeks to improve the accuracy of load predictions, thereby contributing to a more reliable basis for component-level design. By refining the representation of the HAWC2 drivetrain model, the work is intended to provide a foundation for a better analysis of the turbine performance under realistic operational conditions and to assist in the optimization of future turbine designs.

Main Goal and Research Questions

Building on this context, this section outlines the specific research goals of the thesis, highlighting the questions and objectives that served as guidelines for the development and implementation of the enhanced drivetrain modeling approach. As initially indicated, the main goal of this study is the:

Development of an enhanced drivetrain model in HAWC2 to enable the analysis of drivetrain loads, with a particular focus on the main bearing loads, and to more accurately capture dynamic coupling effects in modern wind turbines.

From this main objective, several research questions (RQ) were derived and iteratively adjusted throughout the entire project phase. They are presented below. The first question aimed to develop a deeper understanding of the most relevant drivetrain components, providing the necessary competence to carry out the project. RQ 2 served to identify a suitable reference model during the preparation phase, while RQs 3-I to 3-V guided through the implementation steps of the project (see section 3). The concluding questions RQ 4-1 and RQ 4-2 address the results and the quality of the developed drivetrain model and are answered in section 4. They are designed to link directly back to the project's main goal.

RQ 1 What are the prevailing trends, essential components, and their key characteristics in modern wind turbine drivetrains, and what modeling approaches exist to represent them?

RQ 2 Which turbine and drivetrain models provide the most suitable reference for developing an enhanced HAWC2 drivetrain representation, and what criteria justify this choice?

RQ 3-I How can the drivetrain structure of the selected SIMPACK model be represented in HAWC2 using Timoshenko beam elements while capturing the dynamic behavior at key drivetrain locations?

RQ 3-II Which method can be applied to translate geometric and material parameters from the reference model into HAWC2?

RQ 3-III How can stiffness and damping properties of principal drivetrain joints be integrated into the HAWC2 representation to maintain its dynamic behavior?

RQ 3-IV How can the original, simplified HAWC2 drivetrain model be adjusted to enable a comparison with the newly developed model?

RQ 3-V How can the HAWC2 drivetrain models be calibrated to match the first torsional eigenfrequency of the reference models?

RQ 4-1 How accurately can the developed model determine the main bearing loads under different inflow conditions compared with the reference model?

RQ 4-2 To what extent does the enhanced HAWC2 drivetrain representation influence the overall turbine response compared with the simplified configuration?

Thesis Structure and Project Workflow

To support an efficient and strategic workflow, the thesis project was structured into four main phases: 1. the Initialization and Research phase, 2. the Model Preparation phase, 3. the Model Implementation phase, and 4. the Model Verification phase.
During the first phase, a detailed literature study was carried out to acquire fundamental background knowledge needed for a successful project execution. It is presented in section 1.
The model preparation phase focused on identifying reference models, defining the project framework, and gaining familiarity with the required software tools and underlying theoretical concepts. section 2 is dedicated to these contents.
Subsequently, the Implementation phase was subdivided into five stages, each representing a crucial contribution to the development of a more realistic enhanced drivetrain model within the HAWC2 environment. Each of these implementation steps is described in detail in the main part of this report, in section 3.
In section 4, the developed model is analyzed and compared with the reference model and with the simple, original HAWC2 drivetrain representation. Finally, the report concludes with a summary of the main findings and an outlook on future work. A visualization of the project workflow is given by Figure 2 on the next page.

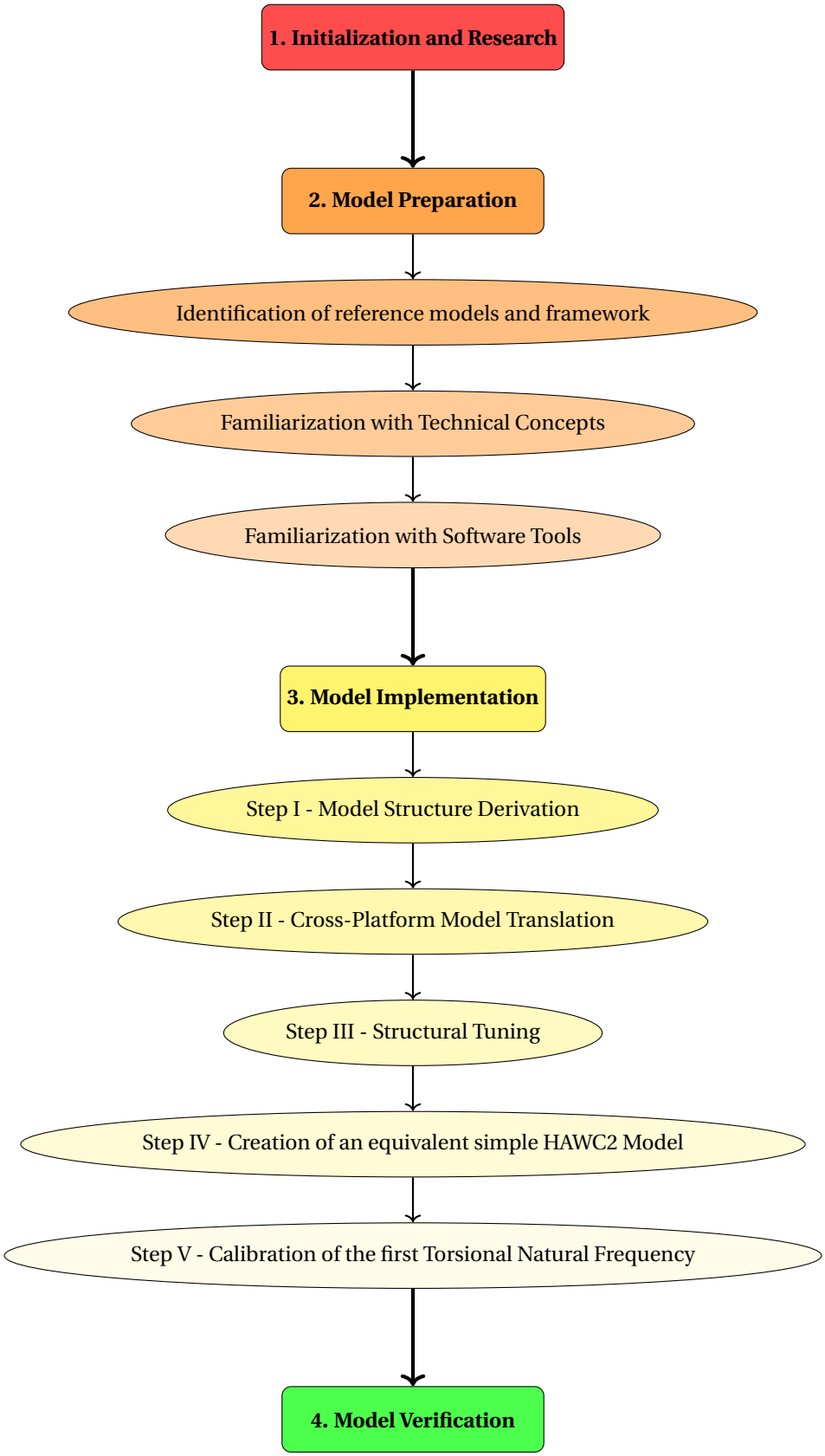

Figure 2: Flowchart of project work flow.

1. State-of-the-art/Literature Review

The drivetrain plays a key role in a wind turbine, being responsible for converting the rotor's kinetic energy into electrical power. This section provides an overview of recent advancements in drivetrain technology for modern, variable-speed wind turbines and aims to answer research question RQ 1. Furthermore, it examines the major components that significantly contribute to turbine coupling effects, highlighting their functions and specific characteristics. Finally, existing approaches for modeling wind turbine drivetrains are presented.

1.1. Overview of most common Types of Drivetrain Configurations

As previously mentioned, the drivetrain converts mechanical power into electrical power and therefore transmits the rotor loads to the generator. However, since not all rotor loads contribute to generating electricity, some loads are transmitted to the structure of the turbine (bedplate and tower). A schematic drivetrain setup is shown in Figure 3. It includes the rotor, the low- and high-speed shafts, the main bearings, the gearbox, a mechanical brake, the generator, the power converter, and the bed frame. The drivetrain is located on a bedplate in the nacelle, which connects to the tower top through the yaw system [3][4].

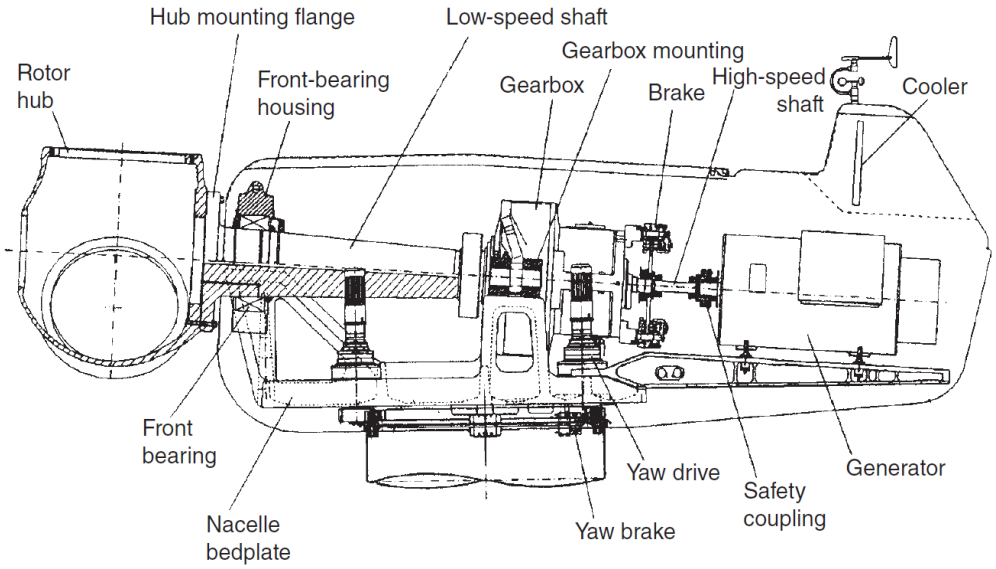

Figure 3: General drivetrain scheme [3]

In general, the most common drivetrain configurations can be divided into two main categories, with, and without gearbox (see Figure 4). While turbines with gearboxes have been dominating the designs for many years, it has become increasingly popular to implement drivetrains without gearboxes, also referred to as direct drive machines. Recently, combinations of these two layouts and other special configurations have been developed. The hybrid designs usually have a smaller gearbox and a medium-speed generator. Although they can be scaled better for larger powers, they entail the disadvantage of having a gearbox that can fail and an expensive custom-made generator [3][11].
According to [4], it has also become a trend to increasingly integrate main components into the structure to reduce mass and therefore costs. Figure 4 shows the two most common drivetrain configurations. In both cases, the hub is connected to the low-speed shaft, and the wind energy is converted into electrical energy. Eventually, the generated electricity can be transmitted into the grid using a power converter and a transformer. In each of these conversion stages, some energy is lost due to mechanical friction, electrical losses, and electromagnetic losses [11]. Below, the two conventional designs are discussed in more detail.

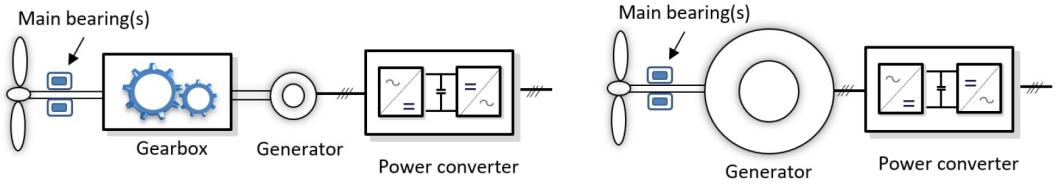

(a) Drivetrain with gearbox.

(b) Drivetrain without gearbox: direct drive.

Figure 4: Schematic of the two most common types of drivetrain configurations [4].

Drivetrain with Gearbox

The traditional drivetrain design includes a gearbox and a high-speed generator (see Figure 4a). These generators are usually off-the-shelf products and operate at 1000 or 15000 rpm. Since the rotor speed is usually approximately 100 times lower, a two- or three-stage gearbox is used to step up the speed. The advantages of this layout are the evolved technology, the possibility to use common generators, and relatively small and therefore lighter components. However, gearboxes require frequent maintenance and are a potential source of failure [11].

Direct Drivetrain

Direct-drive machines, as depicted in Figure 4b, avoid the employment of gearboxes by using large, low-speed generators that are directly connected to the hub. This is expected to enhance the reliability of the drivetrain, reduce losses, noise and maintenance costs [3]. Therefore, this configuration is increasingly popular for offshore applications. The downside is that the generators used are typically custom-made, heavy, and expensive, leading to increased installation challenges [3][11].

1.2. Drivetrain Components

Low-speed Shaft and Main Bearing(s)

The main bearing(s) support and hold the hub or the low-speed shaft in place. Their role is to absorb external forces and transfer them to the housing and the bedplate to avoid the transmission of non-torque loads to the gearbox. These external forces and moments can be radial or axial and are caused by the weight of the rotor and the shaft, as well as by the loads emerging during operational conditions. Generally, a minimum of two bearings is necessary to absorb all loads. One is commonly a fixed bearing, taking up both forces in vertical and longitudinal direction, and the remaining bearings absorb radial forces only. The resulting degree of freedom ensures that shaft deformations caused by thermal expansion do not cause additional tension [11][12]. The number of main bearings used and their location depend on the drivetrain architecture. Direct-drive wind turbines are characterized by a compact design and typically do not have a slow-speed shaft. Instead, a large bearing carries the hub directly. The most common drivetrain configurations with a gearbox, on the other hand, have a three-point, or sometimes a four-point suspension [13]. In both cases, the main shaft is rigidly connected to the rotor on one side and to the low-speed stage of the gearbox on the other end. Two arms on each side connect the gearbox elastically to the bedplate, absorbing moments in the axial direction. These two arms, together with either one or two main bearings, create a three-point or a four-point suspension, respectively. Below, in Figure 5, a schematic representation of both support types can be seen. The additional bearing in Figure 5b serves to isolate the gearbox from non-torque rotor loads upwind. However, the use of two main bearings makes the structure more sensitive to deformations and tolerances in the assembly due to the overconstrained mechanical system [11][14].

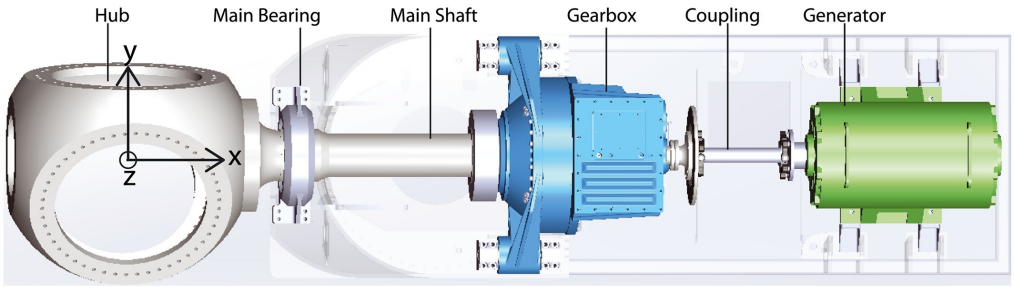

(a) Three-point support.

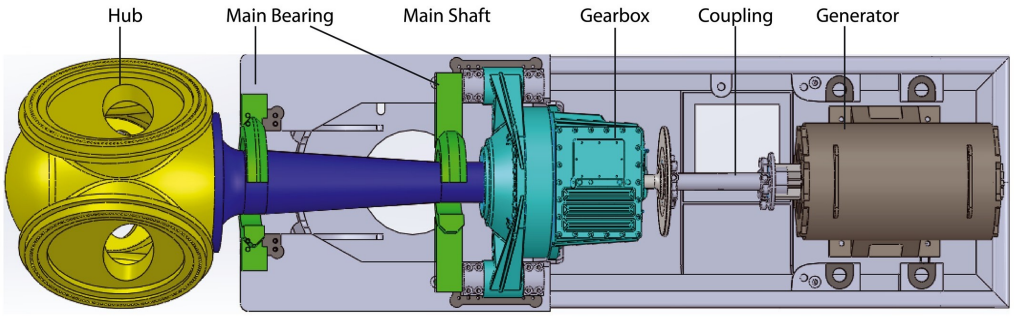

(b) Four-point support.

Figure 5: The two most common suspension types for wind turbine drivetrains with gearbox [14].

Research is done on various bearing technologies, yet rolling-element bearings are well established on an industrial level and are expected to maintain this rank. Their increasingly large diameters are only limited in size by manufacturing and transportation constraints. Moreover, their support structure is more flexible and cheaper than other technologies, such as hydrostatic, air, or magnetic bearings. While spherical bearings dominate in sub-5MW applications, tapered roller bearings are advantageous for larger machines. In [12], their capability of withstanding high radial and axial loads is highlighted. This is beneficial for the absorption of large non-torque loads in multi-MW turbines [4].
Despite being a mature technology with well-established standards, main bearings show alarming high failure rates of up to 30 % during the design life and are considered among the most vulnerable elements in a wind turbine [15]. Research has shown that during operation, frequent, large-scale load fluctuations occur, issues that are amplified when bearing diameters and hence deflections increase. These unwanted loads are not accounted for in conventional life assessments and potentially result in harmful roller skidding, surface fatigue, wear, and abrasion [16]. Another consequence of larger turbines is that main bearings are increasingly integrated into the structure as a load-carrying component. For certain direct drive architectures, the main bearing has to support the generator rotor in addition to the turbine rotor, while maintaining an acceptable generator air gap [4].
This underscores the necessity to revise existing standards, especially for large wind turbine applications, as well as the urgency to find methods to improve the understanding of wind turbines as a coupled system in order to ensure long design lives [4].

Gearbox

Gearboxes are used to convert the low-speed, high-torque rotation of the rotor shaft into a high-speed, low-torque input suitable for conventional generators. This enables the use of smaller and cheaper generators compared to direct drive turbines [11]. However, gearbox stages are designed to transmit torque and rotational speed only. They are very sensitive to non-torque loads, which cause uneven strains or sudden impacts and reduce the reliability significantly [13]. This makes them a vulnerable component and a potential source of failures. Additionally, gearboxes entail significant losses due to mechanical friction and require monitoring and frequent maintenance [14][16].
Conventional turbines use gearboxes with two or more stages and a transmission ratio of up to 200. Depending on the size and the requirements, usually, one or two planetary stages are used on the low-speed side (LSS) and one parallel stage on the high-speed shaft (HSS) [11]. Planetary gears are characterized by coaxial

shafts and a symmetrical force distribution on the main shaft. Due to the three (or more) points of contact, they are more suitable for lower speeds and higher torques. Even peak loads caused by sudden changes in the driving torque are distributed uniformly [17]. At higher speeds, friction becomes more relevant and the torque is lower. Therefore, the single point of contact of parallel stages becomes favorable [11].
Figure 6 shows the schematic setup of a wind turbine gearbox with three stages, two planetary stages on the left, and one parallel stage on the right side.

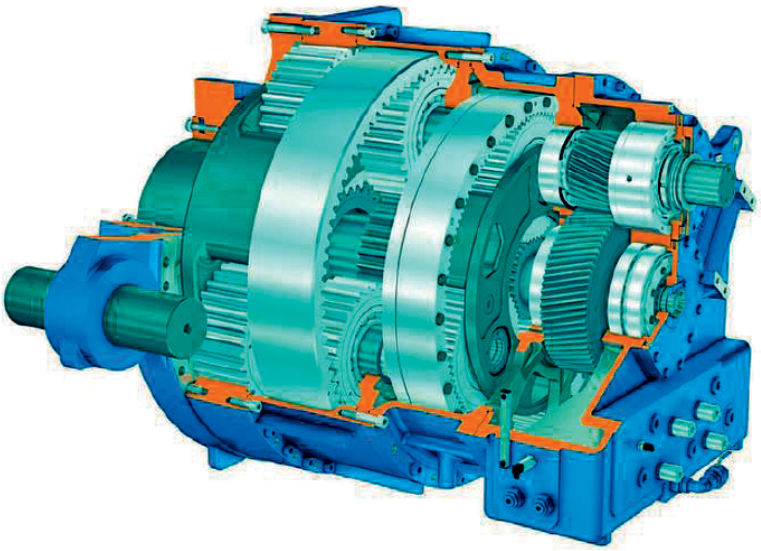

Figure 6: Scheme of a three-stage gearbox: planetary-planetary-parallel [18].

Gearboxes face growing demands due to increasing turbine sizes. Apart from the bigger gearboxes themselves, larger rotors and lower rotor speeds require a higher torque density and higher transmission ratios. The scaling also involves an increase in flexibility and requires a more detailed (finite-element) analysis of the effect of deformations and dynamics on internal loading. Gearboxes are complex systems that consist of many different machine elements, such as shafts, gears, bearings, and seals, which are all subject to standardized reliability calculations. Similar to the main bearings, these calculations do not cover all operational modes that compromise the component's lifetime. Recently, it has become increasingly popular to develop modular designs that facilitate scaling and the replacement of single parts, reducing maintenance costs and downtime [4].

Generator and Power Converter

Wind turbines typically use three-phase generators with a fixed stator and a rotor that is mechanically attached to the rotating shaft. The general principle of all generators is to generate electrical power through the interaction between the magnetic fields of the rotor and the stator. However, there are four main types, differing in the mechanism of how the rotor's magnetic field is generated [11]:

- Permanent magnet synchronous generator (PMSG): The magnetic field is created by the magnetism of the material.
- Electromagnetic synchronous generator: The magnetic field is created by a coil carrying direct current.
- Induction generator or squirrel cage generator: A magnetic field is induced by the rotating magnetic field of the stator.
- Doubly fed induction generator (DFIG): Uses the induction principle, yet with a more complex configuration.

As mentioned previously, while the rotor speed in drive train layouts with a gearbox is high enough to use conventional generators, the rotational speed ω in direct drive machines is very low and requires the

use of custom-made devices. Therefore, a much larger torque Q has to be applied to obtain the same power P ($P = \omega Q$). This is realized by increasing the dimension and by using higher currents. As a result, these generators are very large, heavy, and expensive [11].
Since all large modern wind turbines operate at variable speed, power converters are necessary to maintain a constant output frequency for the grid. This is achieved by using two back-to-back voltage source converters and by transforming the power into direct current (DC) first, and then back into AC with the required grid frequency. The conversion is either done for all the power (Broad range or full power converter (FPC)), or for a fraction of the electrical rotor frequency only (Narrow range or partial power converter (PPC)). Figure 7 compares the working principle of both conversion types. While the former concept is applicable for both synchronous and induction generators, the latter can only be used in combination with a DFIG. PPCs have lower losses and a more compact design. However, their operational speed range is restricted to ±30–40% of the synchronous speed, whereas FPCs perform effectively across the entire operational range [18][19].

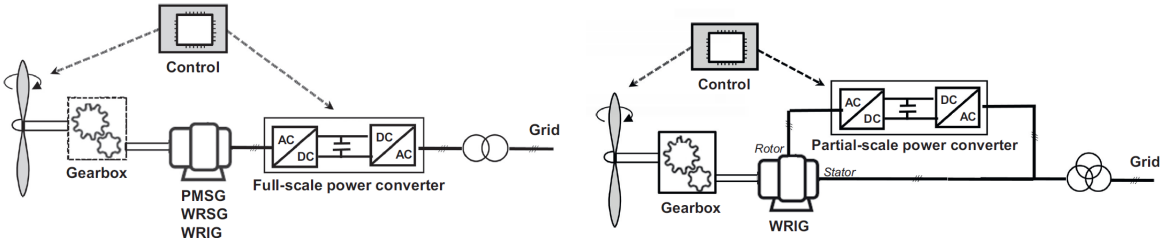

(a) Full power converter [19]. **(b)** Partial power converter [19].

Figure 7: Most common wind turbine power conversion types.

Recent developments show that, despite concerns over the usage of rare-earth materials, permanent magnet synchronous generators with FPC are gradually replacing doubly fed induction generators with PPC systems. More exotic direct drive designs that avoid the use of rare-earth materials employ superconducting generators [4]. Due to the efficiency of their wires, which minimizes heat losses and reduces cooling requirements, higher currents can be applied. This configuration is more suitable for upscaling. However, maintaining the superconducting regime requires the operation at extremely low temperatures [11].
The use of large generators creates challenges not only regarding transportation and installation. Additionally, optimized synchronization and interaction with the other drivetrain components are becoming increasingly important to ensure smooth operation and system reliability. For example, it must be ensured that the generator air gap stays within acceptable limits during operation [4].

Mainframe

The mainframe or bedplate is the combining structure of the drivetrain, guaranteeing its correct and precise alignment [3]. In addition, it transmits the weights and loads of the rotor and the drivetrain to the yaw bearing and the tower and is therefore crucial for the functionality of the entire system [3][4].
The exact configuration of the bedplate depends on each design and can occur in multiple variations. Traditionally, it consists of two parts. The upwind frame carries the main load, resulting from the rotor, the slow-speed shaft main bearings, and sometimes the gearbox [18]. The use of cast iron allows for optimizing the design, regarding load paths and weight [3]. The downwind part is typically lighter and welded. It supports the generator, sometimes the gearbox, and potentially power-converting electronics. In Figure 3, the bedplate consists of two sections that are connected just below the yaw drive. In some layouts, the gearbox frame and the bedplate are combined into one single unit [3][11].
To withstand all standstill and operational loads and keep the mass low at the same time, the bedplate has to be optimized. This means, a compromise between a rigid, yet heavy and expensive, and a more flexible but lighter bedframe has to be found [18]. Modern wind turbine designs tend to have a compact frame structure to minimize the mass [3][11].
The determination of extreme loads and fatigue loads is necessary for the dimensioning of the bedplate. This typically requires a combination of different calculation software. A global load analysis capable of including coupled effects is a prerequisite for more advanced, higher fidelity tools such as FE methods that capture the complexity of the structure and the occurring loads [3][8].

In [8], Wang et al. discovered that the increasing flexibility of the bedplates influences load effects on drivetrain components, and its consideration is therefore crucial for the fidelity of a model. According to [8], the inclusion of bedplate flexibility in holistic wind turbine models could also be beneficial regarding computational costs.

Other Drivetrain Components

Further drive train elements include power electronics, couplings, mechanical brakes, lubrication, and other standard machine parts [3][18]. Although being crucial for the functionality of the drivetrain, they are not discussed in this study, either due to their simplicity or because they are expected to have a limited effect on the overall wind turbine dynamics and are not included in the implemented HAWC2 model.

1.3. Existing Drivetrain Models

As mentioned in the introduction, wind turbine design involves the cooperation of a wide range of engineering fields, and each of them typically relies on its own design tools. As a consequence, a combination of different software is necessary to model an entire turbine accurately, and compromises between the level of accuracy and computational costs have to be made [5]. In general, common aerodynamic codes such as HAWC2, FAST, Bladed, Flex5, or AdWiMo can be used to represent drivetrain designs with varying levels of complexity. However, they often compromise drivetrain-specific properties, as their primary focus lies on the overall turbine response [20]. This section presents insights into a selection of methods for modeling wind turbine drivetrains in a more detailed way.

As described above, drivetrains are complex structures that occur in various configurations. Several approaches with different levels of detail and fidelity exist for describing them. According to [21], most of the models employed are modal-based, finite element codes, multibody formulations, or a combination of them. Although high-fidelity simulations for the entire turbine are possible, these models are computationally too expensive for the design of control systems [5].

Different research has been done on designing and modeling drivetrain layouts. One approach to implement a more detailed model includes the DrivetrainSE (formerly DriveSE) model, a physics-based representation of key drivetrain components such as the shaft, bearings, gearbox, and bedplate. DriveSE is part of the WindPlant Integrated System Design & Engineering Model (WISDEM), and is capable of optimizing designs under structural and weight constraints based on standardized load cases. It is further used to deliver information used in turbine and cost models [14].

In 2014, Guo et al. discussed different modeling approaches for a newly developed drivetrain design aimed at minimizing non-torque loads on the gearbox. In this context, the so-called Alstom's Pure Torque drivetrain concept was modeled with an analytical approach and by using a high-fidelity model implemented in SAMCEF (see Figure 8). SAMCEF is a nonlinear dynamic FE multibody software that enables detailed investigation of the drivetrain structure. The results were compared with experimental data, leading to the conclusion that a realistic drivetrain modeling approach is essential for accurately capturing its dynamics and the coupling effects with the rest of the turbine [13].

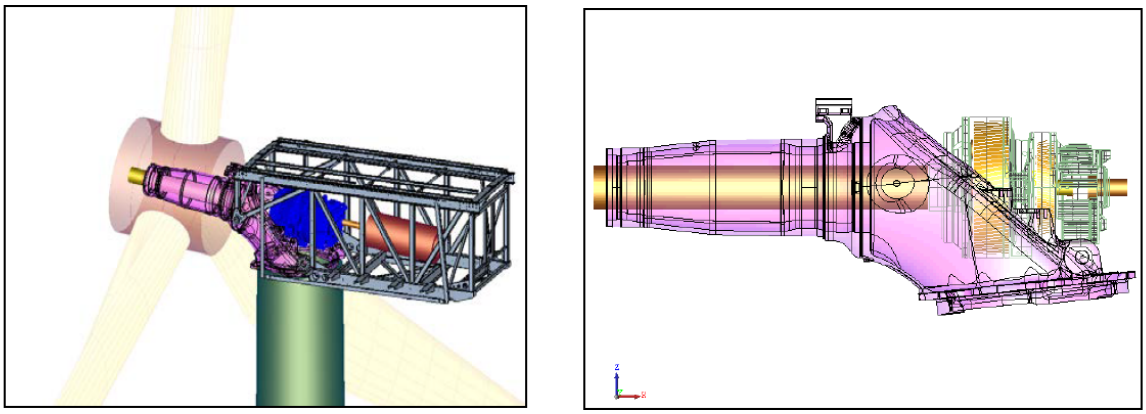

(a) The embedded drivetrain concept.

(b) The detailed drivetrain design.

Figure 8: SAMCEF model of Alstom's ECO100 wind turbine [13].

Another modeling approach is described in [9] and in [22], by Wang et al. in 2019 and 2020, respectively. They developed a detailed four-point support, medium-speed drivetrain model, designed for the DTU 10MW Reference Turbine [22]. To obtain an optimized layout, regarding total mass and reliability, different designs were compared, and a high-fidelity numerical model in SIMPACK was developed. Additionally, a detailed load and resonance analysis was carried out, and both a global turbine simulation and a decoupled drivetrain analysis were performed [9][22]. The SIMPACK model also served as a guideline for this thesis and is discussed in greater detail in the following sections.
In 2024, Krathe et al. published a paper, where they explain how this high-fidelity SIMPACK model was used to develop a more realistic drivetrain structure in the aerodynamic simulation tool OpenFAST. Similar to the presented work, Krathe et al. aimed to develop a model capable of estimating main bearing loads and improving the accuracy of the drivetrain's elasticity properties [23].

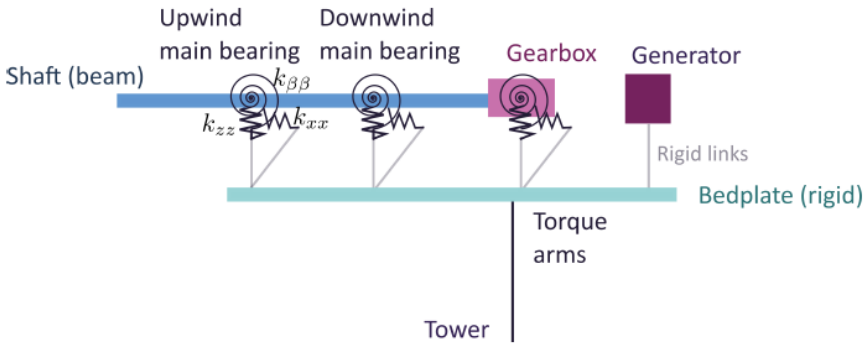

Figure 9: Schmatic concept of the OpenFAST model developed by Krathe et al. [23].

2. Methodology

After the literature review and the formulation of research questions as part of the initialization phase, the next step was the model preparation phase (see Figure 2). In this stage, as part of the setup organization, an appropriate reference turbine and the framework conditions for the simulations were determined. Furthermore, the SIMPACK drivetrain model was identified as an adequate baseline for the development of an enhanced HAWC2 drivetrain model, and its use for this project was authorized by its developers. Hence, this section provides answers to research question RQ 2. Simultaneously, this phase involved getting familiar with the relevant theoretical concepts and gaining practical experience with the required software, in particular with HAWC2, SIMULINK, and SOLIDWORKS.

2.1. Reference models and framework

Reference Turbine

A key aspect of this research study is to establish a well-defined framework. In this case, that involves selecting an appropriate reference wind turbine with a comprehensive dataset that serves as a baseline. Several core requirements for a suitable reference turbine are identified. They include the accessibility of detailed turbine and drivetrain data sets, documentation, and HAWC2 files. Second, simulating a land-based turbine is preferred, as it eliminates the need for additional hydrodynamic calculations and reduces the risk of unforeseen side effects. Third, given the goal of developing an enhanced drivetrain model, it is reasonable to implement a common configuration, which also enables the use of well-documented conventional off-the-shelf components. Additionally, a multi-MW turbine is preferred to investigate the impact of large, flexible components. Lastly, the existence and availability of a high-fidelity drivetrain model are beneficial for comparison and model verification.
Publicly available data exists for several reference turbines [6, 24]. Yet, some were considered outdated or did not meet all the requirements outlined above. The documentations of the IEA reference turbines provide a detailed drivetrain description (see [25][26][27]), yet the DTU 10MW Reference Turbine was found to be more suitable for this study [28]. First, it fulfilled the identified criteria, and second, being developed by DTU, it provided direct access to the researchers involved in the reference turbine's development.
While the DTU 10 MW turbine was primarily designed by upscaling the NREL 5MW reference turbine and applying standard similarity rules, emphasis on developing a light rotor dominates the structure of the blades [28][29]. The DTU 10MW is designed as an offshore turbine, yet a land-based model can be obtained by adjusting the input parameters. Required data that is not accessible may necessitate additional assumptions. The key parameters of the DTU 10MW turbine are presented in Table 3.

Table 3: Key parameters of the DTU 10 MW Reference Wind Turbine [28].

Parameter	DTU 10MW RWT
Wind Regime	IEC Class 1A
Rotor Orientation	Clockwise rotation - Upwind
Control	Variable Speed
Collective Pitch	Same
Cut-in wind speed	4 m/s
Cut-out wind speed	25 m/s
Rated wind speed	11.4 m/s
Rated power	10 MW
Number of blades	3
Rotor Diameter	178.3 m
Hub Diameter	5.6 m
Hub Height	119.0 m
Drivetrain	Medium Speed, Multiple-Stage Gearbox
Minimum Rotor Speed	6.0 rpm
Maximum Rotor Speed	9.6 rpm
Maximum Generator Speed	480.0 rpm
Gearbox Ratio	50
Maximum Tip Speed	90.0 m/s
Hub Overhang	7.1 m
Shaft Tilt Angle	5.0 deg.
Rotor Precone Angle	-2.5 deg.
Blade Prebend	3.332 m
Rotor Mass	227,962 kg
Nacelle Mass	446,036 kg
Tower Mass	628,442 kg

The developed reference turbine and the corresponding HAWC2 model do not contain a detailed description of the drivetrain layout [28]. Instead, one simple beam is used to represent the nacelle and the bedframe, and one to model the rotating part of the drivetrain, i.e., the generator, the gearbox, and the main shaft. The masses and moments of inertia are lumped and assigned to their respective positions. This configuration is represented by the tower top and the shaft in Figure 10. The illustration was created with the help of the HAWC2 Visualization tool and shows the model setup with Timoshenko beams. More information about this modeling approach will be provided later in this section as well as in subsection 3.2. The black lines in Figure 10 denote the beam elements, black dots represent their nodes, and colored lines indicate the local coordinate systems, thereby identifying the first node of each main body.

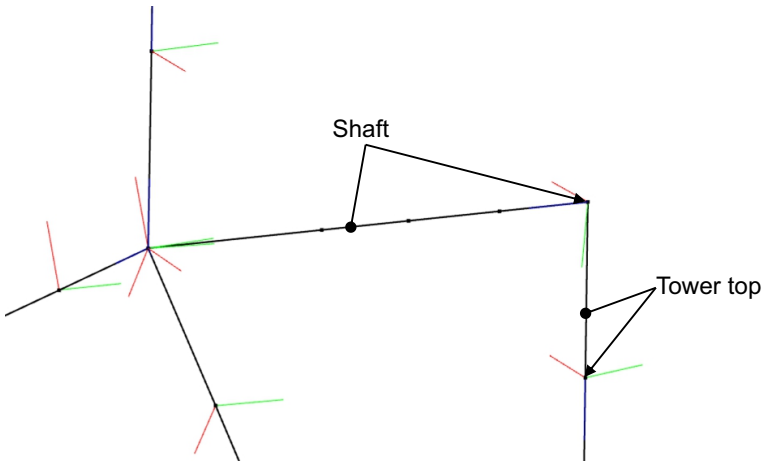

Figure 10: Original drivetrain implementation for the DTU 10MW RWT.

However, as indicated in the literature study, Wang et al. developed a high-fidelity, medium-speed drivetrain model adapted for the DTU 10 MW RWT. The corresponding SIMPACK model served to complete all requirements for this project [9][22].

Drivetrain model

The baseline drivetrain model from Wang S., Nejad A., and Moan T., as described in [9] and [22], represents a standard layout for multi-MW turbines. It employs a four-point support, consisting of two main bearings and two torque arms, and a gearbox with two planetary stages and one parallel stage. The transmission ratio of the medium-speed design is approximately 1:50, reducing the risk of gearbox failure in the high-speed stage and lowering the generator size compared to a direct drive machine. The key parameters are presented in Table 4. Apart from the gearbox which is designed following the IEC 61400-4, the powertrain design is inspired by the 2 MW land-based wind turbine, formerly developed by Wang et al. [30]. A lifetime of 20 years is assumed and all components are weight-optimized while complying with international design standards for both fatigue and ultimate loads under normal operating conditions [9][22].

Table 4: Key parameters of the reference drivetrain [9].

Parameter	Value
Drivetrain type	4-point support
Gearbox type	2 planetary & 1 parallel
First stage gear ratio	1:4.423
Second stage gear ratio	1:5.192
Third stage gear ratio	1:2.179
Total gear ratio	1:50.039
Designed power	10 MW
Rated input shaft speed	9.6 rpm
Rated generator shaft speed	480.374 rpm
Total gearbox dry weight	60 430 kg
Maximum gearbox outer diameter	3.098 m
Service life	20 years

Using the multibody system (MBS) simulation tool SIMPACK, a high-fidelity numerical model was established where rigid and flexible bodies are connected with SIMPACK-Joints and SIMPACK-Forec Elements. The implemented model is shown in Figure 11 and can be used to carry out dynamic analysis of the drivetrain [9].

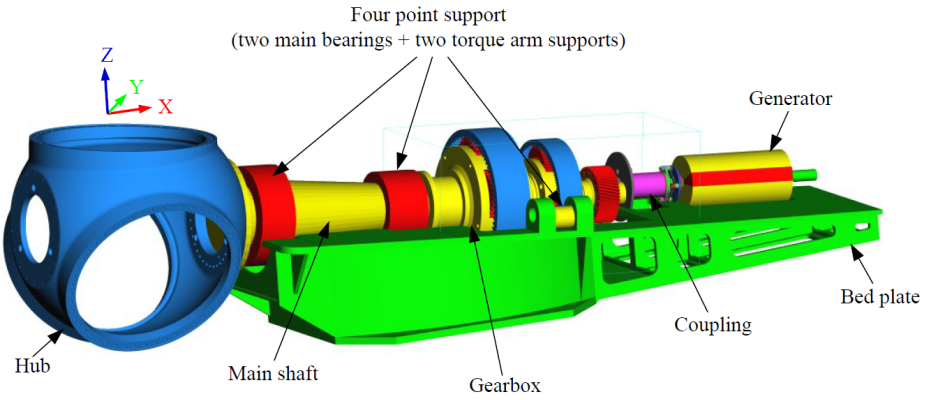

Figure 11: Geometric representation of the SIMPACK drivetrain model [9].

The corresponding MBS interconnections of the different components and their degree of freedom (DOFs) are illustrated in the topological diagram in Figure 12. To achieve a realistic representation of the natural drivetrain properties, the main shaft, the planet carriers, and the transmission shafts in the gearbox are modeled as flexible bodies. The remaining components are considered rigid.

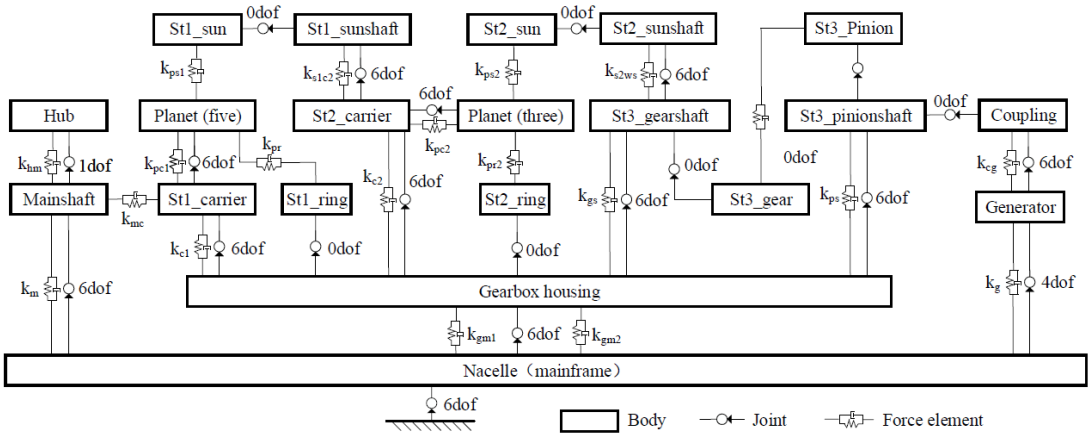

Figure 12: Topological representation of the SIMPACK drivetrain model [9].

To validate this detailed drivetrain architecture against the simple two-mass equivalent mechanical model applied in the DTU 10MW turbine, their first-order torsional eigenfrequencies were compared, and good agreement was observed [9][22]. Further model specifications are provided across the implementation steps in section 3.

Environmental conditions

Wind turbines are typically designed for a specific wind turbine class, as defined in the IEC 61400-1 standard [31]. As indicated in Table 3, the DTU 10MW RWT is designed for the IEC class IA, meaning a high annual average wind speed of 10 m/s and high reference turbulence intensity of 0.16. For the purpose of this study, mainly steady wind simulations were used for the model evaluation. Furthermore, according to the standard, one simulation for normal operational conditions was carried out (se section 4).

2.2. Theoretical Concepts

This study primarily focuses on implementing an enhanced drivetrain model within HAWC2 using Timoshenko beams. This section introduces the theoretical concepts behind Timoshenko beams and the multibody approach used in HAWC2.

Timoshenko beam theory

HAWC2 incorporates a multibody formulation that allows subbodies to be be divided into several substructures. These substructures are represented by one-dimensional Timoshenko beam elements [7]. As the main approach for this project, they are used to build an enhanced drivetrain model and integrate it into HAWC2. Timoshenko beams, also called thick, or shear-flexible beams, add complexity to the shear-rigid Euler–Bernoulli beam theory, which assumes that the cross-sectional planes are fixed to the center line of the beam and remain unchanged if this line is deformed. This assumption, however, only holds for very thin, homogeneous beams. In contrast to this, Timoshenko beams also include shear deformation in the bending deformation. Furthermore, the rotational effects of the cross-sectional planes are included, making Timoshenko beams a more realistic representation for thick beams or under dynamic loading [7]. Figure 13 shows how the Euler–Bernoulli beam can be superimposed with shear deformation to obtain the Timoshenko beam [32]. In this illustration, the bending moment M causes the displacements u_x, and u_y in the respective directions x and y, and φ_z is the angular rotation of the cross-sectional plane with respect to the undeformed section. Further describes the angle γ_{xy} the rotational deformation of the cross-sectional planes due to the shear force Q. In the Timoshenko beam, the combination of the shear angle γ_{xy} and the angle due to pure bending deformation φ_z defines the resulting deformation angle ϕ_z [32].

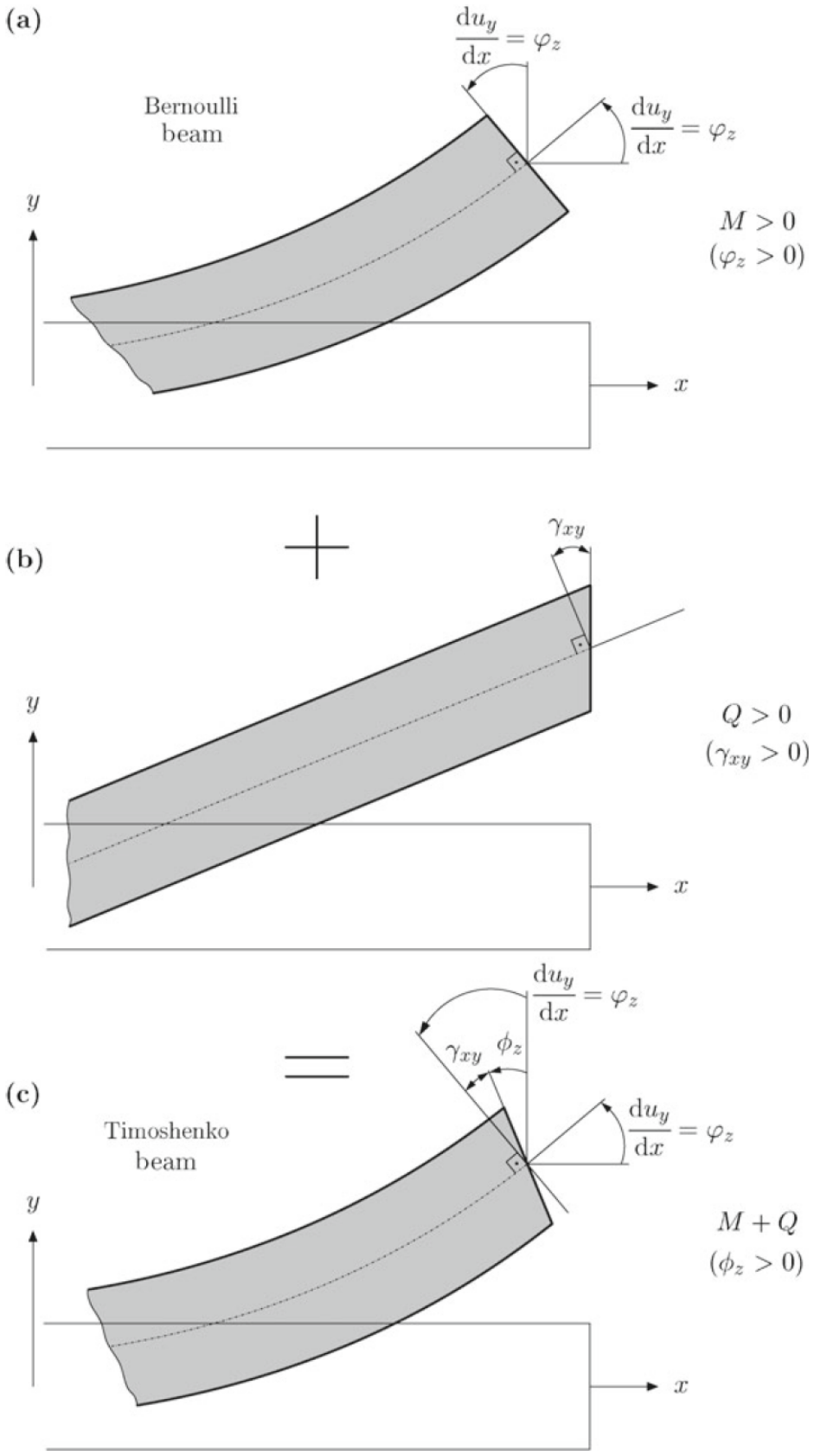

Figure 13: Superposition of the Euler–Bernoulli beam (a) and the shear deformation (b) to the Timoshenko beam (c) in the x-y plane [32].

The key assumptions and limitations made in a Timoshenko beam are [32]:

- Shear deformation γ_{xy} is included: Cross-sections remain plane but not necessarily perpendicular to the neutral axis after deformation (see Figure 13b).
- Resulting deformations ϕ_z are assumed to be small (i.e. $\sin\phi_z \approx \phi_z$). Therefore, higher-order, nonlinear terms are ignored, and linear elasticity and small-strain theory are applicable.
- The cross-section of the beam is constant throughout the entire length of the beam.
- The beam material is assumed to be homogeneous and isotropic, i.e. constant material (Young's modulus E, shear modulus G) and geometrical (area moment of inertia I, area A, shear factor k) properties are assumed.
- Stress σ is proportional to strain ϵ according to Hooke's law: $\sigma = E\epsilon$
- Shear stress and strain are assumed constant instead of parabolic across each cross-sectional area and vary only along the center line of the beam. A shear correction factor k is introduced to account for this non-uniform shear stress distribution.

The concept of Timoshenko beam elements is used for the setup of the turbine structure within HAWC2, and played a key role in the implementation of the enhanced drivetrain structure, and therefore in answering research questions RQ 3-I to RQ 3-V.

Multibody formulation

Since Timoshenko beam elements are limited in their geometric configurations and unable to capture nonlinear effects, multibody formulations are employed in HAWC2. By interconnecting beam elements to form bodies or subbodies, structural nonlinear effects such as large rotations and translations can be modeled and internal inertia loads calculated [6]. This is crucial for the dynamic analysis of the structure [7].
In addition, the interface between bodies can be used to apply constraint equations, for example, representing coupling or bearings. This enables the simulation of the entire wind turbine response. In HAWC2, the kinematics of each body and each element is described in their own floating reference system [33]. This formulation differs from the one-body linear model and is crucial to obtain realistic responses of long and flexible wind turbine blades. The difference between these two concepts is illustrated in Figure 14. The three-body model captures the bending deformation more accurately, as its nodes are not only displaced linearly in the vertical bending direction but also horizontally.
For the implementation of the support structures of the SIMPACK model, the main bearings and the torque arms, however, the one-body model will be used, especially because of its linear characteristics (see subsection 3.3). The position of each coordinate system is defined by translation and rotation relative to the previous coordinate system, with one initial coordinate system being linked to a global frame of reference [7][34].

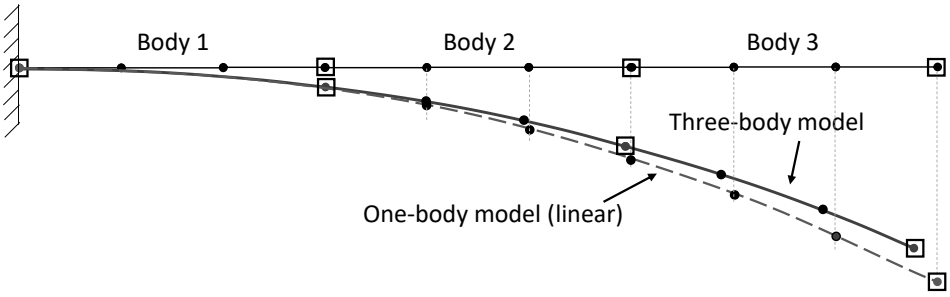

Figure 14: Structural representation of a clamped cantilever beam in a floating reference system with three bodies compared to the linear one-body model [33].

2.3. Software

Although the development of a drivetrain model is not limited to a specific software, this project focuses on the implementation within HAWC2 only. However, additional tools are necessary to derive the HAWC2 model, run simulations, analyze, and visualize the results. This section gives an introduction to all the tools needed during this project. Since it is a major environment, the primary focus is on describing the HAWC2 software.

HAWC2

HAWC2 is a second-generation, aero-servo-elastic code developed at Risø National Laboratory by the DTU Wind Energy department to calculate wind turbine responses in the time domain [6]. It is a verified, well-established code that is used in various applications in the wind energy industry. As discussed in the previous section, the turbine structure is represented by a multibody formulation and defined in a so-called htc-file, combined with a set of structural input files (st-files) that specify the cross-sectional properties of each body. The detailed setup and interaction of the htc- and the st-files are described in the HAWC2 manual [34].
An example of a possible implementation can be seen in Figure 15a. Each body has its own coordinate system and consists of a user-defined number of Timoshenko beam elements. This enables adaptive modeling, depending on the requirements of the application. Although freely selectable, the coordinate systems as defined in Figure 15b are recommended and the same convention is used for the DTU 10 MW RWT model [34]. Different bodies are combined using coupling constraints that replace mechanical connections like couplings or bearings. A list of the available HAWC2 constraints is shown in Table 6 in subsection 3.1. These constraints account for nonlinear effects like rotations or deformations. Furthermore, the division of a body into a deliberate number of linear beam elements can be used to model body deflections accurately [6][34].

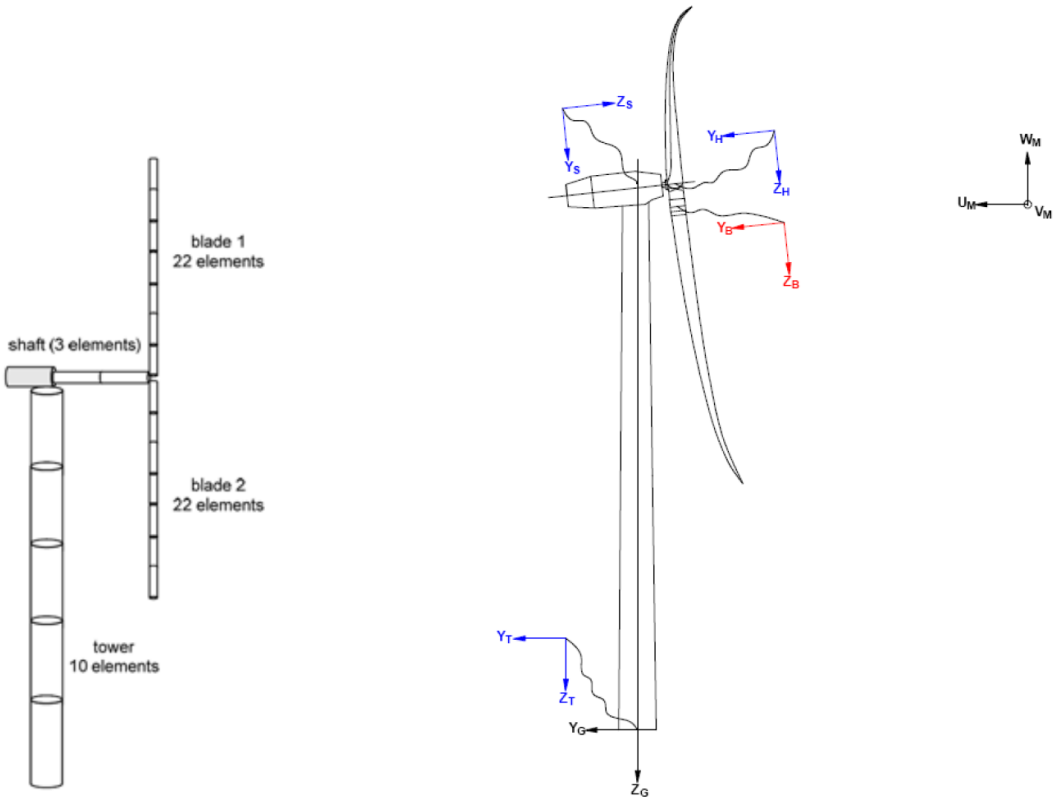

(a) Schematic multibody representation of a WT in HAWC2 [6].

(b) Standard definitions of coordinate systems in HAWC2 [34].

Figure 15: Wind turbine setup in HAWC2.

The structural part is used in combination with aerodynamic calculations that are based on the blade element momentum theory [34]. To obtain higher fidelity results, wake expansion and additional theoretical concepts (summarized in Table 20 in Appendix B) are included in the code.
The turbine can be controlled during the simulations through a flexible set of Dynamic Link Libraries (DLLs). The number of DLLs and their sensors can be customized to control different parameters or settings. By default, a pitch-regulated variable speed controller is implemented [6].
It is also possible to connect user-defined systems to HAWC2 via an external system interface. This allows user-specified equations of motion (EOMs) for a dynamic system to be solved alongside HAWC2's wind turbine EOMs. The interaction is governed by constraint equations that link the external system's degrees of freedom (DOFs) to HAWC2's DOFs. The external EOMs and constraint equations are implemented in a DLL, used by HAWC2 during simulation. External systems can be used, for instance, to model gearboxes [6].

The HAWC2 package includes a number of models and features that can be used for the conceptual design, load simulations, site-specific simulations, and certification of large wind turbines [6][35]. The three main program tools and their purpose are listed in Table 5. They represent the core code of the software, covering the aeroservoelastic calculations and stability analysis. Additionally, the HAWC2 Visualization tool, a 3D-visualizer, was used to illustrate the implemented multibody structure. External effects such as wind, waves, and the soil can also be modeled with HAWC2 [6][34].

Table 5: HAWC2 programs and their features [6][34]

Program	Feature
HAWC2S	Steady state calculations of aerodynamic forces and deflections
HAWCStab2	Linearized aeroelastic stability analysis; Visualizing mode shapes
HAWC2	Calculates turbine's response to time-varying wind inputs

The HAWC2 code is developed in Fortran, and can be utilized by any programming environment. The wind turbine is described in a master file and a number of sub-files that contain additional structural, aerodynamic, and controller parameters. The master file includes data regarding the multibody setup of the turbine, input parameters regarding steady aerodynamic calculations, and parameters related to time-varying simulations [34].

SIMPACK

SIMPACK by Dassault Systèmes is a high-fidelity multi-body simulation (MBS) software developed for analyzing the dynamic behavior of mechanical and mechatronic systems. The software enables the modeling of rigid and flexible bodies, and provides a wide range of predefined joints, constraints, and force elements to apply problem-specific boundary conditions and define the degrees of freedom accordingly. User-defined parameters can also be used, making SIMPACK suitable for multiple engineering disciplines. It can be used for aeroelastic wind turbine simulations, and, as presented in section 1, for modeling drivetrains.
SIMPACK uses a 'tessellated' approach, where mass properties are calculated by integrating over the discretized geometries. FEM data can also be used as input data to determine the body properties [36][37].

Other software

For the derivation of the HAWC2 drivetrain model and for the analysis of the results, further software is used. The CAD tool SOLIDWORKS is chosen to analyze the 3D geometry of components, such as the main shaft [38]. More details on this procedure are provided in subsection 3.1 and subsection 3.2. All HAWC2 implementations and modifications, the initialization of the simulations, as well as the analysis of the results, are carried out in the open-source editor VS Code, using Python [39].
To gain the necessary experience with the software, the HAWC2 manual [34] provided detailed guidance, and the DTU online course 'HAWC2 Selfstudy' offered additional support. Additionally, the graphical data analysis program PDAP, developed by DTU, was used to visualize the simulation results [40].
Apart from brainstorming and conceptual drawings, the presented software tools provided the main support throughout the entire project process - from developing an advanced drivetrain structural model in HAWC2 to analyzing and comparing the outcomes with higher-fidelity models.

3. Implementation

The five implementation steps, as depicted in Figure 2 and illustrated for a better overview again in Figure 16, are presented in this section. They describe in detail how the enhanced HAWC2 drivetrain layout was developed, aiming to provide a clear understanding of the applied methods. Each step is structured according to the same logic:

- Objective and Relevance
- Model Procedure
- Model Rationale
- Model Limitations

First, the objective of each step is outlined, and its relevance to the corresponding research question is highlighted. This is followed by an in-depth description of the implementation procedure. Finally, the chosen approach is justified, and its limitations are discussed.

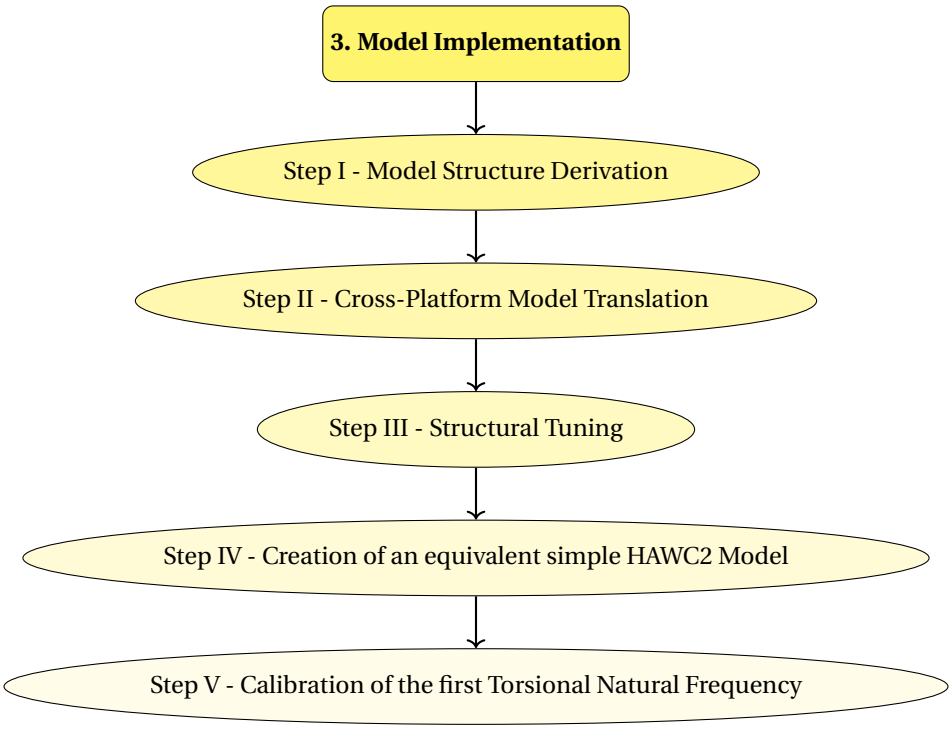

Figure 16: Flowchart of the Implementation Phase.

3.1. Step I - Model Structure Derivation

Objective and Relevance

The first implementation step focused on deriving a drivetrain structure from the SIMPACK model that could be represented in HAWC2 using Timoshenko beam elements. This step was particularly critical, as it defined the overall layout and thereby laid the foundation for the subsequent workflow. Moreover, it determined whether the resulting model could effectively capture dynamic responses at key locations. In particular, the objective was to identify the main components and key points of interest, such as the positions of the main bearings, and other support points (see RQ 3-I in Figure).

Procedure

Starting from the topological SIMPACK drivetrain model (see Figure 12), related components were identified and grouped together. As a first step, a very detailed division was made, where only rotating components with the same rotational speed were combined. Subsequently, incremental simplifications were applied and larger units obtained until the main drivetrain elements were isolated, and further simplification would lead to a considerable loss in detail. Furthermore, an important criterion for the outcome was that the implementation of the final representation with Timoshenko beams was feasible.
Figure 17 to Figure 18 illustrate the first and the last steps of this process. Each color represents a structure that can either be considered as a separate body in HAWC2 (e.g. the hub, the mainshaft, the mainframe), or as a group of components that need to be modeled together due to the limitations of the multibody formulation in the HAWC2 software (see section 2).
Subsequently, incremental simplifications were applied to increasingly larger assemblies, culminating in the isolation of the main drivetrain elements amenable to modeling with Timoshenko beam theory.

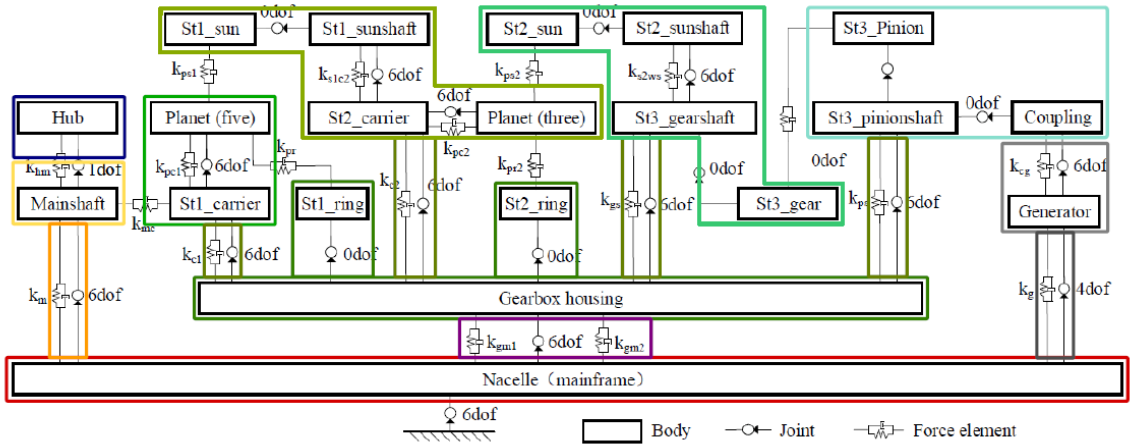

Figure 17: Identification of related drivetrain components - initial step: Grouping with respect to the same rotational speed.

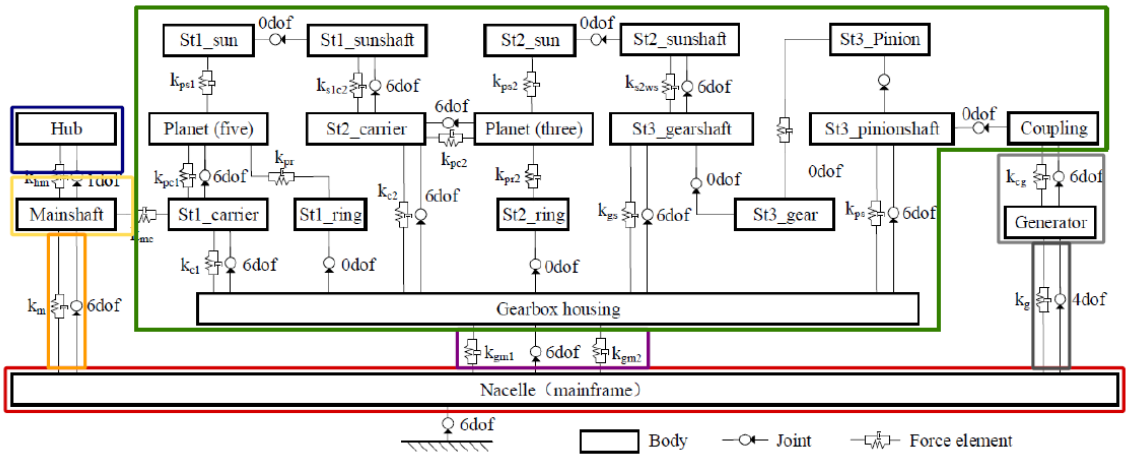

Figure 18: Identification of related drivetrain components - final step: Identification and isolation of key drivetrain components for representation in HAWC2.

The final simplification step was used as a template for the initial HAWC2 drivetrain configuration shown in Figure 19. The lines represent Timoshenko beams, and therefore, the derived drivetrain structure used to replace the original HAWC2 configuration. The tower, the mainshaft, and the mainframe, illustrated with dotted lines, are the components that can potentially be modeled with flexible beams in this configuration, due to the available data from the SIMPACK reference model and the existing HAWC2 model. The most significant simplification affected the representation of the gearbox, where all three stages are combined into a single Timoshenko beam. This approach was necessitated by the constraint that only fixed-node connections are supported within HAWC2. For the initial implementation of the structure, the different beam elements were assigned with arbitrary but realistic input values, since the SIMPACK model was not yet available at that time. Therefore, the model's functionality was verified only through visual inspections and simple simulations. These artificial values were later substituted with the real model data.

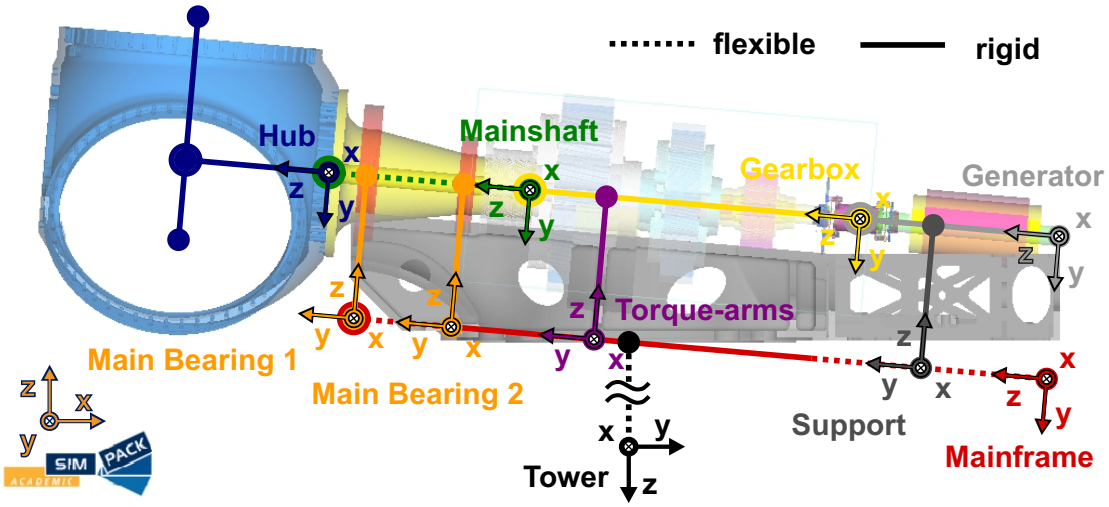

Figure 19: First HAWC2 drivetrain implementation derived from the SIMPACK model.

Rationale

This approach was chosen for three main reasons. First, the SIMPACK model became available at a later project stage. Until then, the published paper [22] provided the only source of model data. Consequently, detailed, geometric specifications were still missing, and the topological representation, together with the

accessible data, served as a guideline for a rough draft of the drivetrain model. Access to the model at an earlier stage would have allowed the direct use of the exact geometric dimensions and material specifications. Second, starting from the complex model and iteratively grouping components into subunits allowed for a better understanding of the setup and the functionality of the provided model. And finally, this systematic approach enabled the derivation of a simplified, yet representative structure that can be implemented within HAWC2 and at the same time maintain core characteristics of the higher fidelity model.

Limitations

The Model Structure Derivation step aimed to simplify the high-fidelity model as much as possible while minimizing any loss of its original accuracy. However, due to the constraints associated with Timoshenko beam elements in the HAWC2 modeling environment, compromises were inevitable, both in terms of result quality and the level of detail.
While SIMPACK provides specific modeling elements for bearings, couplings, or gear stages where individual parameters can be defined by the user, HAWC2 only offers a small set of possible joints between two bodies, as specified in Table 6. The transmission of forces and moments from one body to another is possible only by connecting two nodes with one of these predefined constraint types. They only offer the possibility of entirely free or locked degrees of freedom, allowing for either completely rigid or completely frictionless connections. Consequently, gear pairs that rely on tooth contact for the transmission, or joints characterized by stiffness or damping assigned to individual DOFs, are not modeled accurately in the present configuration. For the presented configuration, only combinations of the two standard constraints `fix1` and `bearing1` were employed. In Step III, additional HAWC2 constraint types were integrated and are discussed in subsection 3.3.
Additionally, due to the simplified gearbox representation, internal forces and moments originating from gearbox stages, as well as the flexible components inside the gearbox, are not explicitly represented, potentially affecting the dynamic response.
For the same reason, the connections between the four rotating components, the generator, the gearbox, the shaft, and the hub, can only be realized by fixing the corresponding nodes rigidly to each other. As a result, elastic coupling effects, such as those present between the generator and gearbox, are not captured in the model, potentially causing discrepancies in the resulting moments.
Some of these limitations will be partially addressed in subsequent implementation stages.

Table 6: Supported HAWC2 constraint types [34].

Constraint Type	Description
`fix0`	Clamped to the ground
`fix1`	Clamped connection
`fix2`	Fix node to ground, optionally specify axis of free translation
`fix3`	Fix node to ground, optionally specify axis of free rotation
`fix4`	Locked in translation, but not in rotation, with pre-stress feature
`bearing1`	Frictionless bearing
`bearing2`	Bearing for which a fixed angle is specified by an external DLL
`bearing3`	Bearing with a constant specified angle velocity
`bearing4`	Cardan shaft, locked in rotation around one vector, but free to rotate around the two other axes
`bearing5`	Spherical constraint, fixed in translation, free to rotate around any of the three axes

3.2. Step II - Cross-Platform Model Translation

Objective and Relevance

In the previous implementation stage, a HAWC2 structure was defined that represents the existing SIMPACK model. The next critical step included finding a robust method for translating parameters between the two representations, ensuring that as many of the original system characteristics as possible are preserved. The main objective, therefore, was to extract the geometric and material properties from the SIMPACK model and use them as input for the HAWC2 drivetrain structure. By answering research question RQ 3-II, consistency in terms of mass and inertia distribution should be ensured.

Procedure

Two main parts can be identified for this step. First, the drivetrain components were analyzed individually, in terms of their geometry and their structural properties. Subsequently, the geometric assembly of the entire structure, as depicted in Figure 19 was assessed.
Regarding the former, 19 input parameters are required to fully define a Timoshenko beam in HAWC2. An overview and the definition of these can be found in Table 7. The exact derivation of these parameters is straightforward for simple cross sections consisting of a single isotropic material. For more complex geometries, however, approximations or assumptions have to be made. Furthermore, not every parameter is individually relevant for the computations. The eight variables 9 to 16 define the longitudinal stiffness EA, the bending stiffnesses EI_x, and EI_y, the shear stiffnesses k_xGA, and k_yGA, and the torsional stiffness KG. Since these six products determine all cross-section stiffness properties of the beam, two of the eight input parameters involved can be chosen arbitrarily, as long as the underlying equations are fulfilled. This feature was used in Step III and is explained in more detail in the corresponding section.

Table 7: Timoshenko input parameters in HAWC2 (Adapted from [34]).

Column	Symbol	Unit	Description
1	s	[m]	Curved length distance from main_body node 1 [m]. HAWC2 normalizes this by the curved length defined in c2_def.
2	m	[kg/m]	Mass per unit length
3	x_m, x_{c2}	[m]	x_{c2}-coordinate from $C_{1/2}$ to mass center
4	y_m, y_{c2}	[m]	y_{c2}-coordinate from $C_{1/2}$ to mass center
5	r_{ix}	[m]	Radius of gyration related to elastic center. Corresponds to rotation about principal bending x_e axis
6	r_{iy}	[m]	Radius of gyration related to elastic center. Corresponds to rotation about principal bending y_e axis
7	x_s, x_{c2}	[m]	x_{c2}-coordinate from $C_{1/2}$ to shear center [m]. The shear center is the point where external forces only contributes to pure bending and no torsion.
8	y_s, y_{c2}	[m]	y_{c2}-coordinate from $C_{1/2}$ to shear center [m]. The shear center is the point where external forces only contributes to pure bending and no torsion.
9	E	$[N/m^2]$	Modulus of elasticity
10	G	$[N/m^2]$	Shear modulus of elasticity
11	I_x	$[m^4]$	Area moment of inertia with respect to principal bending x_e axis. This is the principal bending axis most parallel to the x_{c2} axis
12	I_y	$[m^4]$	Area moment of inertia with respect to principal bending y_e axis
13	K (I_p)	$[m^4/rad]$	Torsional stiffness constant with respect to ze axis at the shear center. For a circular section only this is identical to the polar moment of inertia I_p.
14	k_x	[-]	Shear factor for force in principal bending x_e direction
15	k_y	[-]	Shear factor for force in principal bending y_e direction
16	A	$[m^2]$	Cross sectional area
17	θ_z	[deg]	Structural pitch about z_{c2} axis. This is the angle between the x_{c2}-axis defined with the c2_def command and the main principal bending axis x_e.
18	x_e, x_{c2}	[m]	x_e, x_{c2}-coordinate from $C_{1/2}$ to center of elasticity [m]. The elastic center is the point where radial force (in the z-direction) does not contribute to bending around the x or y directions.
19	y_e, y_{c2}	[m]	y_e, y_{c2}-coordinate from $C_{1/2}$ to center of elasticity [m]. The elastic center is the point where radial force (in the z-direction) does not contribute to bending around the x or y directions.

As discussed earlier, the only drivetrain components that can be modeled as flexible bodies are the mainshaft and the mainframe. Since the structure of the mainframe is rather complex, it was also considered rigid for the implementation of this project. All remaining parts were regarded as rigid, and large stiffness terms were assumed. Since the SIMPACK model provides mass, location of the center of gravity, and mass moments of inertia for all bodies, and HAWC2 offers the option to assign the mass and inertia to a specific point along the curved beam length, negligibly small values could be chosen for parameters 2 to 6 (Choosing a zero value results in a computational error). Furthermore, the shear center (Parameters 7 and 8) and the elastic center (18 and 19) are irrelevant for rigid geometries. Input 17, the structural pitch, only plays a role for twisted beams, like the blades, and was therefore set equal to zero for all involved drivetrain components.
To sum up, for all components apart from the mainshaft, high stiffness terms were used, and the relevant data from the SIMPACK model consisted of the curved length, mass, center of gravity location, and mass moment of inertia about the center of gravity. Since the SIMPACK model represents only the drivetrain, the blade mass and inertia are included in the hub component and therefore had to be subtracted for the HAWC2 input. As HAWC2 offers the option to calculate both the properties of the entire structure and those of individual bodies, determining the blade mass and inertia was straightforward.
Referring to Step III, later adjustments to the input parameters for the support structures - main bearings, torque arms, and generator support - were necessary to capture the system's dynamic behavior more accurately. Table 8 summarizes the material properties that are relevant for the implementation. As noted earlier, the exact values of these constants are only required for implementing structures that are, or could potentially be, modeled as flexible.

Table 8: Material properties of the flexible drivetrain components (Adapted from [22])

Component	**Material**	**Density** ρ [kg/m^3]	**E-Modulus** E [GPa]	**Poisson's Ratio** ν
Shaft	18CrNiMo7-6	7800	207	0.300
Mainframe	QT400-18 A L	7100	169	0.275

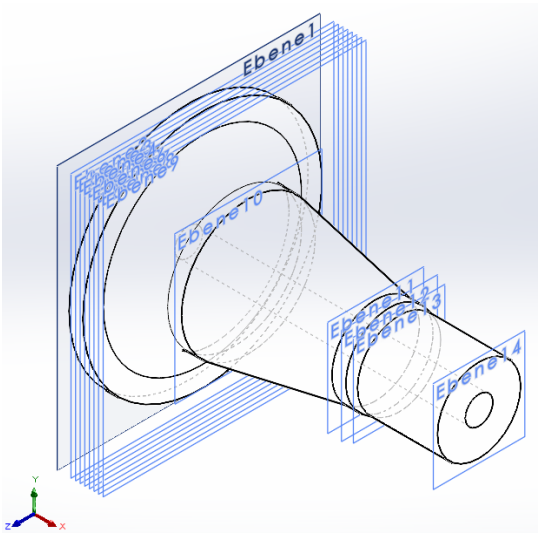

Figure 20: CAD geometry of the mainshaft.

For the mainshaft, a cross-sectional analysis was carried out to determine the Timoshenko input parameters. Due to the simple, annular cross-section, as can be seen in Figure 20, the mass center, the elastic center, and the shear center coincide with the central axis, and the corresponding values could be set to zero. Furthermore, due to the symmetry, all x and y components are identical. An overview of the Timoshenko beam parameters for annular cross-sections is provided in Table 9. For this geometry, well-known equations for the area A, the relative mass m, the mass and area moments of inertia, J and I could be applied. For the calculation of the shear factor k, Equation 1 for a homogeneous isotropic beam according to Cowper and the Timoshenko beam theory was applied [41].

Table 9: Parameters for a hollow circular ring cross-section

Column	Parameter*	Unit	Equation
1	s	[m]	z-coordinate (from CAD)
2	m	[kg/m]	$\rho\pi(R^2 - r^2)$
3	x_m	[m]	0
4	y_m	[m]	0
5	r_{ix}	[m]	$\sqrt{J_x/m}$, $J_x = \frac{m}{4}(R^2 + r^2)$
6	r_{iy}	[m]	$\sqrt{J_y/m}$, $J_y = \frac{m}{4}(R^2 + r^2)$
7	x_s	[m]	0
8	y_s	[m]	0
9	E	[N/m^2]	see Table 8
10	G	[N/m^2]	$\frac{E}{2(1+\nu)}$, see Table 8
11	I_x	[m^4]	$\frac{\pi}{4}(R^4 - r^4)$
12	I_y	[m^4]	$\frac{\pi}{4}(R^4 - r^4)$
13	I_p	[m^4/rad]	$\frac{\pi}{2}(R^4 - r^4)$
14	k_x	[-]	(see Equation 1)
15	k_y	[-]	(see Equation 1)
16	A	[m^2]	$\pi(R^2 - r^2)$
17	θ_z	[degree]	0
18	x_e	[m]	0
19	y_e	[m]	0
*Refer to Table 7 for the description of the parameters.			

$$k = \frac{6(1+\nu)\left(1+\left(\frac{r}{R}\right)^2\right)^2}{(7+6\nu)\left(1+\left(\frac{r}{R}\right)^2\right)^2 + (20+12\nu)\left(\frac{r}{R}\right)^2} \tag{1}$$

Since the E-Modulus E, the Poisson's Ratio ν, and the density ρ are given from Table 8, all variables could be calculated knowing the outer radius as a function of the distance from the 1st body node $R = f(z)$. With the help of the CAD geometry, the relevant radii for the different cross-sections could be determined in SOLIDWORKS. Figure 20 illustrates the planes used for the cross-sectional analysis. Properties at 15 distinct axial positions were extracted and defined the Timoshenko beam within the structural input files [34]. A reasonable discretization choice had to be made to capture the trend of the outer shaft radius R accurately. In the areas where R changes non-linearly, a higher density of analyzed planes was used. The software also provided the possibility to verify the analytically derived values for the area moments of inertia.
Subsequently, the geometric assembly of the SIMPACK drivetrain was studied and used to obtain the correct dimensions for the HACW2 setup. Building up on the general configuration that was already implemented in the previous step, Figure 21 and Figure 22 were derived, and the arbitrary values replaced by the correct ones. Due to the constraints discussed in the previous implementation stage, the generator beam had to be axially aligned with the three other rotating components, the gearbox, the main shaft, and the hub. The y-offset of the SIMPACK coordinate system (see Figure 22) had therefore been neglected.

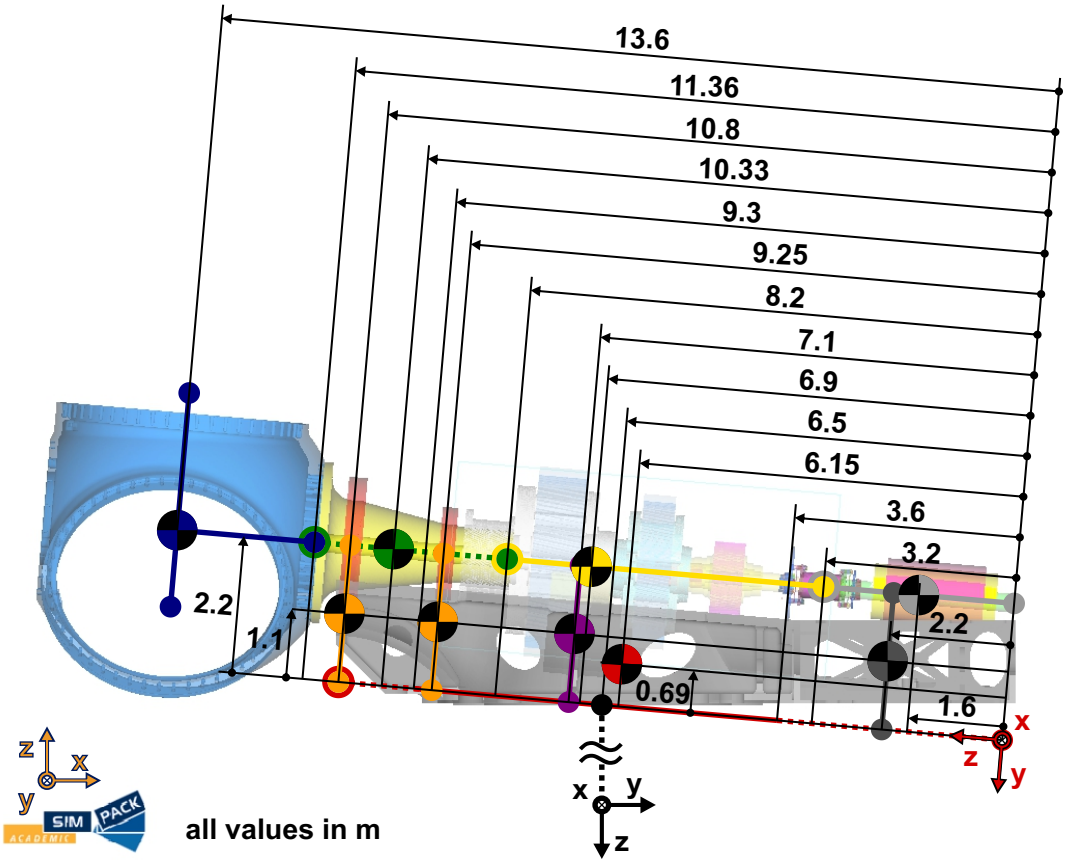

Figure 21: Side view of the drivetrain structure dimensions.

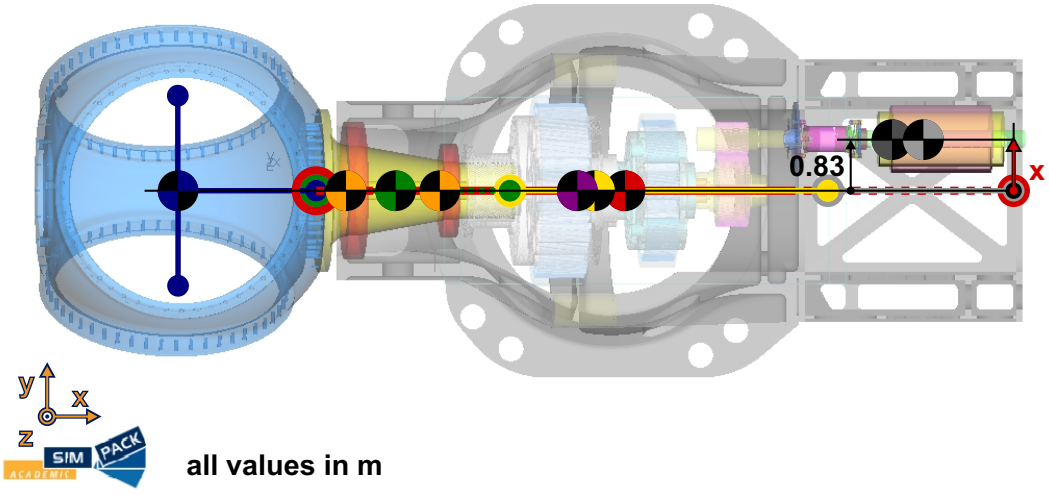

Figure 22: Top view of the drivetrain structure dimensions.

After implementing the drivetrain model with the geometric specifications as shown in the two figures above, it was important to confront the preliminary new HAWC2 structure with the SIMPACK configuration.

This was done by comparing both the mass and the center of gravity (CG) locations of all individual components, as well as the entire drivetrain. For this purpose, the drivetrain structure was isolated from the tower and the blades, and fixed at the location of the yaw bearing (tower top). Using the HAWC2-inherent output methods to calculate the required outputs, the values of both models could be compared with each other. The results are summarized in Table 13 at the end of Step IV and demonstrate good overall agreement. The x-component is zero due to the symmetric HAWC2 configuration (see Figure 22) and only differs slightly from the SIMPACK value (x_{CG} = 0.023 m). All remaining differences are within 1.2% and can be attributed to the limitations discussed in the section below.
Since the mass moments of inertia were assigned to the beams at their respective centers of gravity—consistent with the approach used in SIMPACK—their contributions aligned with those of the reference model.

Rationale

The described procedure was considered the most practical approach for mapping the characteristics of the SIMPACK model to the Timoshenko beam model. Since the focus at this development stage was laid on matching the dimensions, the weight distribution, and the inertia of the structure, flexibility properties of connections, like the main bearings or the torque arms, were neglected.

Limitations

While the chosen approach is highly accurate for rigid structures and homogeneous, isotropic bodies with simple cross-sections, representing the behavior of complex 3D geometries using a 1D beam model with assigned cross-sectional properties along its length is non-trivial and demands advanced computational methods. Furthermore, every type of discretization inherently involves some degree of information loss. While cylindrical and conical segments are represented accurately by the two bounding sections, a discretization choice must be made for fillet radii. As described in [34], in the htc-file, the actual main body is defined by assigning dimensions and nodes. The total length of this body is scaled to match the curved length specified in the st-file, and for each node n_i, the equivalent structural properties are interpolated from the table in the st-file. Figure 23 illustrates how this is done based on the example of the shaft mass distribution. The blue cross-markers represent the discrete data from the structural input file, and the orange point-markers the body nodes, defined in the htc-file. The relative mass m for each element (horizontal lines) is calculated by integrating the blue curve over the corresponding section and dividing it by the element length.
This integration-based averaging is applied to all 19 cross-sectional properties. This method ensures that the overall mass of the defined body is equivalent to the mass of the input file. However, it does not guarantee that the static mass moment, i.e., the location of the center of gravity, coincides. HWAC2 offers the options to either keep the overall integrated mass consistent or scale the mass to match the static mass moment. Scaling the mass is the default method and was also applied for the shaft implementation (see `mass_scale_method` in [34]). As a consequence, discrepancies in the total shaft mass had to be expected.
Lastly, the implementation neglects the offset of the generator from the shaft axis, which has an impact on the resulting forces and moments.

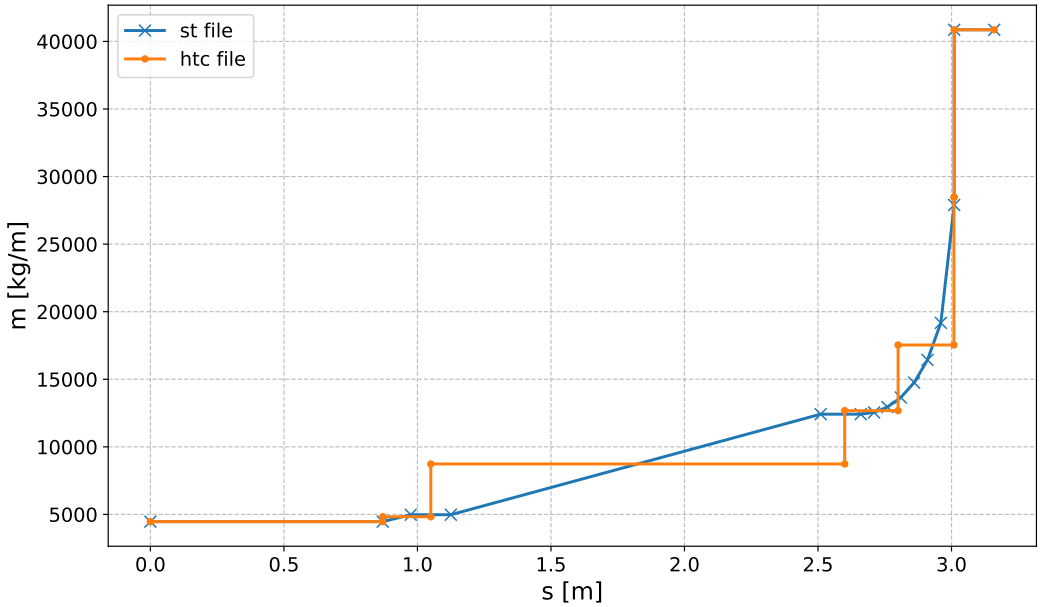

Figure 23: Property mapping of st.-to-.htc-files according to [34].

3.3. Step III - Structural Tuning

Objective and Relevance

As previously mentioned, the precise characteristics of the joints and constraints between the drivetrain subcomponents were not considered in the earlier steps. A more detailed analysis is required, along with corresponding adjustments to the HAWC2 configuration. Figure 18 illustrates the connection constraints between the individual components. While a few interfaces are fully rigid (i.e., 0 DOF), most are defined by specific stiffness and damping properties. The goal of the Structural Tuning step, as described in this section, was to incorporate as many of these characteristics as possible to ensure a comparable dynamic behavior. The applied procedure provides an answer to the research question RQ 3-III.

Procedure

In the SIMPACK model, all major joints are defined via so-called Force Elements, and as force type, predominantly `43: Bushing Cmp`, as shown in Figure 67 in Appendix A are used. This element is comparable to a three-dimensional spring-damper system and defines a connection between two markers (i.e. specified locations that are typically linked to a body or the Inertial System). As shown in Appendix A, stiffness, and damping values can be assigned in all three translational and all three rotational directions to define the behavior of the connection. The values used for the two main bearings (MB), the torque arms (TA), the generator, and the shaft-gearbox couplings are depicted in Table 10. Latter was modeled as a rigid connection due to its large stiffness values. While the remaining stiffness terms could be taken directly from the corresponding force element, the equivalent K_α for the generator coupling had to be calculated from the three implemented coupling elements in SIMPACK, following the law for spring constants in series:

$$\frac{1}{K_{\text{eq}}} = \sum_{i=1}^{n} \frac{1}{K_i} \tag{2}$$

However, since the generator shaft of the HAWC2 model is directly connected to the mainshaft and hence underlies the same torque, this term would have to be adjusted to account for the change in rotational speed and torque due to the gearbox. Therefore, and for simplicity reasons, it was decided to introduce a K_α that essentially corresponds to infinitive stiffness.

Table 10: Overview of the stiffness and damping parameters of the major support components from the SIMPACK reference model.

Parameter	MB front	MB rear	TA left/right	Gen. Coup.	Shaft-GB Coup.
K_x [kN/m]	3 524 500	3 387 900	120 000	0	1E+12
K_y [kN/m]	8 924 400	5 378 100	240 000	0	1E+12
K_z [kN/m]	12 520 000	8 782 300	2400 000	0	1E+12
K_α [kNm/rad]	0	0	120 000	1 164 545	0
K_β [kNm/rad]	1 210 800	592 240	240 000	0	1E+12
K_γ [kNm/rad]	862 240	362 150	240 000	0	1E+12
C_x [kNs/m]	3 524.5	3 387.9	120	0	1E+9
C_y [kNs/m]	8 924.4	5 378.1	240	0	1E+9
C_z [kNs/m]	12 520.0	8 782.3	24 000	0	1E+9
C_α [kNms/rad]	0	0	120	0	1E+9
C_β [kNms/rad]	1 210.8	592.24	240	0	1E+9
C_γ [kNms/rad]	862.24	362.15	240	0	1E+9

Translating these lumped stiffness and damping values at the equivalent locations in the HAWC2 drivetrain using Timoshenko beams is challenging. Since they cannot be directly applied, careful conversion and approximation methods were necessary. In the following, a simple elastic cantilever beam made of an isotropic and homogeneous material, with a constant cross-sectional area A was considered. When clamped at one end, three basic deformations can be observed: I. longitudinal (Δl), II. bending (δ), and III. torsional deformation (θ). Figure 24 illustrates the three deformation types along with their corresponding equations, where l is the beam length, F and M_t are the applied force and moment, E is the Young's modulus, A the cross-sectional area, G the shear modulus, k the shear constant, I the area moment of inertia, and K the polar moment of inertia, hereafter also referred to as I_p.

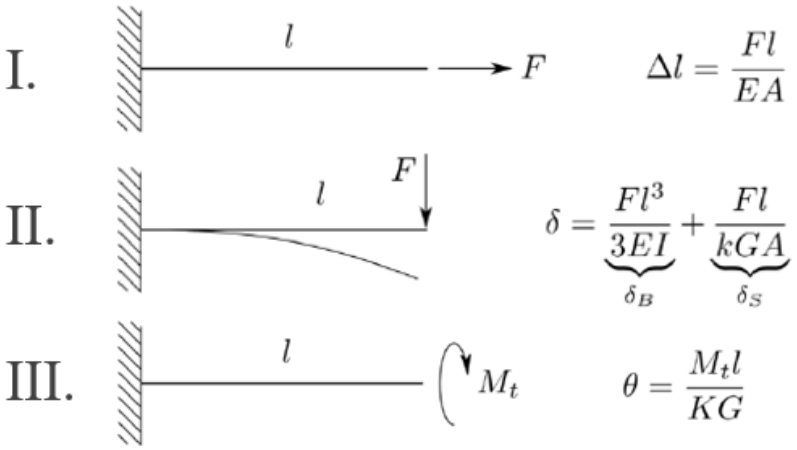

Figure 24: Timoshenko beam deformation: I. Longitudinal, II. Bending, III. Torsion (Adapted from [42]).

Main bearings

To obtain a similar connection between the mainframe and the mainshaft, the stiffness constants from Table 10 for the main bearings and equations for the three beam deformations were used together with the available HAWC2 constraints from Table 6. The damping values were initially disregarded. Since the properties of front and rear main bearings only differ in the magnitude of the stiffness terms, the following description focuses on the front bearing only. The same procedure was applied for the rear counterpart.
Figure 25 shows the preliminary implementation of the shaft and the front bearing, as well as the relevant coordinate systems. The global reference system CS_{SP} is adopted from the SIMPACK environment and is therefore consistent with the properties in Table 10. The body coordinate system of the front main bearing (defined at node n1) was used to define the cross-sectional beam properties.
Until this stage, all support structures were modeled as two-node beams with very high stiffness. At node n1, they were rigidly connected to the mainframe using the `fix1` constraint in HAWC2 (0 DOF), while the second node used a `bearing1`-type connection to allow rotation only around the shaft axis (the local y-axis of the front MB), equivalent to 1 DOF. Therefore, a method had to be found to incorporate the remaining five stiffness coefficients by using combinations of the three deformation forms from Figure 24.

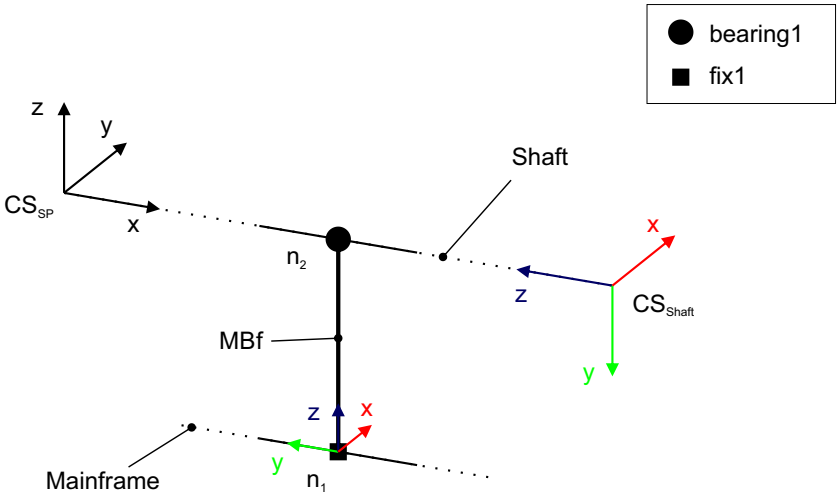

Figure 25: Preliminary main bearing implementation: 1 DOF - Rotation around shaft axis.

Different approaches were tested, yet the most comprehensible was found to be a three-beam model (3BM). Not only was the implementation straightforward, but it also showed good accordance with the joint characteristic in SIMPACK. To match the stiffness constants in all three dimensions, one support beam was introduced along each principal direction, x_{SP}, y_{SP}, and z_{SP}. To facilitate comparability, the SIMPACK coordinate system orientation was adopted for each joint. Thus, the originally implemented single support beam (e.g., `MB_front`) was replaced by three Timoshenko bodies, `MBf_Kx`, `MBf_Ky`, and `MBf_Kz`. All were connected at their node 1 to the same, corresponding shaft node, and extending in positive x-, y-, and z-directions of the SIMPACK coordinate system CS_{SP}. This new arrangement is shown in Figure 26.

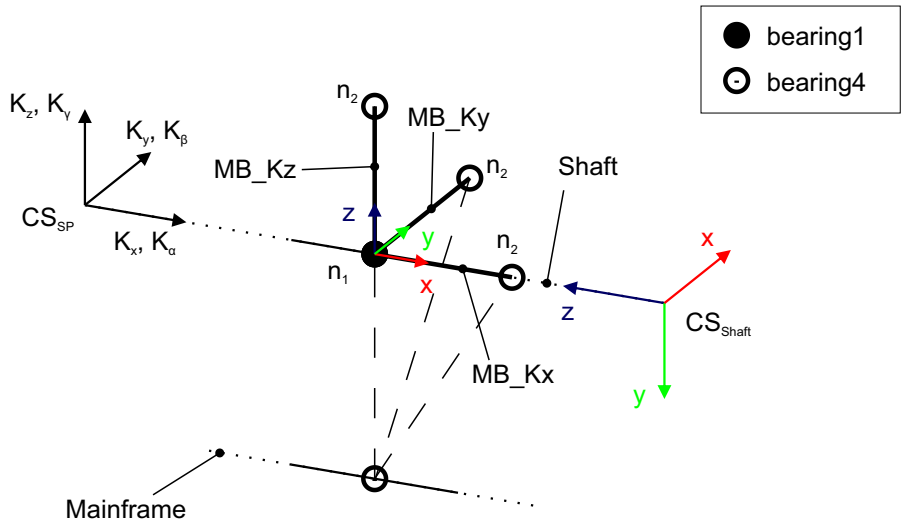

Figure 26: Adopted main bearing implementation: 6 DOF - 5 stiffness terms.

Since HAWC2 allows rigidly connecting two nodes even if they are spatially separated by an offset, the second nodes were fixed to the corresponding mainframe location. The concept of this configuration was to assign each beam the related longitudinal and torsional stiffness along its axial direction.
To achieve this, the equations for the beam deformations (Figure 24) were rearranged to derive the corresponding axial, bending, and torsional stiffnesses. The goal of this manipulation was to obtain an expression that could be set equal to the values in Table 10. Ensuring dimensional consistency, Equation 3 to Equation 5 were obtained.

$$\Delta l = \frac{Fl}{EA} \quad \rightarrow \quad K_l = \frac{F}{\Delta l} = \frac{EA}{l} \tag{3}$$

$$\delta = \frac{Fl^3}{3EI} + \frac{Fl}{kGA} \quad \xrightarrow{\text{for } k \text{ large}} \quad K_b = \frac{F}{\delta} = \frac{3EI}{l^3} \tag{4}$$

$$\theta = \frac{M_t l}{I_p G} \quad \rightarrow \quad K_t = \frac{M_t}{\theta} = \frac{I_p G}{l} \tag{5}$$

The second term in Equation 4 corresponds to the bending deformation due to the shear stiffness kGA. To obtain a classic Euler–Bernoulli beam, i.e. a beam where shear deformation can be disregarded, the second term has to become negligibly small. This can be achieved, for instance, by choosing a sufficiently large shear coefficient k. Since the purpose of the implemented support beams was to imitate the characteristics of the main bearings, the choice of single material constants was arbitrary. As mentioned above in the description of Step II, only their combination, i.e., EA, EI, and I_pG, matters.

Subsequently, Equation 3 and Equation 5 were used to determine the required input parameters 9 to 16 in Table 7 for the three support beams. Since the number of unknowns and equations was not matching, initial assumptions for the E-modulus E, the G-modulus G, and the beam length l were made and the same values used for all structures. As a next step, the required cross-section A, and the polar moment of inertia I_p could be calculated for each beam using the chosen values for E, G, and l and the stiffness properties from Table 10:

$$A_{x,y,z} = \frac{K_{x,y,z} l}{E} \tag{6}$$

$$I_{P/\beta,\gamma} = \frac{K_{\beta,\gamma} l}{G} \tag{7}$$

Equation 6 and Equation 7 assume that each beam exclusively carries axial forces and torsional moments along its own axis, and has no contribution to the other stiffness components. To ensure this behavior, two possible approaches, to minimize the coupling effects were identified.
The most obvious and robust solution involves modeling the beams as a cardan shaft, with both ends being

locked in translation and in rotation about their own axis, while allowing free rotation about the two perpendicular axes (see Figure 27). This configuration prevents the transmission of bending moments.

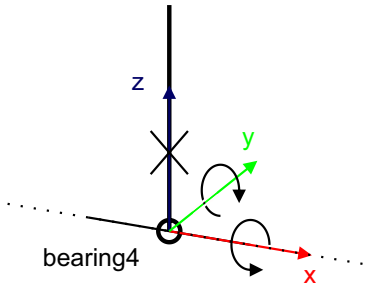

Figure 27: Beam with a cardan shaft-constraint (`bearing4`-command) where the rotation about the beam axis is locked and the rotation about both perpendicular axes is free.

Selecting sufficiently low cross-sectional area moments of inertia, I_i, results in negligibly small bending stiffnesses. From Equation 4, it can be seen that K_b is directly proportional to I. Therefore, a beam with very low bending stiffness can only resist minimal loads in beam-perpendicular directions, and consequently, these loads are taken up by the neighboring support beam with the longitudinal stiffness in that direction. The additional rotational degree of freedom in the first concept resulted in ambiguous constraints at the shaft nodes, causing issues with shaft rotation during the simulations. Therefore, a combination of both methods was applied. The connection with the mainframe was realized with the cardan shaft constraint (see Figure 27 and `bearing4`-constraint in Table 6), while the opposite nodes were connected rigidly with the shaft by employing a `bearing1`-constraint and hence only allowing the rotation around the shaft axis (see Figure 26). In section 4, it will be shown that this setup, combined with low bending stiffnesses, led to satisfying results.

In the following, the same coordinate convention is used as in the HAWC2 st.-files, where the curved length always corresponds to the z-axis, and hence the cross-sectional parameters are always referred to as x and y components. While for the `Kx`-beams, that are aligned with the shaft axis, both cross-sectional area moments of inertia, I_x and I_y were relevant for the application, for the remaining two bodies, only one bending direction mattered. The bending about the axis, parallel to the shaft axis, was irrelevant due to the free DOF around this axis originating from the `bearing1`-constraint. Furthermore, the magnitude of each stiffness value K_i influenced how small I_x/I_y of the neighboring support beams had to be because the major force component will be transmitted to the strongest counterpart. Taking these considerations into account, the area moments of inertia I_x, I_y were incrementally reduced until the six external load components, F_x, F_y, F_z, M_x, M_y, and M_z mainly transmitted longitudinal and torsional loads to the corresponding beam, while maintaining solver stability. An example of this tuning process is illustrated below. Figure 28 shows the residual forces present in the beam-perpendicular directions of the three support beams `MBf_Kx`, `MBf_Ky`, and `MBf_Kz`. These load components should therefore be negligibly small. Figure 29 presents the prevailing and intended force components in x, y, and z direction. It can be observed, that a reduction in I_y from 1E-03 (yellow curve) to 1E-6 (orange curve) led to significantly better results, i.e. lower residuals for one component of all three beams, `MBf_Kx`, `MBf_Ky`, and `MBf_Kz`, while the reduction of I_x from 1E-03 to 1E-04 (red curve) only had an impact on the `MBf_Kx`-beam that is aligned with the shaft axis. Additionally, it can be seen that the residual components $F_{Ky,z}$ and $F_{Kz,y}$ are widely independent due to the `bearing1`-constraint and the related free DOF.

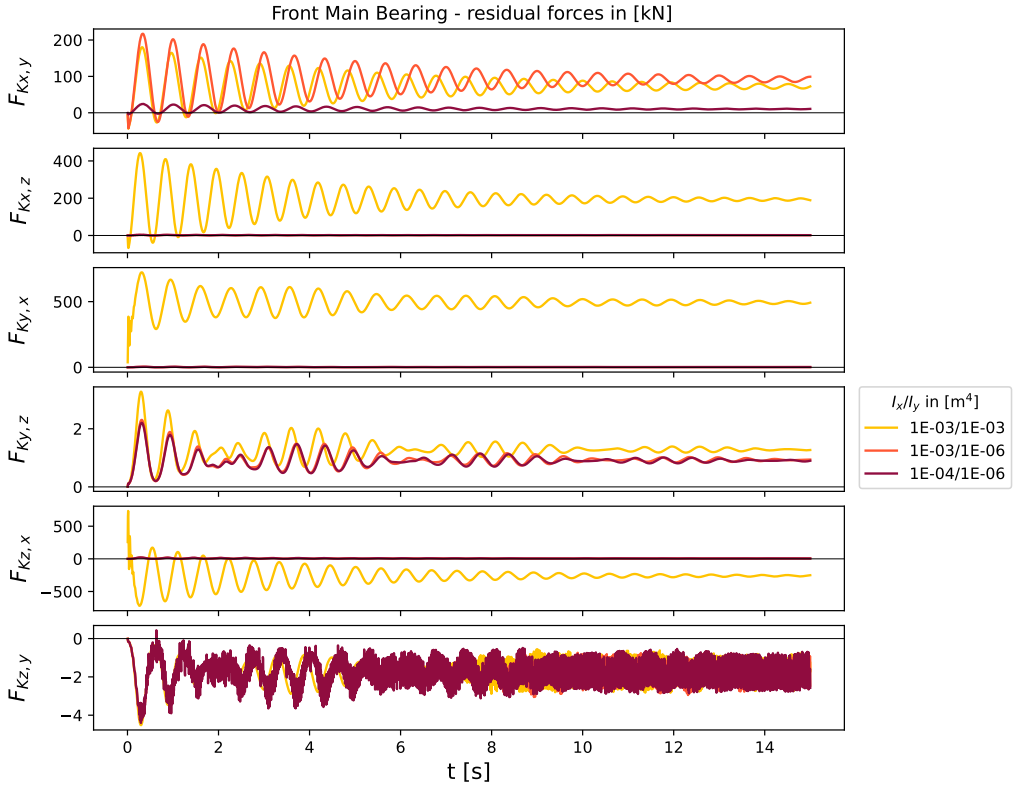

Figure 28: Tuning of cross-sectional bending stiffness - residual force components.

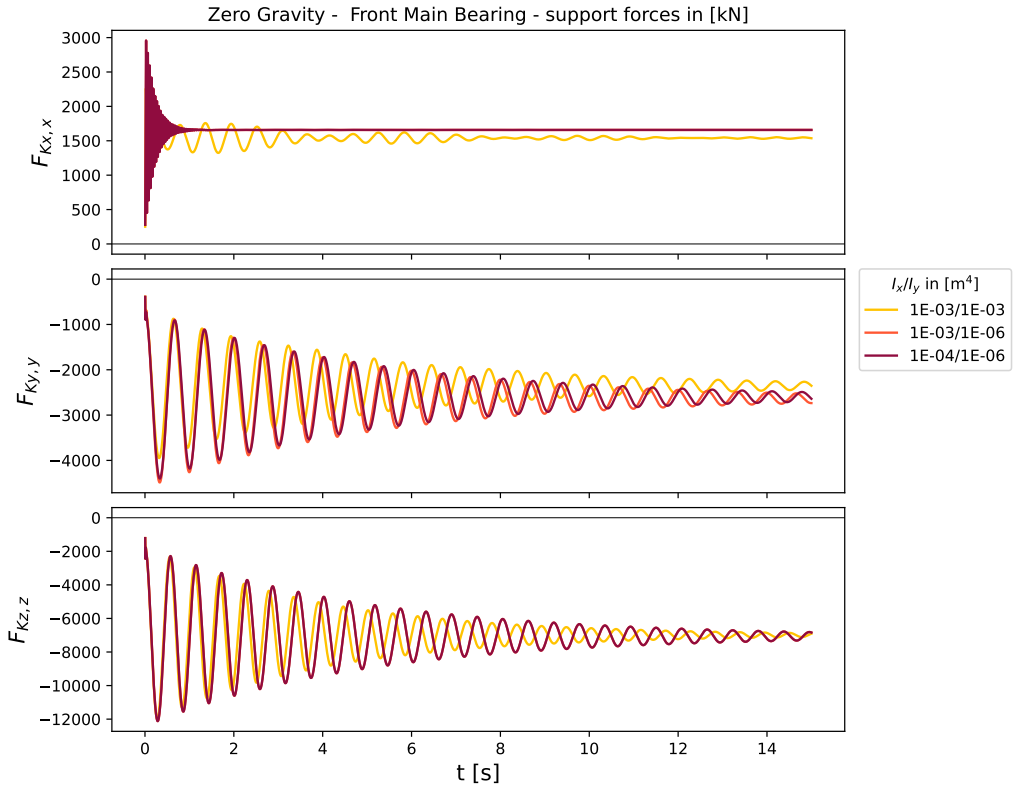

Figure 29: Tuning of cross-sectional bending stiffness - main force components.

Table 11 summarizes the final cross-sectional values obtained for the support structures that model the

main bearings. The values printed in bold were calculated using Equation 6 and Equation 7, and the remaining values were chosen or iteratively optimized. In addition to the experimental tuning of I_x and I_y, described above, using Equation 4, an estimate was made for an arbitrary force F to verify that bending due to shear could be neglected for the combination of chosen and the calculated beam properties:

$$\frac{\delta}{F} = \frac{\delta_{bend}}{F} + \frac{\delta_{shear}}{F} = \frac{l^3}{3EI} + \frac{l}{kGA} \approx \mathcal{O}(10^{-6}) + \mathcal{O}(10^{-15}) \quad \rightarrow \quad \delta_{bend} >> \delta_{shear} \tag{8}$$

A similar estimate was made for the three Euler-Bernoulli beam stiffness terms K_l, K_b, and K_t, always using the most conservative combination of (relevant) cross-sectional parameters and applying Equation 3 to Equation 5:

$$K_l = \frac{EA}{l} \approx \frac{\mathcal{O}(10^{11-2})}{\mathcal{O}(1)} = \mathcal{O}(10^9) \tag{9}$$

$$K_b = \frac{3EI}{l^3} \approx \frac{\mathcal{O}(10^{11-5})}{\mathcal{O}(1)} = \mathcal{O}(10^6) \tag{10}$$

$$K_t = \frac{GIp}{l} \approx \frac{\mathcal{O}(10^{11-3})}{\mathcal{O}(1)} = \mathcal{O}(10^8) \tag{11}$$

Hence, a lower bending stiffness by approximately two to three orders of magnitude was achieved and considered sufficient to have a negligible effect on the results.

Table 11: Overview of cross-sectional beam properties for main bearing support structures and resulting beam stiffnesses

		MB front - beams			MB rear - beams		
Parameter		Kx	Ky	Kz	Kx	Ky	Kz
l	[m]	1	1	1	1	1	1
E	[N/m^2]	2E+11	2E+11	2E+11	2E+11	2E+11	2E+11
G	[N/m^2]	1E+11	1E+11	1E+11	1E+11	1E+11	1E+11
I_x	[m^4]	1E-5	1E-3	1E-3	1E-5	1E-3	1E-3
I_y	[m^4]	1E-6	1E-6	1E-6	1E-6	1E-6	1E-6
$\boldsymbol{I_p}$	[m^4/rad]	1	**1.211E-02**	**8.622E-03**	1	**5.922E-03**	**3.622E-03**
$k_{x/y}$	[-]	1E+6	1E+6	1E+6	1E+6	1E+6	1E+6
$\boldsymbol{A}$	[m^4/rad]	**1.703E-2**	**4.311E-2**	**6.048E-2**	**1.637E-2**	**2.598E-2**	**4.243E-2**

Torque arms

For the torque arms, a slightly different approach was used, since they incorporate stiffness and damping components in all 6 DOFs (see Table 10), and the joints are not directly connected to a rotating body. Figure 30 shows the adopted configuration. One key difference is the addition of one horizontal arm `TA`, symmetrically arranged and perpendicular to the gearbox shaft. In this configuration, `TA` was modeled as a rigid beam with three nodes. Its central node was connected to the gearbox body with a 1 DOF constraint, allowing the gearbox rotation (`bearing1`). The two outer nodes were connected to additional vertical beams (`TA_left` and `TA_right`) that were introduced to place the joints at the correct position, according to the SIMPACK model.

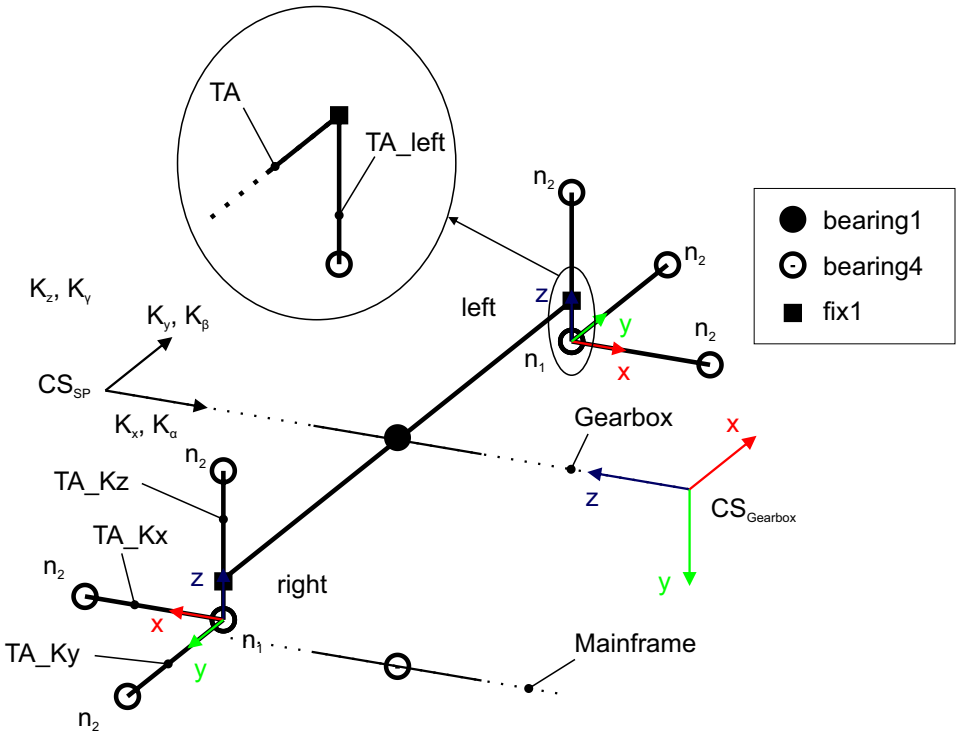

Figure 30: Adopted torque arm implementation: 6 DOF - 6 stiffness terms.

Similarly to the main bearings, a 3BM is introduced to model the joint characteristics. The same coordinate convention was applied, and the six beams were named after their location and orientation, `TA_left/right_Kx/Ky/Kz`. The convention from the SIMPACK reference model was adopted, defining left and right with respect to the downwind direction. As mentioned in the previous section, deploying a cardan shaft constraint at both beam ends was considered the most robust method to prevent coupling between bending, torsion, and longitudinal deformation. While this implementation was not working for the main bearings due to the connection to the rotating shaft, here it was applicable since the first nodes of the six support structures are connected to the non-rotating torque arm body (`TA`). Consequently, the transmission of forces and moments is purely characterized by the axial and torsional stiffness properties of each beam which could be calculated using Equation 6 and Equation 7. However, due to the additional presence of a rotational stiffness about the x-axis, $I_{p/\alpha}$ had to be derived as well. The value of the area moment of inertia I could be chosen arbitrarily. The resulting cross-sectional properties for the torque arm support structures are presented in Table 12.

Generator Support and Generator Coupling

Since the generator support is characterized by the same behavior as the main bearings, the identical approach was applied. However, since the support is modeled rigidly in SIMPACK, the calculated properties I_p and A are replaced by large values, while I_x and I_y are kept low.
To model the elastic coupling between the gearbox and the generator, the last 0.5 m of the generator beam element was replaced by an additional beam. Since the generator mass was assigned to its corresponding center of gravity with respect to the first body node, the reduction in length did not impact the weight distribution of the model. Yet, it allowed for introducing an additional element with a high torsional stiffness, but low longitudinal and torsional stiffnesses to avoid the transmission of axial and radial loads, as well as bending moments from the gearbox to the generator, and therefore imitating the elastic behavior of the couplings used in the SIMPACK model.

Table 12: Overview of cross-sectional beam properties for torque arm and generator support structures and resulting beam stiffnesses

		Torque arms			Gen. support	Coupling
Parameter		Kx	Ky	Kz	Kx / Ky / Kz	Kx / Ky / Kz
l	[m]	1	1	1	1	0.5
E	[N/m^2]	2E+11	2E+11	2E+11	2E+11	2E+11
G	[N/m^2]	1E+11	1E+11	1E+11	1E+11	1E+11
$I_{x/y}$	[m^4]	1	1	1	1E-5	1E-8
$\boldsymbol{I_p}$	[m^4/rad]	**1.2E-3**	**2.4E-3**	**2.4E-03**	**1E+09**	**1**
$k_{x/y}$	[-]	1E+6	1E+6	1E+6	1E+6	1E+6
$\boldsymbol{A}$	[m^4/rad]	**6.0E-4**	**1.2E-3**	**1.2E-2**	**1E+09**	**1E-6**

By comparing Figure 10 from subsection 2.1 and Figure 31, the difference between the original drivetrain implementation and the developed detailed structure is illustrated. The red, green, and blue lines represent the x-, y-, and z-axes, respectively, while the black lines and dots denote the beam elements and the body nodes. It can be seen, that the original model contains a tower top body that is connected to the tower one one end and supports the driveshaft on the other. In this configuration, the tower top represents the nacelle, and therefore all stationary components, while the shaft beam includes the rotating components.

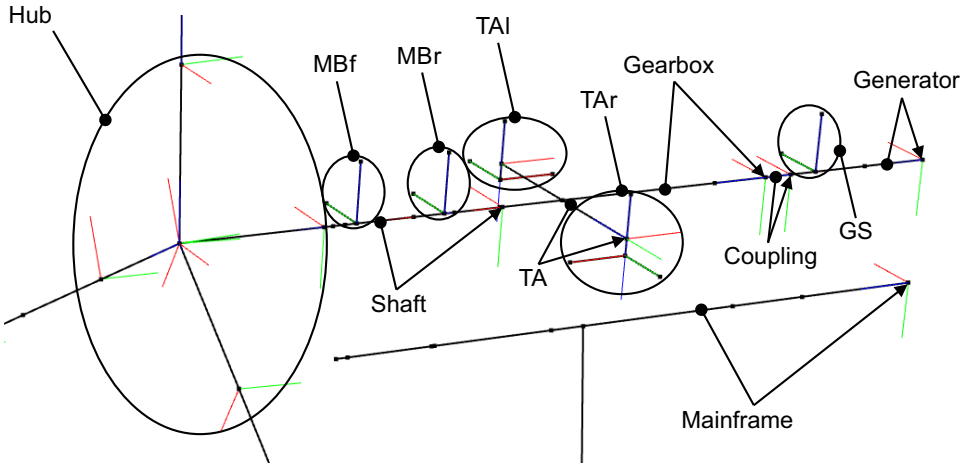

Figure 31: Adopted drivetrain implementation.

The tuning of the damping coefficients was carried out experimentally when comparing the SIMPACK and HAWC2 responses under statically applied loads and will be discussed in section 4.

Damping Calibration of the implemented joints

After implementing these features, simple static-load simulations were performed using both the SIMPACK and HAWC2 models. The primary goal was to provide an initial verification of the applied method and to fine-tune the damping characteristics of the implemented structure. Because the frequency of the implemented beams, and hence the response, mainly depends on the length and the calculated stiffness properties in Table 11 and Table 12, matching the frequencies of the SIMPACK model would have required a more detailed analysis and possibly an adaptation of the chosen approach. This step was therefore omitted at this stage. Nevertheless, it is important to note that matching the response frequencies in both models is critical for producing realistic fatigue load estimates for components such as the main bearings.
The tuning of the damping parameters was done iteratively, using the `damping_posdef`-command in HAWC2 and the equation for logarithmic damping (ξ) Equation 12. To account for the different frequencies, the amplitudes A_i were averaged over different numbers of periods n. The concept is illustrated in Figure 32 and Figure 33, which also shows the discrepancy in the response frequency. From this simple static-load simulation, it can also be estimated that both model responses converge to similar results, serving as a preliminary plausibility check for the implementation of the support properties. To get a better indication of the fidelity

of the individual support structures, the simulations were run for a decoupled driveshaft system, i.e., the connections between the shaft and gearbox, and gearbox and generator were suspended. The damping tuning approach was equally applied for the torque arms, while for the generator support, it was not necessary due to the high implemented stiffness.

$$\xi = \frac{1}{n} \ln\left(\frac{A_0}{A_n}\right) \tag{12}$$

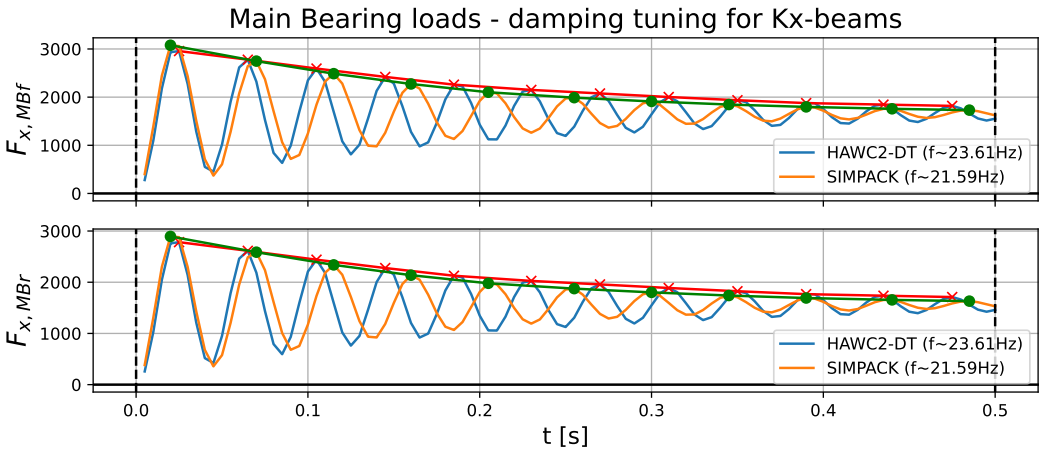

Figure 32: Visualization of damping tuning for the `MBf/r_Kx`-beams.

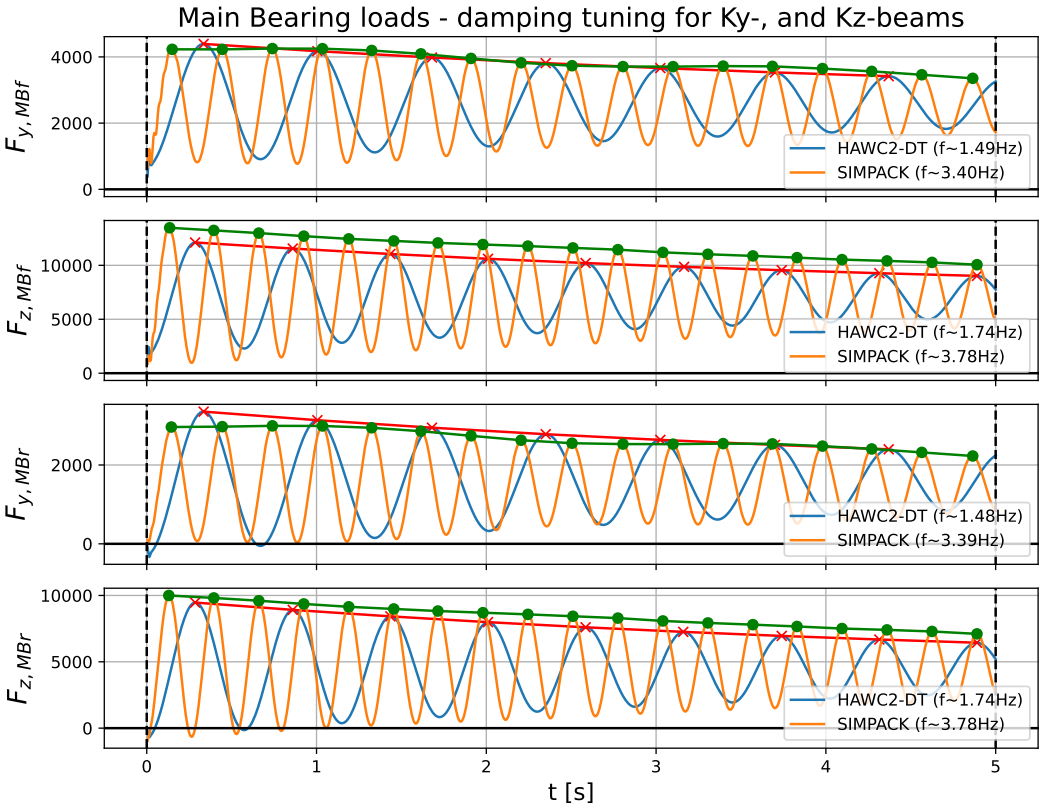

Figure 33: Visualization of damping tuning for the `MBf/r_Ky-`, and `MBf/r_Kz`-beams.

Rationale

The chosen approach, representing connections via a combination of three support beams, provided a practical and consistent framework and was considered the most evident choice, given the constraints of the HAWC2 environment and the Timoshenko beam elements. At the same time, this method enabled the integration of the dynamic behavior of the principal force elements of the SIMPACK reference drivetrain, and hence helped to address research question RQ 3-III.
Alternatively, the implementations with a single beam as well as a two-beam model were tested. In both cases, the beam's perpendicular bending stiffnesses were used to map the SIMPACK values K_x, K_y, and K_z, in addition to the longitudinal and torsional beam stiffness. However, one beam alone could not adequately capture all necessary stiffness components, and employing two beams resulted in a more complicated allocation of properties.
By utilizing the linear bending behavior of one-body beams (see Figure 14 in subsection 2.2), the applied method allowed for an accurate approximation of the stiffness conditions defined in the SIMPACK model. Importantly, this strategy could be applied accordingly across all major support structures, ensuring methodological consistency throughout the drivetrain representation. It also enabled the complete mapping of all involved stiffness terms without exception, making it both a comprehensive and an easily implementable solution within the limitations of the available modeling tools. Finally, the chosen method enables fast adjustments to different stiffness properties as each beam operates nominally independent of the other two.

Limitations

When mapping stiffness and damping characteristics in all six degrees of freedom (DOFs) to a node connected to multiple elastic beams, several limitations and assumptions must be acknowledged. First, this approach assumes that the equivalent stiffness behavior of the original system can be reproduced through the combined response of the beams. While the response for a single Euler beam under axially applied longitudinal and torsional loads will coincide with the deformation of a spring having a corresponding stiffness constant, this might not apply for 3BM under an arbitrary combination of loads and moments. As described in subsection 2.1 and seen Figure 14, a linear beam theory applies for single bodies in HAWC2. Yet, unwanted coupling effects might occur, when large forces and moments act in multiple directions simultaneously and deformations get large.
Although comparably low bending stiffnesses were implemented, coupling effects at the joints where no Cardan shaft constraints were employed, can be expected. Furthermore, a sufficiently large ratio between the support beam length and its deformation is required to ensure the validity of the linear bending assumption. Although not explicitly verified, the selected beam lengths were assumed to be reasonable in relation to the expected deformations. Another important aspect that has to be considered is the definition of the coordinate systems that are used for expressing the forces and moments. Since they are assigned to specific locations on the bodies, they also underlie translational and rotational displacements that impact the representation of the loads.

3.4. Step IV - Creation of an equivalent simple HAWC2 Model

Objective and Relevance

As previously mentioned, the SIMPACK model does not include structural components such as the nacelle housing, the gearbox housing, or the generator stator [22]. In the DTU 10MW RWT, however, an estimate of the entire nacelle mass is included [28]. To enable a comparison between the enhanced drivetrain implementation and the simple structure, the original HAWC2 model was adjusted to match the SIMPACK characteristics. This section presents the process of adopting the simple drivetrain representation and addresses research question RQ 3-IV.

Procedure

Since tower, hub, and blades remain unchanged, the focus was laid on matching the models by adjusting the simple shaft body and the tower top of the original HAWC2 configuration (see Figure 10). As mentioned earlier, in HAWC2, the `concentrated_mass` command attaches masses and mass moments of inertia to a position relative to a body node. This allowed for assigning the mass properties of the rotating components,

the mainshaft, the gearbox, and the generator to the simple shaft beam at their corresponding locations, i,e, their centers of gravity. Furthermore, the hub masses of the SIMPACK model and the original HAWC2 model showed a small discrepancy of approximately 3%, which was adjusted.

Equally, the relevant values of the mainframe were assigned to the appropriate position of the tower top beam element. To determine the coordinates of each mass center, the geometric configuration of both structures had to be compared, and the 5° tilt angle of the drivetrain had to be considered. The trigonometric relationship between the adjusted model (orange beams) and the detailed HAWC2 drivetrain layout is illustrated in Figure 34. All relevant mass centers are located in the y-z-plane of the local mainframe reference system, and their positions are expressed relative to this system, i.e. the geometric difference Δy corresponds to 0.69 m, and Δz to 6.5-6.15 m.

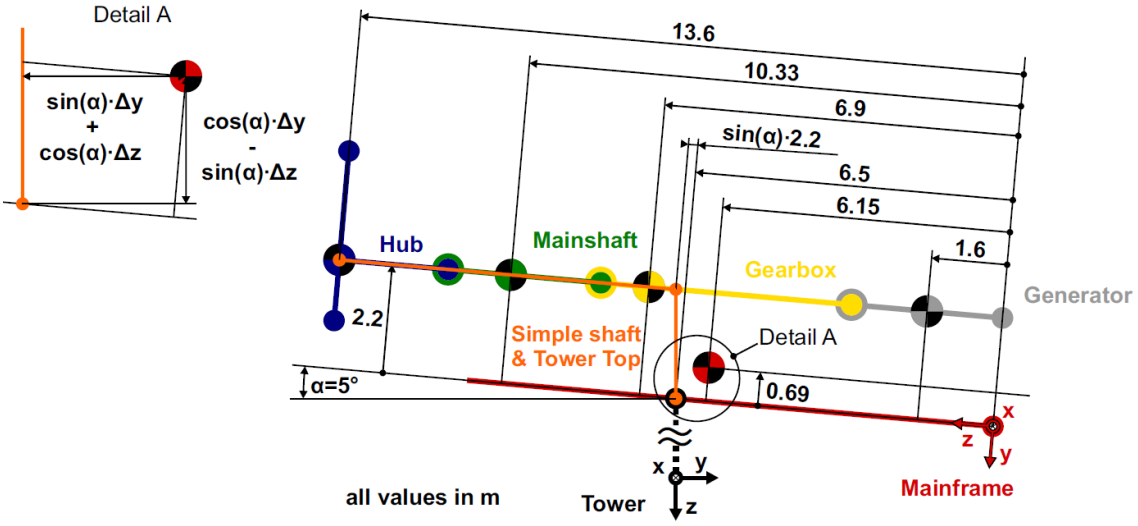

Figure 34: Original drivetrain implementation for the DTU 10MW RWT.

As a first verification step, the obtained overall mass of the SIMPACK model was compared with those of the detailed HAWC2 structure and the adjusted simple HAWC2 configuration. Since the SIMPACK model includes all components except the tower, the comparison included the entire drivetrain structure, the hub, and the blades. Additionally, the global CG locations of the three models were compared, and good agreement was observed. Table 13 presents the values for the overall mass and CG location in global coordinates and with respect to the last tower node. It can be seen that the deviations of the adjusted model also lie within 1.2 %, and therefore within acceptable boundaries. The difference between the SIMPACK and the detailed HAWC2 drivetrain configuration was already discussed in the limitations of Step II. The minor differences between the two HAWC2 models result from neglecting the additional support structures introduced in the previous step. Although the intention was to employ massless beams, small masses had to be assigned to ensure numerical stability of the solver.

Table 13: Overall mass and CG comparison of all three models with respect to the last tower node in global HAWC2 coordinates.

Model	y_{CG} [m]	**dev.** [%]	z_{CG} [m]	**dev.** [%]	m [kg]	**dev.** [%]
SIMPACK	-4.270	-	-2.222	-	437 157.4	-
HAWC2 DT	-4.219	1.2%	-2.224	0.1%	438 529.5	0.3%
HAWC2 adjusted	-4.313	1.0%	-2.233	0.5%	438 547.6	0.3%

Rationale

An alternative approach of matching newly implemented drivetrain characteristics in the simple model, would have been to adjust the masses and inertia terms that were assigned to the tower top and the shaft in the original HAWC2 setup. However, the applied approach was considered to be more comprehensible and more robust. After the trigonometric determination of the correct locations for allocating the individual

mass centers and inertia moments, this applied procedure offered a fast and simple method to obtain the same properties. To enable a more detailed comparison between the affected model components, the blades could have been excluded from the analysis. Yet, due to the significant weight of the drivetrain components, the associated impact was considered small.

Limitations

As mentioned above, disregarding the implemented support beams leads to small differences in the overall weight. Furthermore, since the masses and inertia terms are assigned to specific nodes, their distribution changes if these nodes experience displacements during operation. Due to the different structure in both HAWC2 models, this could have an impact on the dynamic behavior of the system. For instance, in the simple model, the shaft has constant stiffness properties across the length of the beam, while in the detailed model, the driveshaft consists of the rigid generator, the gearbox with reduced stiffness, and the flexible mainshaft. Therefore, the assigned masses and moments of inertia of these three bodies underlie slightly different boundary conditions. This potential discrepancy could be avoided by adjusting the shaft body of the simple model to match the stiffness distribution of the detailed model. Due to simplicity reasons, and because the expected influence was considered negligible, this was omitted.

3.5. Step V - Calibration of the first Torsional Natural Frequency

Objective and Relevance

After the implementation of the internal joint characteristics and the creation of the adjusted simple HAWC2 model, the objective was to match the first torsional eigenfrequency of both new models with the original DTU 10MW model and the detailed SIMPACK drivetrain. The torsional eigenfrequency of the drivetrain is the most relevant because it is most likely to be excited by operational torque fluctuations, poses a risk of resonance, and significantly affects both mechanical loads and control system behavior [18]. Therefore, a good agreement between the models is crucial.
To add, conducting a torsional mode comparison helps to assess whether the rotational drivetrain components were implemented accurately in terms of overall mass, stiffness, and moment of inertia [9].

Procedure

For a free-free mode with flexible shaft and tower, the design target for the torsional frequency of the original HAWC2 model was 1.8 Hz, with a structural damping of 0.89%. In the DTU 10MW documentation, four different mode scenarios are presented. In free-free mode, the drivetrain components are free to rotate, whereas in the free-fixed case, the generator rotation is locked. This additional constraint adds stiffness to the system and hence leads to an increase in the eigenfrequency. Furthermore, the cases of a rigid tower and rigid blades are compared with full flexibility [28].
Due to the lack of tower and blades in the SIMPACK model, the free-free and free-fixed modes for stiff blades and tower were analyzed. In the following, the approach of tuning the torsional frequency for the detailed drivetrain model is presented.
The drivetrain configuration can be simplified to a dynamic system consisting of a beam with equivalent stiffness $k_{t,eq}$, and two attached mass moments of inertia J_r one side, and $J_g = n_{GB}^2 J_{GB} + n_{Gen}^2 J_{Gen}$ on the other end for the free-free mode and the rotor inertia only for the free-fixed case [36]. In this simplified application, n_{GB} represents the ratio of the rotational speed of the gearbox and n_{Gen} the ratio of the generator speed with respect to the rotational speed of the inertia J_r. Since both the gearbox and the generator are modeled as rigid bodies, their inertias can be combined. The two systems are illustrated in Figure 35 and can be used to calculate the torsional eigenfrequencies.

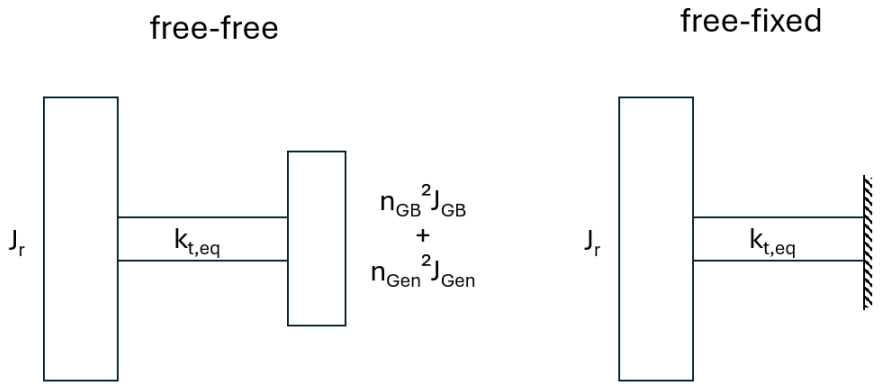

Figure 35: Equivalent drivetrain with single stiffness and inertia for free-free and free-fixed modes.

For the following derivation, $J_g = n_{GB}^2 J_{GB} + n_{Gen}^2 J_{Gen}$ is used. Applying Newton's second law for rotation, i.e. $\sum M = J\ddot{\varphi}$, the undamped eigenfrequencies for both cases can be derived. Using $\varphi = \varphi_g - \varphi_r$ as the relative angular deformation across the beam length, the moment around the beam axis can be written as $M = \varphi k_{t,eq}$. For the simple free-fixed beam, the equation of motion can then be written as:

$$k_{t,eq}\varphi = J_r\ddot{\varphi} \tag{13}$$

Assuming harmonic oscillation, i.e. $\varphi(t) = A_0 e^{i\omega t}$ and $\ddot{\varphi}(t) = -\omega^2 A_0 e^{i\omega t}$, with ω being the angular frequency and A the amplitude of the oscillation, the natural frequency $f_{n,ffix}$ can be obtained:

$$f_{n,ffix} = \frac{\omega_{n,ffix}}{2\pi} = \frac{1}{2\pi}\sqrt{\frac{k_{t,eq}}{J_r}} \tag{14}$$

Similarly, the eigenfrequency for the free-free mode $f_{n,ffree}$ can be calculated and writes:

$$f_{n,free} = \frac{\omega_{n,ffree}}{2\pi} = \frac{1}{2\pi}\sqrt{\frac{k_{t,eq}(J_r + J_g)}{J_r J_g}} \tag{15}$$

Equation 14 and Equation 15 were used to tune the torsional eigenfrequency of the new drivetrain.

Free-Fixed Mode Calibration

First, the drivetrain was locked at the first generator node to simulate the free-fixed system. To maintain consistency with both the SIMPACK and the original HAWC2 model, the general goal was to preserve as much of the provided body data as possible. However, the initial torsional frequency of the new drivetrain model was too high, requiring adjustments to either the rotor inertia J_r or the equivalent stiffness $k_{t,eq}$ (see Equation 14).
Since the rotor inertia as well as the shaft properties were implemented in accordance with the provided models, the choice was made to adjust the torsional stiffness of the gearbox body, which was implemented as a rigid beam. This was done by iteratively lowering the value of the shear modulus Guntil the free-fixed torsional frequency matched the ones from the original HAWC2 and the SIMACk model. To allow for a sanity check of the final result, i.e., the magnitude of G, the same polar moment of inertia I_p as in the original HAWC2 shaft was used. During this process, G was reduced from a value of 7.96E+16 to 1.596E+11 Nm^2, which was still by a factor of approximately 2 higher than the 8.08E+10 $\mathrm{N/m}^2$ used for the original shaft.

Free-Free Mode Calibration

Second, the torsional frequency was tuned for the unlocked system. As described in [36], the inertia of the high-speed shaft side has to be scaled with the square of the gearbox ratio to account for the additional kinetic energy. In the case of the original shaft, this was done for the generator inertia [28]. From Equation 15, where $J_g = n_{GB}^2 J_{GB} + n_{Gen}^2 J_{Gen}$, it can be seen that most variables, namely the torsional spring constant $k_{t,eq}$, the inertia terms J_r, J_{GB} and J_{Gen}, as well as the rotor speeed ratio n_{Gen} (equivalent to the overall gearbox ratio),

were already fixed. As a consequence, the only adjustable parameter was n_{GB}, which can be interpreted as an effective, averaged gearbox ratio, condensing all three internal rotational velocities of the gearbox into a single representative value.
However, during the calibration, the value for n_{GB} that was required to match $f_{n,ffree}$, was 1, leading to the assumption that the inertia values taken from the SIMPACK model already included the kinematic scaling of the three gearbox stages and were hence defined with respect to the low-speed shaft. This circumstance was supported by the fact that the provided generator inertia was exactly equivalent to 50x1500.5 kgm2.
With the implementation method used for the adjusted HAWC2 model, as described in Step IV, the torsional frequencies for this model did not require any tuning. The reasons for this are one hand, the fact that the same shaft beam as in the original model is used. Hence, its equivalent driveshaft torsional stiffness constant $k_{t,eq}$ is identical to the other two models. On the other hand, the same mass moment of inertia distribution about the shaft axis as in the detailed configuration is applied.

Damping Calibration of driveshaft

Subsequently, the damping of the drivetrain was tuned iteratively using the built-in HWAC2 command `damping_posdef`. The chosen Rayleigh damping parameters are directly multiplied to the moments of inertia in the stiffness matrix and inserted in the damping matrix [34]. The obtained frequencies and logarithmic damping terms for the two new models are compared with the values from the original HAWC2 and the SIMPACK model in Table 14. Overall, the results lie within acceptable deviations. Both the equivalent shaft torsional stiffness constant $k_{t,eq}$ as well as the equivalent shaft torsional damping constant $c_{t,eq}$ depend on these results and consequently show the same level of agreement.

Table 14: Natural frequencies and damping for the rigid free-fixed and free-free shaft torsion modes

	$f_{\text{n\_ffixed}}$ [Hz]	log. damping [%]	$f_{\text{n\_ffree}}$ [Hz]	log. damping [%]
HAWC2 original	0.612	4.80	4.003	31.42
SIMPACK	0.611	4.80	3.889	31.39
HAWC2 DT	0.609	4.83	3.972	31.40
HAWC2 adjusted	0.611	4.81	3.975	31.25

Rationale

In the simple HAWC2 drivetrain layout, the shaft has a length of 7.1 m, while in the new configuration, the flexible mainshaft beam is only 3.16 m long. This reduction influences the overall stiffness and explains why additional flexibility had to be added in the new model to match the free-fixed torsional frequency. Moreover, in the SIMPACK layout, some components inside the gearbox are modeled as flexible bodies, and therefore, lowering their overall shear modulus seemed a reasonable approach.
Overall, the described procedures offered a way to obtain comparable eigenfrequencies without requiring major modifications to the structure or its dynamic properties, and were therefore considered appropriate for addressing research question RQ 3-V.

Limitations

While the chosen approach relies on the available data from the SIMPACK reference model, representing the entire gearbox with a single beam of equivalent flexibility cannot fully capture the behavior of a detailed gearbox model that includes both flexible and rigid components. Consequently, some local effects and dynamic interactions within the gearbox are necessarily neglected. Nevertheless, because the same simplification was applied in the original HAWC2 model, this approach was considered a reasonable compromise between model fidelity and computational efficiency for the purposes of this study.
In this approach, only the first torsional eigenfrequency was matched, while other eigenfrequencies of the drivetrain were disregarded, potentially neglecting higher-order dynamic effects.

4. Simulations and Results

To verify the implemented drivetrain structure, a detailed analysis was carried out, comparing the SIMPACK (SP) model with the detailed HAWC2 turbine model, in the following referred to as H2-DT. To determine the level of agreement as well as to investigate where occurring discrepancies might originate from, several load case scenarios were analyzed and presented in subsection 4.2. Subsequently, in subsection 4.3, the HAWC2-DT implementation is compared with the adjusted, simple model (H2-AD) to see the impact of the enhanced drivetrain model on the overall response. To ensure comparability, the SIMPACK model was tested, and some modifications were necessary.

4.1. SIMPACK model modification

First, it was noticed that in the uploaded version of the SIMPACK drivetrain model, one relevant force element, namely `$S_gearbox.$F_st3_w_gear_to_st3_p_gear` and representing the connection between the wheel and pinion of the third gearbox stage, was falsely deactivated. Additionally, the position of the hub's center of mass had to be corrected, as it was initially assigned to the shaft–hub connection point. Due to the missing blades in the model, the hub body includes the inertia and mass of the three blades. The combined CG was determined and changed accordingly. Since this location varies as the blades deflect, this definition is only accurate for rigid blades. However, for the sake of simplicity, these variations were neglected in the simulations but were accounted for in the analysis of the relevant cases.

After these adjustments, a simple simulation was run with no external loads, no gravity, and no rotational speed. The results showed the presence of high internal residual loads, particularly in the F_x Components. It was discovered that these partially occurred as a consequence of relatively large initial displacements between markers that were used to define connecting force elements between two adjacent bodies. Because of the four-point drivetrain support and the complexity of the dynamic model, the system is overdetermined. Consequently, minor inaccuracies in component connections induce internal stresses that are amplified according to the specified joint stiffnesses. To compensate for the most impactful initial marker offsets, the addition of nominal bushing displacements was tested, and the implementation with the best results, i.e., lowest residuals, was used for the model comparison. Figure 36 shows a comparison of the residual drivetrain loads before and after this modification for the front main bearing. In particular, the reduction of the axial force component F_x is significant, from more than 33 000 kN, being approximately 20 times higher than the thrust at rated wind speed, to 5 kN.

In addition to this, the mode of angle calculation, defined within some force elements, was changed from `All Angles < 10 deg` to `Alpha > 10 deg` to obtain valid results for these components. This was particularly relevant for the force elements of the front and the main bearing.

Although these modifications produced more plausible results, they also introduced drawbacks, as will be shown later, highlighting the inherent complexity of the model.

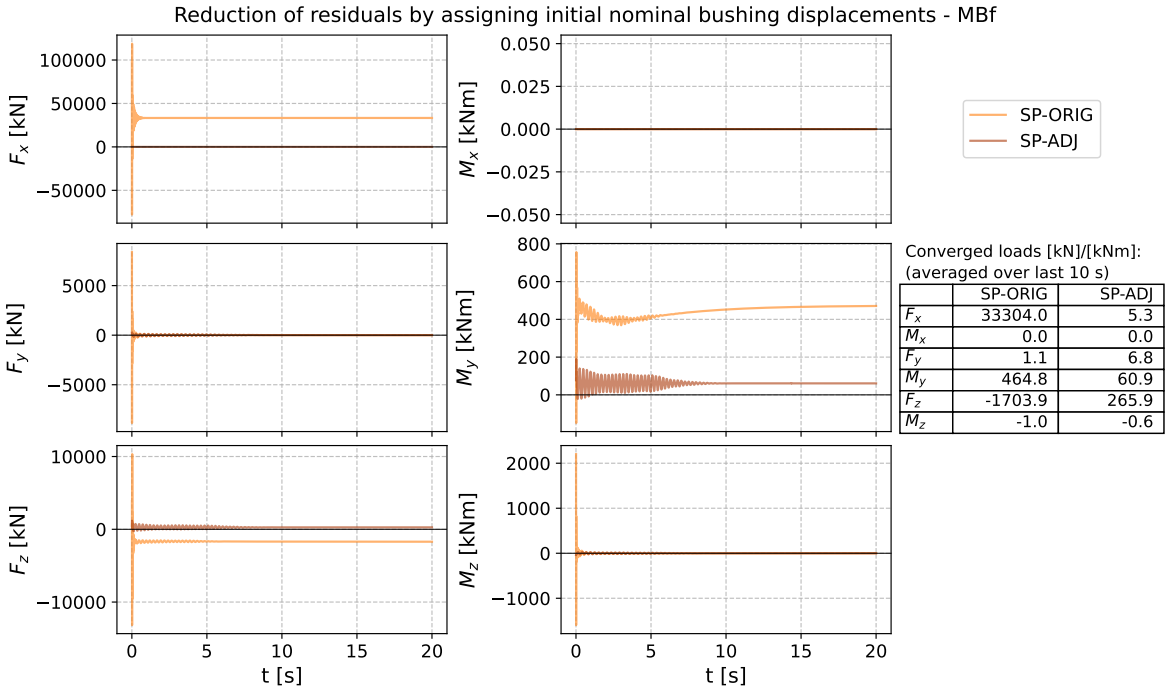

	SP-ORIG	SP-ADJ
F_x	33304.0	5.3
M_x	0.0	0.0
F_y	1.1	6.8
M_y	464.8	60.9
F_z	-1703.9	265.9
M_z	-1.0	-0.6

Figure 36: Impact of introducing nominal bushing displacements on residual loads in SIMPACK model.

4.2. Model verification

An overview of the load cases used for the model verification is presented in Table 15. It includes the simulation-ID, the type of external loads that are applied at the rotor or the hub, and whether gravity g and tower or blade flexibility are included in the calculations. Furthermore, the initial rotor speed $\omega_{r,t0}$, the simulation time t_s, the sampling frequency f_s, and the objective of the specific load case are specified in the table. For IDs 1 and 2, a decoupled driveshaft was used, i.e. shaft, gearbox, and generator were decoupled in both models.

Table 15: Overview of general simulation parameters.

ID	Ext. loads	g	ω_r [rad/s]	Tow.	Bl.	t_s [s]	f_s [Hz]	Objective
1	✗	✗	0	rig.	rig.	30	200	Decoupled driveshaft; To derive if there any residual forces are present in the system.
2	Hub and GB: F_x = 3000 kN F_y = 1000 kN	✓	0	rig.	rig.	30	200	Decoupled driveshaft; To enable a comparsion of the individually implemented support structures with the SIMPACK model.
3	✗	✗	0	rig.	rig.	30	200	To check whether any internal residual forces are present in the coupled system.
4	✗	✓	0	rig.	rig.	30	200	To check the accuracy of the load distribution on the implemented support structure under standstill conditions for the coupled system.
5a	F_x = 3000 kN F_y = 1000 kN	✓	0	rig.	rig.	30	200	Two different steady external hub load scenarios; To compare the response of the SIMPACK and the detailed HAWC2 model.
5a	F_x = 1500 kN F_y = 500 kN	✓	0	rig.	rig.	30	200	
6a	V_0 = 7 m/s	✓	0	rig.	rig.	120	200	Three steady inflow conditions are examined to analyze the level of agreement of the implemented HAWC2 drivetrain model.
6b	V_0 = 11 m/s	✓	0	rigflex.	rig.	120	200	
6c	V_0 = 15 m/s	✓	0	rig.	rig.	120	200	
7a	V_0 = 7 m/s	✓	0	rig.	rig.	120	200	Entirely rigid DT structure, and rigid Coupling only, to show the impact of the implemented joint features.
7b	V_0 = 7 m/s	✓	0	rig.	rig.	120	200	
8	$V_{0,turb}$ = 7 m/s	✓	$\omega_r(t)$	flex.	flex.	700	200	Turbulent simulation for a mean wind speed of V_0 = 7 m/s; To analyze the response under realistic conditions.

Table 16: Overview of wind-related simulation parameters.

Type	Inflow Angle*	Shear format	TI**	Turb. Model	Tower Shadow
Steady	0°	Constant wind	0	None	None
Turbulent	0°	Power law, α = 0.2	0.217	Mann	Potential flow
*Combined yaw, tilt, and rotation angle wrt the global coordinate system.					
**Turbulence intensity calculated according to IEC standard for turbulence class A [31].					

General simulation approach

To maximize the comparability of the solutions from both modeling environments, SIMPACK and HAWC2, it was important to use the same simulation parameters, wherever possible. These included the sampling frequency and external conditions such as gravity. In both models, the user-defined initial conditions are applied instantaneously, resulting in a transient period that needs to be disregarded in the comparison. These transients were used for the determination of damping gradients, as shown in subsection 3.3.
Additionally, it was crucial to apply the external loads identically on the hub center. In both models, external steady loads can be applied at the location of the hub center. However, when modeling a time-marching simulation under specific wind conditions, the hub loads in the HAWC2 model result from inflow-induced loads acting on the entire rotor. A more detailed description of how the external loads were obtained and applied in each specific case is provided in the corresponding sections.

As mentioned previously, an integral part of the accurate comparison of the loads between the different models is the use and handling of the coordinate system in which the results are presented. As a general rule, the 5°-tilted mainframe coordinate system of both models was used to save the results for the presented load cases. However, since the definition of the axes-orientations between both models is different, the SIMPACK convention was used, and the HAWC2-components were transferred accordingly. The mainframe coordinate system in SIMPACK corresponds to the global coordinate system, shown in Figure 15a, positively rotated around the y-axis by 5°. Hence, the following relations can be derived:

- $x_{MF,SP} = -z_{MF,H2-DT}$
- $y_{MF,SP} = x_{MF,H2-DT}$
- $z_{MF,SP} = -y_{MF,H2-DT}$

One exception to this rule is the right torque arm, where the coordinate system is rotated 180° around the z-axis compared to the left counterpart (see Figure 31). Therefore, the x- and y-components of the right torque arm have opposite signs, which will be accounted for. If not mentioned otherwise, the MF,SP coordinate system is used in section 4. As a reference for the different presented scenarios, Figure 37 shows the rotor speed, the pitch angle, and the aerodynamically induced rotor torque and thrust for the entire operational range.

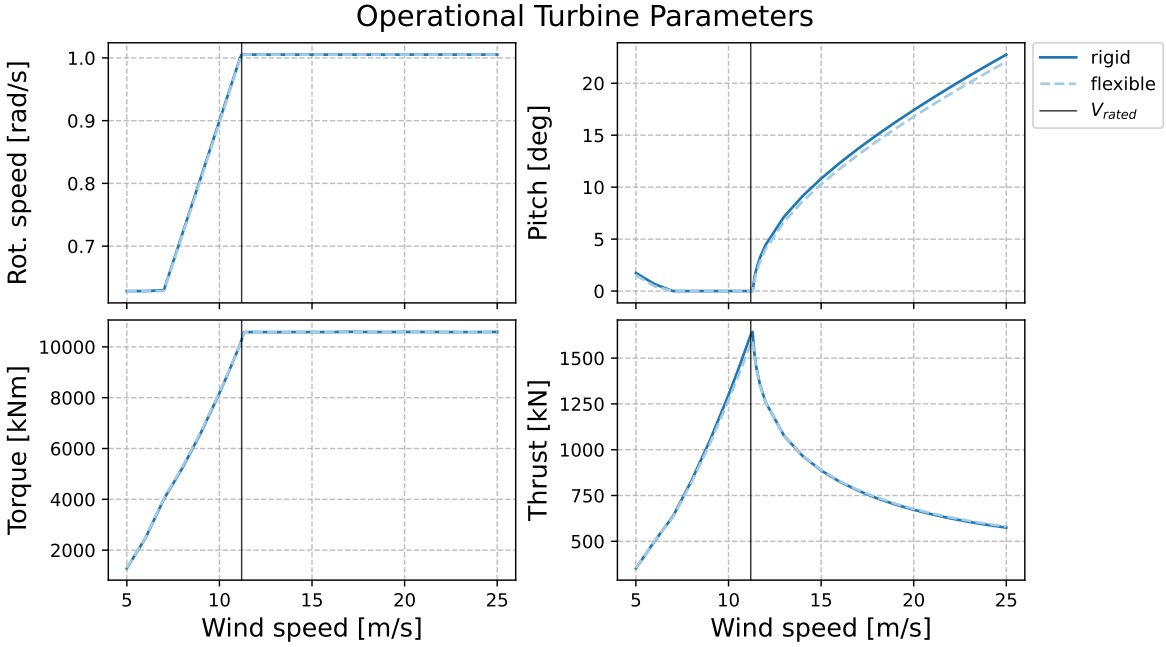

Figure 37: Turbine parameters across the entire operational range for rigid and flexible blades.

C1 - Determination of residual forces in both models

As a first step, the SIMPACK and the new HAWC2 model were decoupled to determine if any internal, residual forces were present when no external forces and no gravity were acting on the system. Apart from the visual check with the visualization tool, this served as a test to see whether the implemented HAWC2 drivetrain structure was set up properly. The presence of the small residual forces in the SIMPACK model, on the other hand, originates from the complex, overdetermined mechanical system. Small initial, spatial displacements between two related markers can lead to high residual forces due to the large applied stiffness terms ($F = K\Delta d$). This, and the complex setup within the gearbox, can lead to discrepancies presented in Figure 38 and Table 17. The table includes all residual forces and moments above/below a threshold of ± 1 kN/1kNm. It can be seen that mainly the F_x-components of the four-point support structure, and the M_z-components of the torque arms were affected in the decoupled system. However, since the residuals depend on the interconnection between all components, they were also analyzed for the coupled system (see Load Case 3).

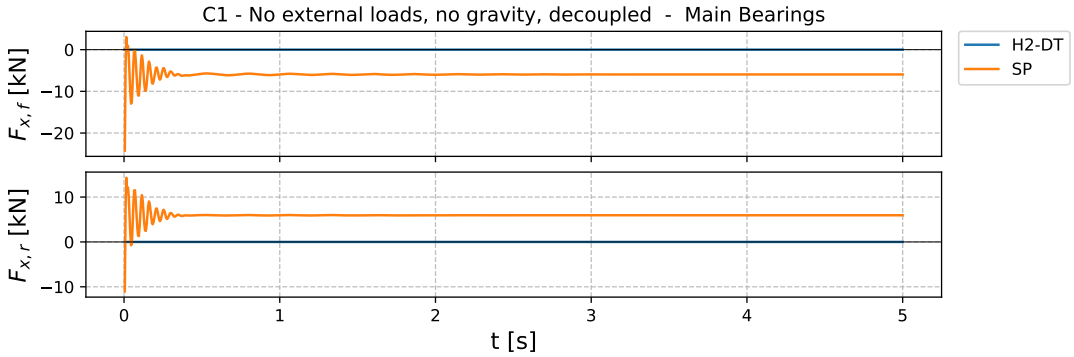

Figure 38: Residual F_x-forces for front and rear main bearing.

Table 17: Overview of residual forces for the decoupled system, no gravity and no external forces.

Load Channel	HAWC2-DT	SIMPACK
MBf F_x [kN]	0.000	-5.945
MBr F_x [kN]	0.000	5.945
TAl F_x [kN]	0.000	-2.462
TAr F_x [kN]	0.000	2.462
TAl M_z [kNm]	0.000	-4.737
TAr M_z [kNm]	0.000	-4.737

C2 - Comparison of individual joint response

Next, static loads in x- and y-directions were applied on the hub to investigate the response of the implemented bearing structures, and at the last gearbox node to analyze the behavior of the modeled torque arms. The system was again decoupled to analyze the behavior independently of any interaction between the different support structures. For this purpose, the gravity was activated, resulting in a force component in the vertical z-direction and an additional small force in x-direction, due to the 5° tilt angle of the drivetrain. The applied forces were 3000 kN, in x-direction, corresponding to approximately twice the thrust at rated wind speed, and 1000 kN in y-direction since side-side forces are considerably smaller. The results, including the initial transient period for both main bearings and the torque arm support structures, are shown in Figure 39 to Figure 42. On the right, they include a table comparing the converged loads of both models. For this purpose, the average of the last 10 simulation seconds is taken.
Apart from the frequency of the response, the main bearing loads show overall a good agreement and indicate a successful implementation of the corresponding stiffness properties. The negligible discrepancies in the converged solutions can be explained by the nature of the different implementations. The beam model used in the HAWC2 drivetrain structure is more impacted by coupled forces. As explained in section 3, the stiffness parameters are distributed on three perpendicular beams, each characterized by a corresponding

longitudinal and torsional stiffness. A displacement of the bearing node will lead to a beam deformation and consequently influence the stiffness properties of the deformed body. Furthermore, it was shown in Step III of section 3 that, despite very small bending stiffnesses, small residual forces and moments are transferred to the neighboring beams (see Figure 28). This can be particularly seen in the M_x-components of both main bearings. Due to the implemented `bearing1`-constraint with free rotation about the x-axis, these moments should be zero, yet small residual contributions remain.

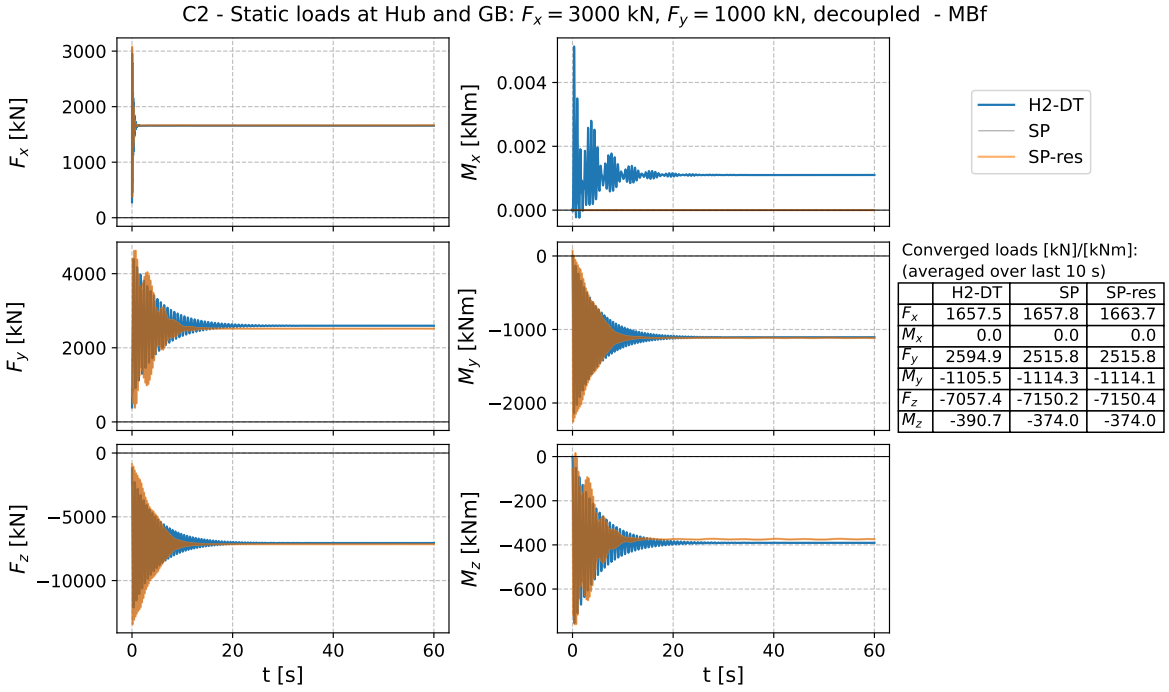

	H2-DT	SP	SP-res
F_x	1657.5	1657.8	1663.7
M_x	0.0	0.0	0.0
F_y	2594.9	2515.8	2515.8
M_y	-1105.5	-1114.3	-1114.1
F_z	-7057.4	-7150.2	-7150.4
M_z	-390.7	-374.0	-374.0

Figure 39: Front main bearing response for static loads and a decoupled system.

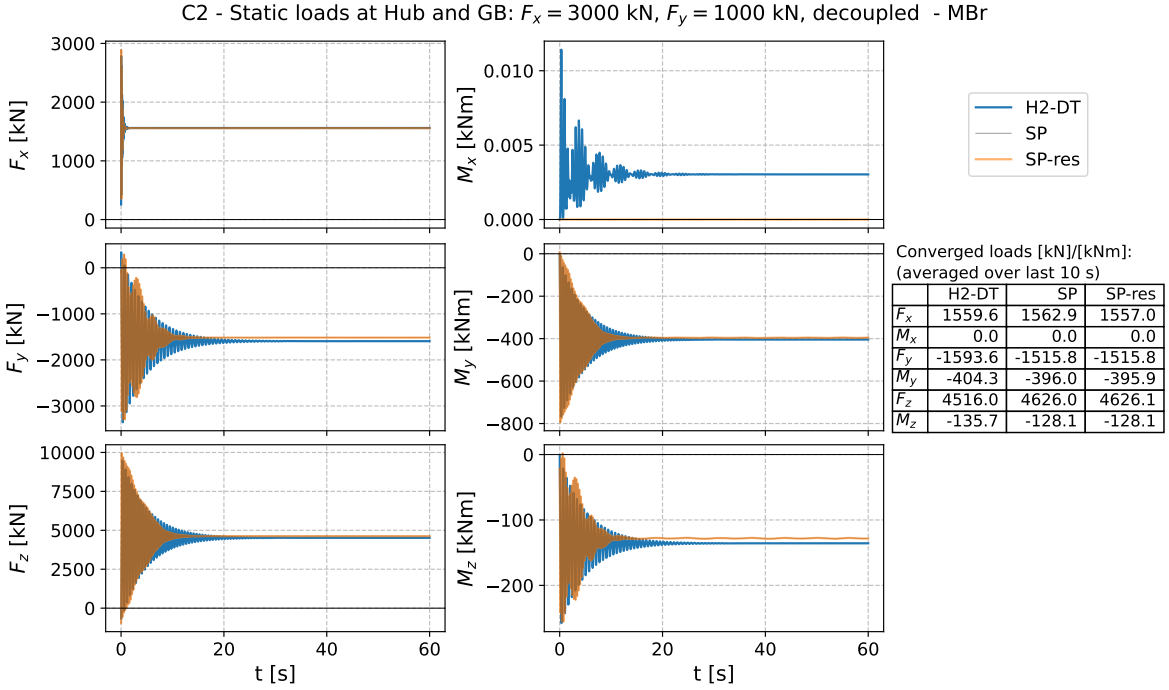

	H2-DT	SP	SP-res
F_x	1559.6	1562.9	1557.0
M_x	0.0	0.0	0.0
F_y	-1593.6	-1515.8	-1515.8
M_y	-404.3	-396.0	-395.9
F_z	4516.0	4626.0	4626.1
M_z	-135.7	-128.1	-128.1

Figure 40: Rear main bearing response for static loads and a decoupled system.

The level of agreement for the torque arm response is slightly lower. As discussed previously, the gearbox model in the developed HAWC2 drivetrain structure does not map the complexity of the SIMPACK model. A major difference is that in the H2-DT model, the gearbox is assumed to be a rotationally symmetric element with the mass center being on its axis. However, in the SIMPACK model, the CG is slightly shifted to the left side, due to the third gearbox stage (see Figure 22). Due to the small $y_{SP,MF}$-coordinate of the mass center of less than 0.03 m, this lateral offset was neglected in the HAWC2 model. The large difference of 80 kNm in the M_z-components occurs because the force application point in both models differs. While in the HAWC2 model, the last gearbox node is fixed to the first shaft, as illustrated in Figure 15a, in SIMPACK, the connecting force element is located 0.4 m in the x-direction towards the second shaft node, resulting in an additional M_z-contribution. Finally, in the drivetrain implementation of HAWC2, the geometric dimensions imported from the SIMPACK model were rounded to the nearest centimeter, which introduced small discrepancies in the results, particularly under high-load conditions.

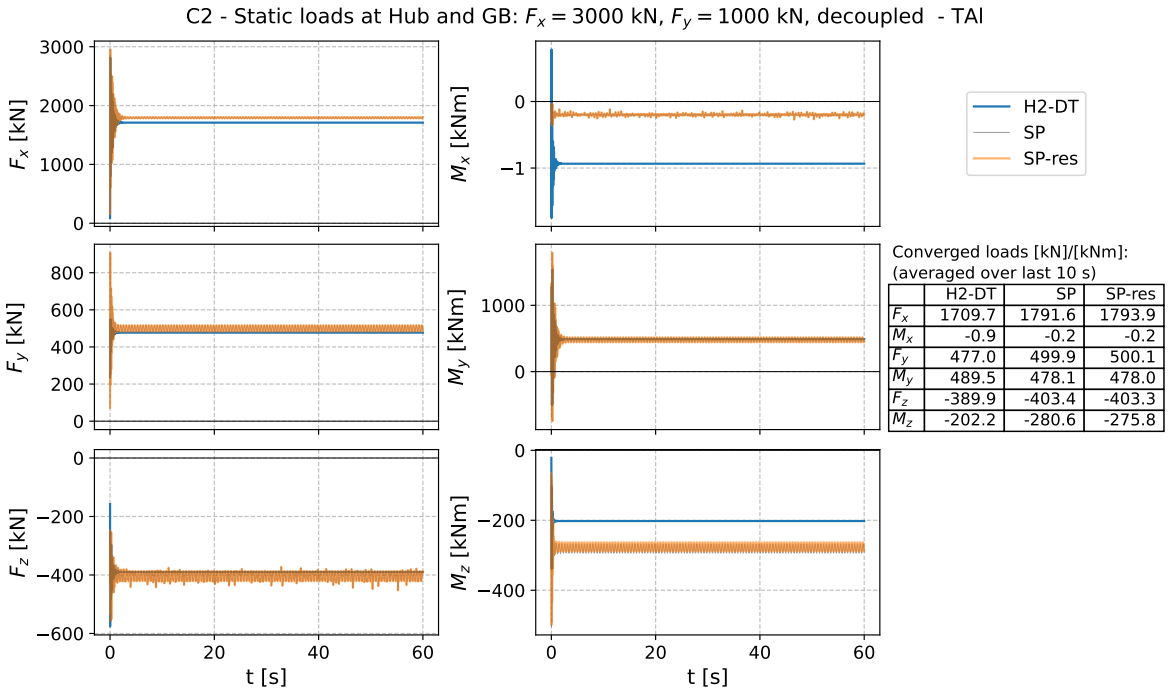

	H2-DT	SP	SP-res
F_x	1709.7	1791.6	1793.9
M_x	-0.9	-0.2	-0.2
F_y	477.0	499.9	500.1
M_y	489.5	478.1	478.0
F_z	-389.9	-403.4	-403.3
M_z	-202.2	-280.6	-275.8

Figure 41: Left torque arm response for static loads and a decoupled system.

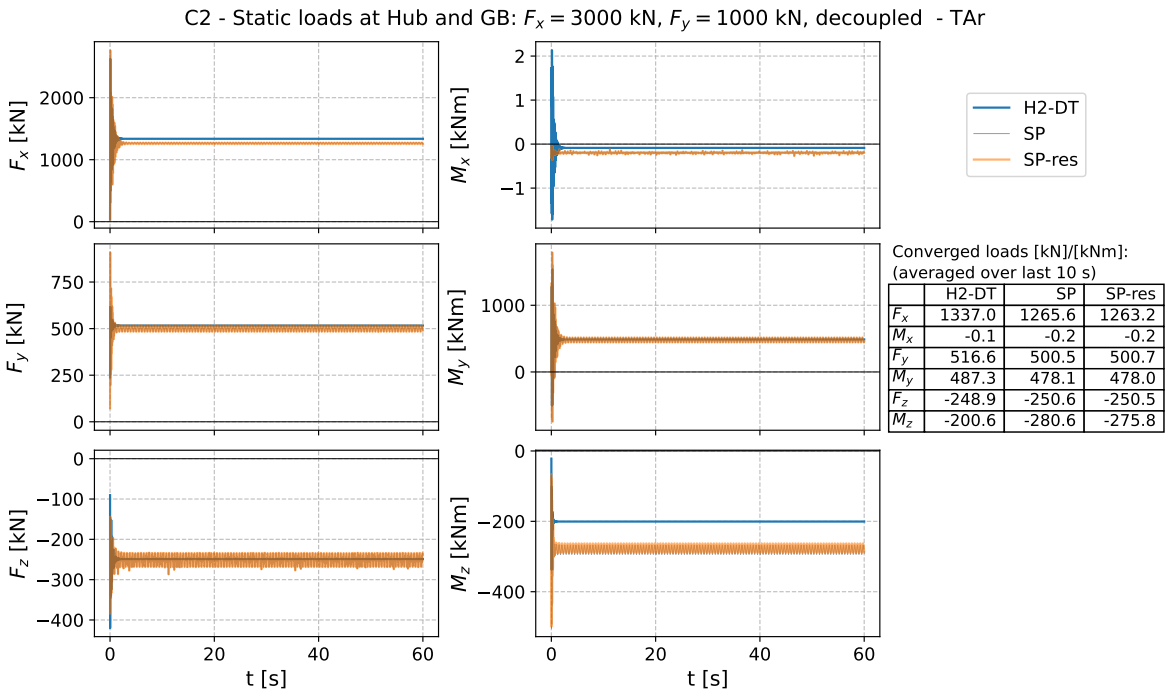

	H2-DT	SP	SP-res
F_x	1337.0	1265.6	1263.2
M_x	-0.1	-0.2	-0.2
F_y	516.6	500.5	500.7
M_y	487.3	478.1	478.0
F_z	-248.9	-250.6	-250.5
M_z	-200.6	-280.6	-275.8

Figure 42: Right torque arm response for static loads and a decoupled system.

C3 - Determination od residuals in coupled system

For load case 3, the gravity was deactivated, and external loads were set to zero. It served to determine all the remaining internal forces in the coupled system. Looking at Table 18, it can be seen that the residuals in the SIMPACK drivetrain model are significantly larger than in the decoupled system. The additional active joint constraints generate internal stresses that will be superimposed on those induced by external loads. As previously mentioned, some of these residuals depend on the azimuthal shaft positions. Therefore, the purely internal SIMPACK loads were determined for each of the following load cases and subtracted from the outcome of the actual simulation. This should enable a better comparison of both models.

The largest residual forces are present in the rear bearing, indicating inaccuracies in the mainshaft-gearbox connection. In SIMPACK, the force element that connects the shaft with the gearbox is modeled with a stiffness of 1E+12 N/m in all three translational directions and 1E+12 Nm/rad rotational stiffness around the y- and the z-axis (see Table 10). Consequently, minor offsets between the two connecting markers will lead to large residuals, as can be seen in Figure 43 for the rear bearing. The results for the remaining components are presented in section 6.

Table 18: Overview of residual forces for the coupled system for a threshold of ± 1 kN/kNm.

Load Channel	HAWC2-DT	SIMPACK
MBf F_x [kN]	0.000	5.323
MBf F_y [kN]	0.000	6.953
MBf F_z [kN]	0.000	265.385
MBr F_x [kN]	0.000	16.989
MBr F_y [kN]	0.000	-2.842
MBr F_z [kN]	0.000	-530.829
TAl F_x [kN]	0.000	-17.158
TAl F_y [kN]	0.000	-2.056
TAl F_z [kN]	0.000	133.016
TAr F_x [kN]	0.000	-5.154
TAr F_y [kN]	0.000	-2.056
TAr F_z [kN]	0.000	132.427
MBf M_y [kNm]	0.000	60.752
MBr M_y [kNm]	0.000	47.028
TAl M_y [kNm]	0.000	34.997
TAl M_z [kNm]	0.000	-1.058
TAr M_y [kNm]	0.000	34.997
TAr M_z [kNm]	0.000	-1.058

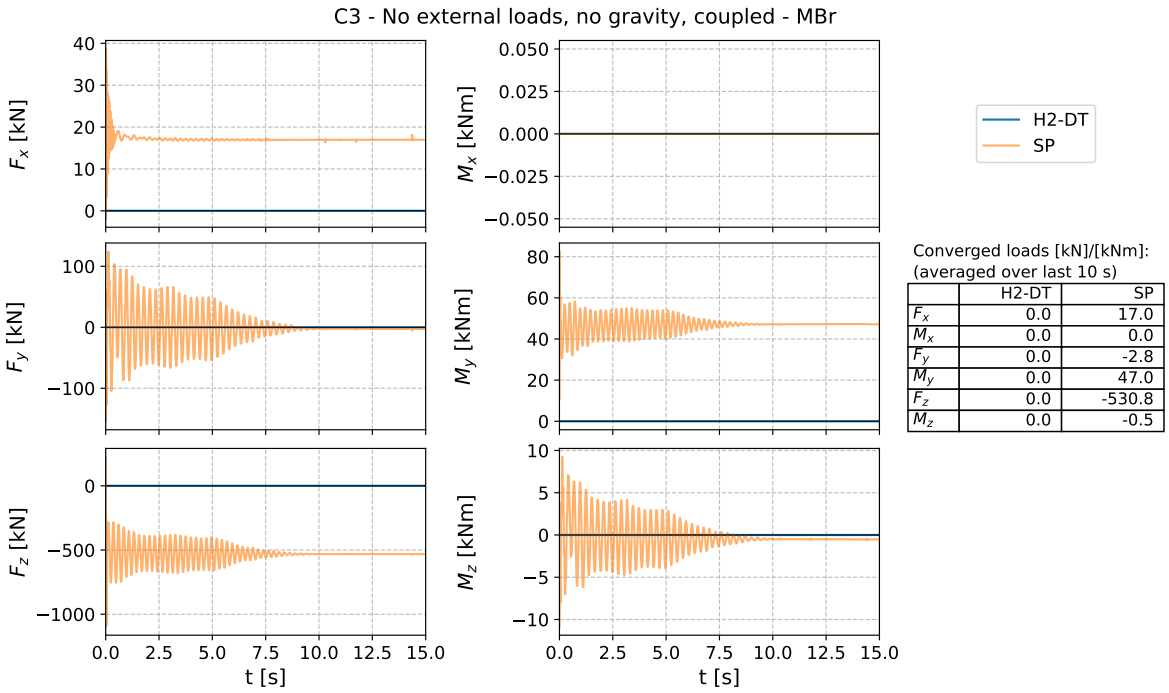

Figure 43: Rear main bearing residual forces and moments for the coupled drivetrain.

C4 - Analysis of mass distribution of coupled system

The objective of load case 4 was to see how both coupled models compare when no external forces act upon them but gravity. Furthermore, the impact of the residual forces on the model comparison, determined in the previous load case, is illustrated. By comparing the SP-curve with the SP-res-curve in the figures below, a slight overall improvement in the level of agreement between the SIMPACK and the HAWC2 models can be noticed. Yet, when comparing the converged values, this is not the case for all load components. As expected, the best results were obtained from the main bearing response, followed by the rear bearing and then the torque arms.
In general, it can be observed that the relative discrepancy, i.e., the difference between the load components of both models, relative to their values, is larger for small reaction forces and moments. This is plausible since inaccuracies due to the different implementation methods dominate when no or low external loads are applied (see residuals). They become increasingly irrelevant for larger imposed loading conditions. This is illustrated by comparing the results of load cases C2 and C4.

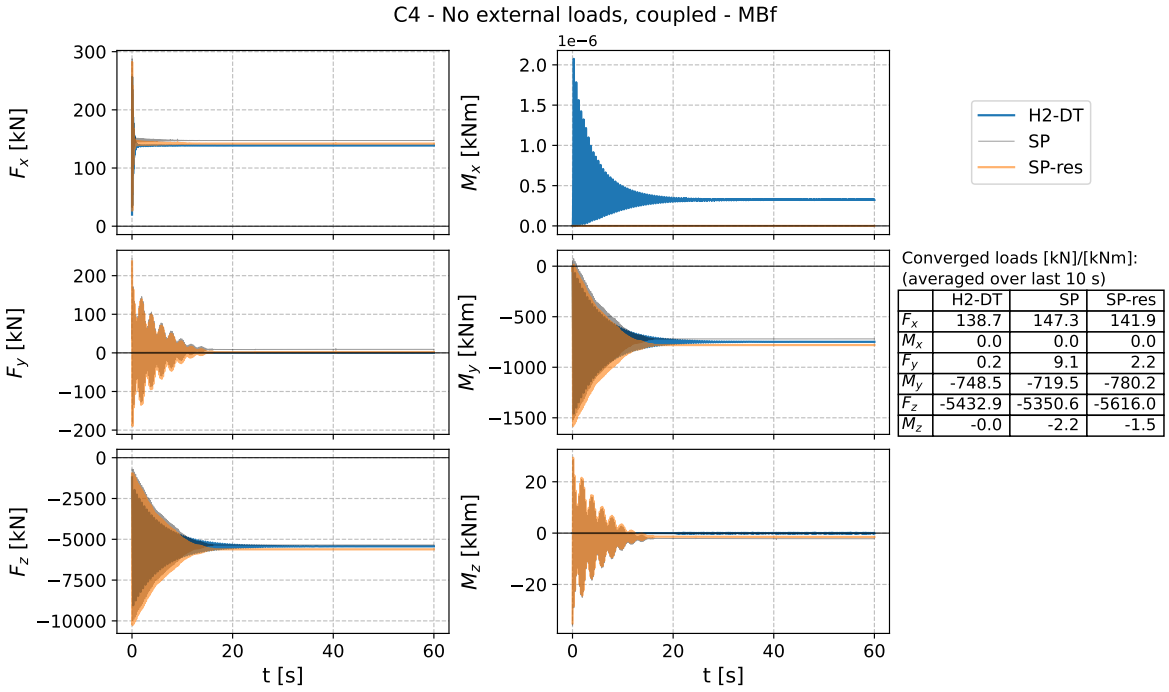

	H2-DT	SP	SP-res
F_x	138.7	147.3	141.9
M_x	0.0	0.0	0.0
F_y	0.2	9.1	2.2
M_y	-748.5	-719.5	-780.2
F_z	-5432.9	-5350.6	-5616.0
M_z	-0.0	-2.2	-1.5

Figure 44: Front main bearing forces and moments for the coupled drivetrain at standstill and F_{ext}=0.

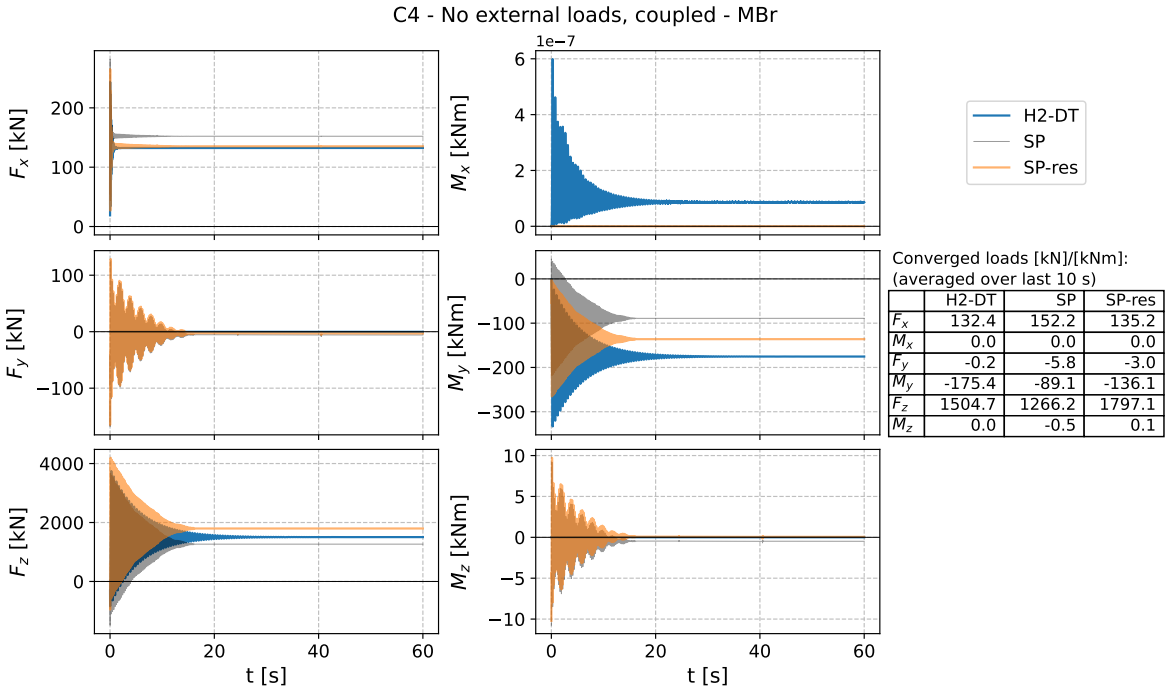

Converged loads [kN]/[kNm]:
(averaged over last 10 s)

	H2-DT	SP	SP-res
F_x	132.4	152.2	135.2
M_x	0.0	0.0	0.0
F_y	-0.2	-5.8	-3.0
M_y	-175.4	-89.1	-136.1
F_z	1504.7	1266.2	1797.1
M_z	0.0	-0.5	0.1

Figure 45: Rear main bearing forces and moments for the coupled drivetrain at standstill and F_{ext}=0.

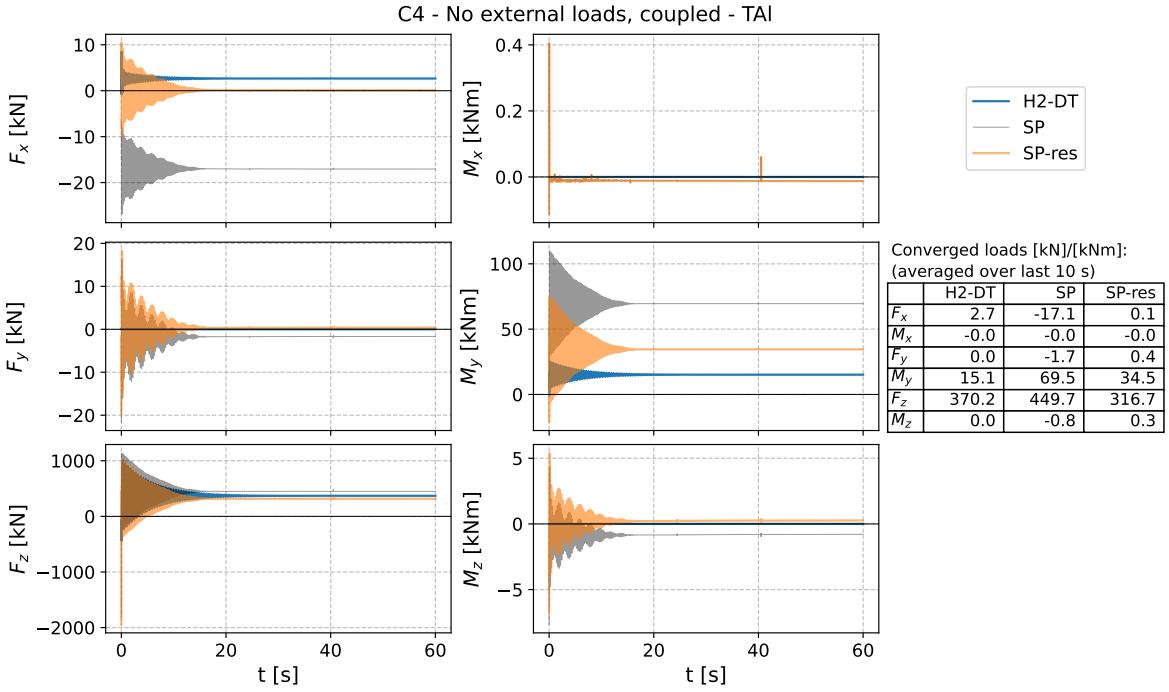

Converged loads [kN]/[kNm]:
(averaged over last 10 s)

	H2-DT	SP	SP-res
F_x	2.7	-17.1	0.1
M_x	-0.0	-0.0	-0.0
F_y	0.0	-1.7	0.4
M_y	15.1	69.5	34.5
F_z	370.2	449.7	316.7
M_z	0.0	-0.8	0.3

Figure 46: Left torque arm forces and moments for the coupled drivetrain at standstill and F_{ext}=0.

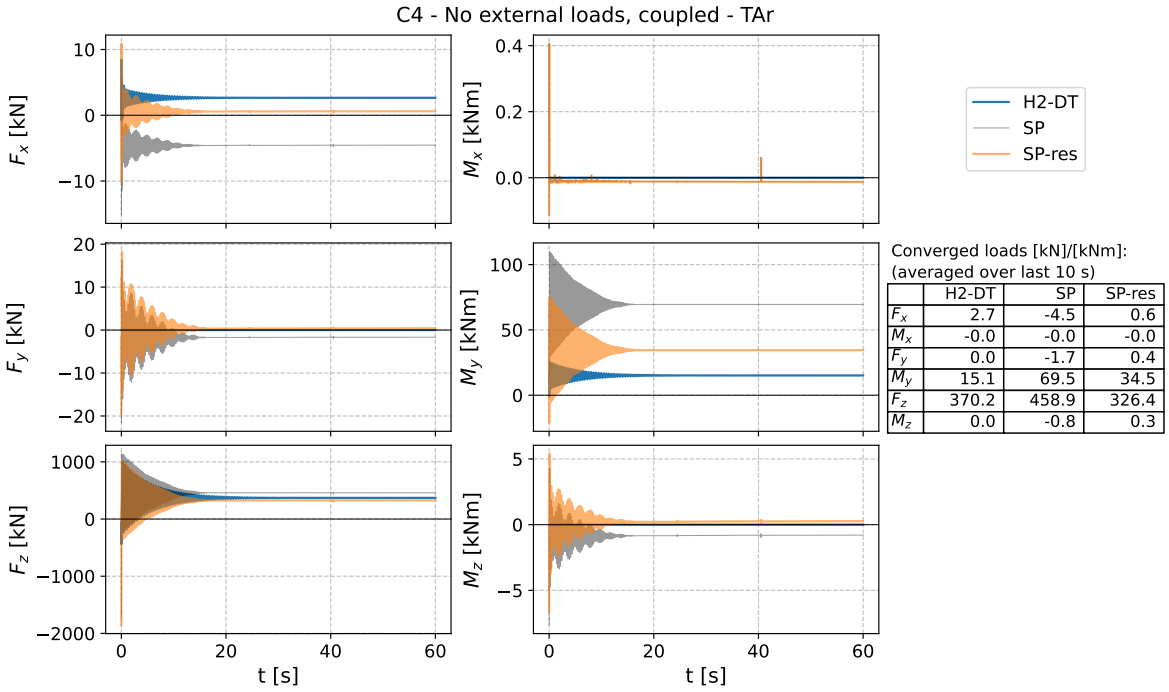

	H2-DT	SP	SP-res
F_x	2.7	-4.5	0.6
M_x	-0.0	-0.0	-0.0
F_y	0.0	-1.7	0.4
M_y	15.1	69.5	34.5
F_z	370.2	458.9	326.4
M_z	0.0	-0.8	0.3

Figure 47: Right torque arm forces and moments for the coupled drivetrain at standstill and F_{ext}=0.

C5 - Comparison of response for coupled system under static loads

Simulation cases C5a and C5b were introduced to examine how the quality of the results is influenced by the magnitude of the applied static loading conditions. After applying two force combinations in x- and y-directions, a similar degree of agreement in the responses could be observed, as depicted in Figure 48 for the front and in Figure 49 for the rear bearing. This indicates that the quality of the results is to a great extent independent of the external loads. The responses for the torque arms show the same characteristics and can be found in section 6. Since only additional forces in the horizontal directions are applied, the F_z-components, and the related moment M_y remain unchanged for cases C5a, C5b, and also the previous case C4. This indicates that the implemented support structures behave as intended.

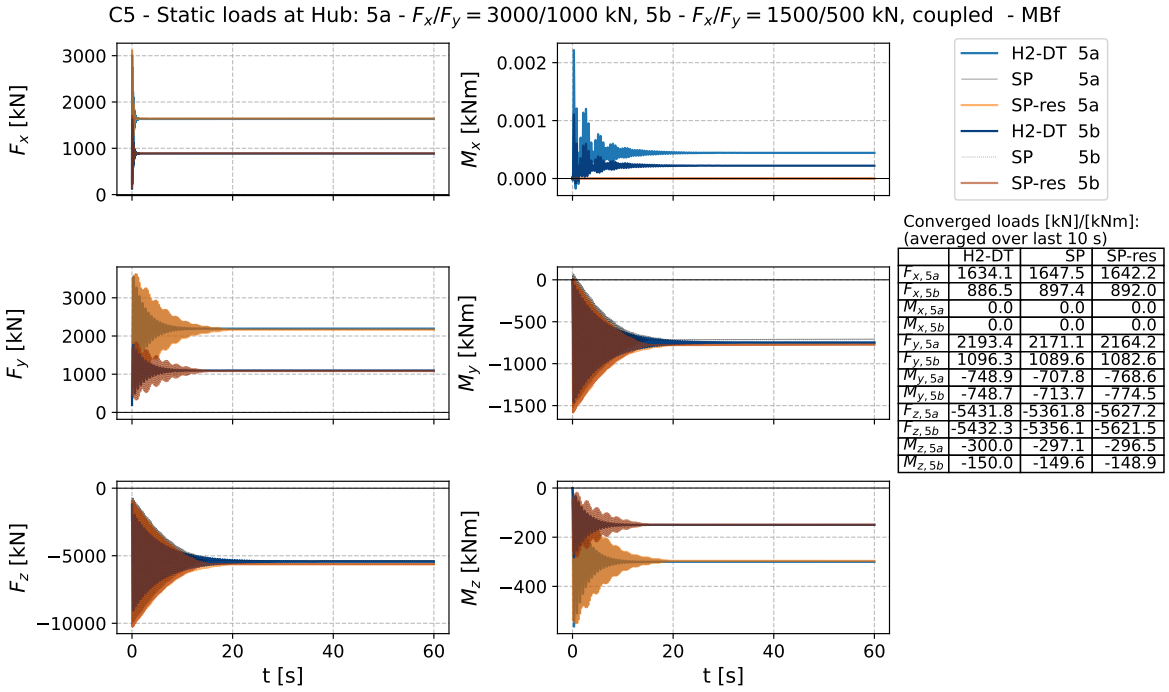

	H2-DT	SP	SP-res
$F_{x,5a}$	1634.1	1647.5	1642.2
$F_{x,5b}$	886.5	897.4	892.0
$M_{x,5a}$	0.0	0.0	0.0
$M_{x,5b}$	0.0	0.0	0.0
$F_{y,5a}$	2193.4	2171.1	2164.2
$F_{y,5b}$	1096.3	1089.6	1082.6
$M_{y,5a}$	-748.9	-707.8	-768.6
$M_{y,5b}$	-748.7	-713.7	-774.5
$F_{z,5a}$	-5431.8	-5361.8	-5627.2
$F_{z,5b}$	-5432.3	-5356.1	-5621.5
$M_{z,5a}$	-300.0	-297.1	-296.5
$M_{z,5b}$	-150.0	-149.6	-148.9

Figure 48: Front MB forces and moments for the coupled drivetrain and different static external loads.

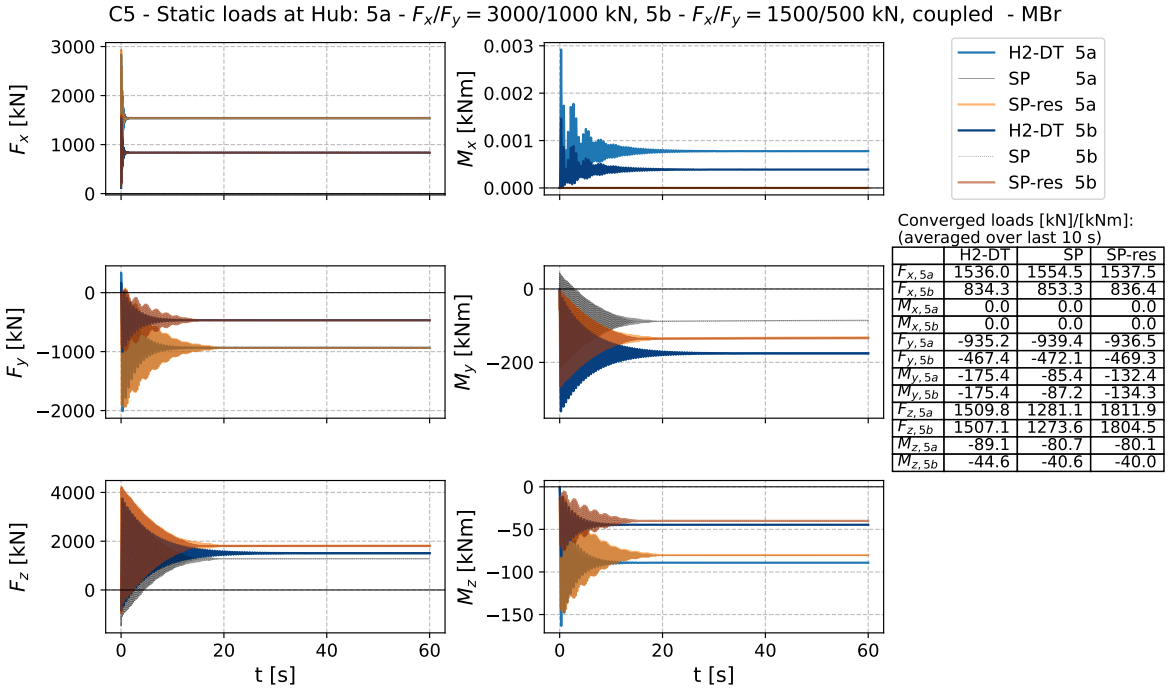

	H2-DT	SP	SP-res
$F_{x,5a}$	1536.0	1554.5	1537.5
$F_{x,5b}$	834.3	853.3	836.4
$M_{x,5a}$	0.0	0.0	0.0
$M_{x,5b}$	0.0	0.0	0.0
$F_{y,5a}$	-935.2	-939.4	-936.5
$F_{y,5b}$	-467.4	-472.1	-469.3
$M_{y,5a}$	-175.4	-85.4	-132.4
$M_{y,5b}$	-175.4	-87.2	-134.3
$F_{z,5a}$	1509.8	1281.1	1811.9
$F_{z,5b}$	1507.1	1273.6	1804.5
$M_{z,5a}$	-89.1	-80.7	-80.1
$M_{z,5b}$	-44.6	-40.6	-40.0

Figure 49: Rear MB forces and moments for the coupled drivetrain and different external loads.

C6 - Comparison of response for coupled system under steady inflow conditions

Due to the reduced fidelity of the torque arm support structures, in the following, the model comparison is focused on the response of the main bearings only. To analyze the behavior of the H2-DT model under steady wind conditions, simulations were run for three different wind speeds: one below (7 m/s), one at (11 m/s), and one above the rated wind speed (15 m/s). For this comparison, the flexibility of the tower and the blades was activated in the HAWC2 model. When comparing the results for the three given load cases, it was observed that for the increasing rotational frequency of the drivetrain, resulting from the higher wind speeds (see V_0-ω-curve in Figure 37), growing oscillations in the SIMPACK response were occurring, even for rigid blades and a rigid tower. This phenomenon is illustrated in Figure 50.

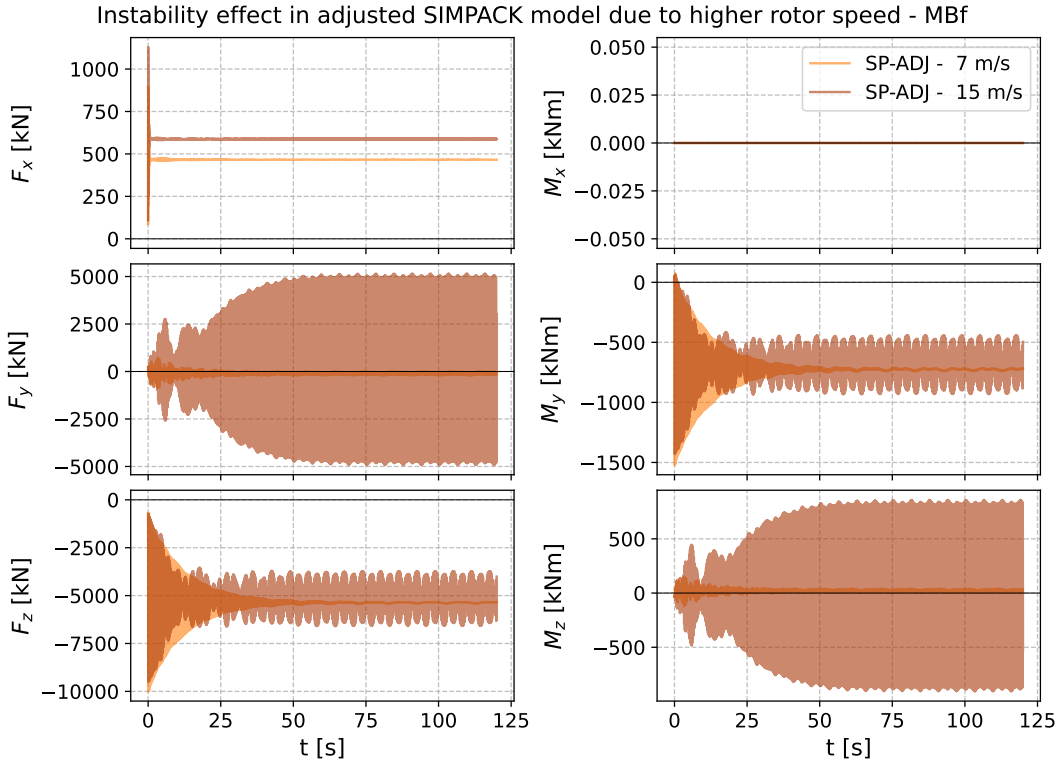

Figure 50: Visualization of instability effect in adjusted SIMPACK model due to an increase in rotor speed.

While simulations with higher sampling frequencies did not have any effect on the results, an increase in the damping of the affected connectors did. Although there was a strong reason to suspect that these instabilities resulted from the internal residual stresses, combined with the natural frequencies and too low damping of the support structures, the exact source of the problem remained unknown. Therefore, the choice was made to run all steady wind flow simulations without rotation to avoid the negative impact of these instability effects while maintaining low residual forces. Since, under steady external loading conditions, the converged reaction forces and moments in the support structures of interest should be independent of the rotational speed, this approach was considered a suitable compromise for comparing the responses of both models without requiring additional, major modifications to the SIMPACK model.
To guarantee that for the HAWC2 and the SIMPACK model, the hub center, and hence the subsequent turbine structure, was subjected to identical loads, the following guideline was developed and applied to all steady wind simulations individually:

1. Run the simulation in HAWC2 for 150 s to determine the converged external hub loads, corresponding to the integrated aerodynamic rotor loads. The integrated rotor loads can be obtained using the HAWC2 commands `aero int_rotor_force-` and `aero int_rotor_moment` [34].

2. Use the last 90 s as input for the SIMPACK model.

3. Compare the responses of both models, including and excluding the residuals derived in Case 3.

Since the aerodynamically induced loads on the tower and nacelle do not directly contribute to the loads acting on the driveshaft, they were disregarded in the analysis. In Figure 51, the process of deriving the input for the SIMPACK simulations for a steady wind of V_0 = 7 m/s is shown. The grey area illustrates the transient period, which is disregarded after the HAWC2 simulation.

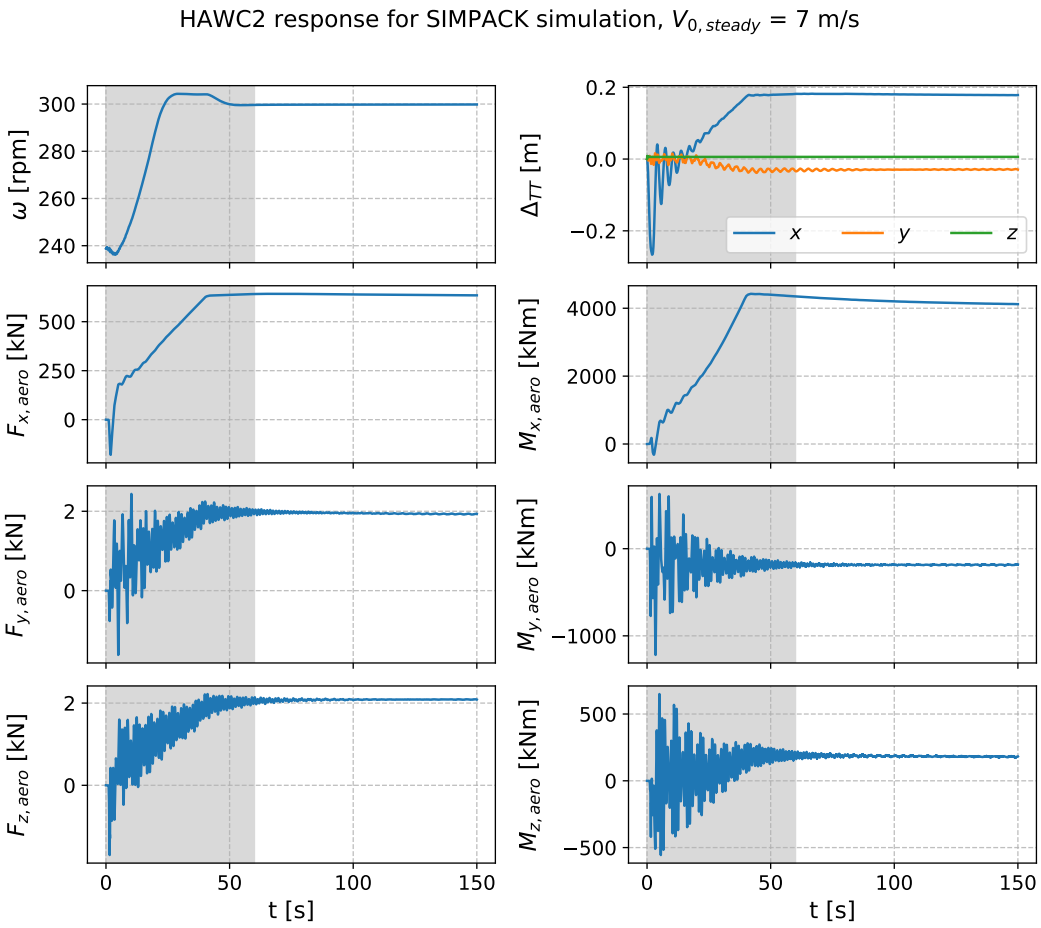

Figure 51: Rotor speed, tower displacement, and resulting aerodynamic rotor loads obtained with HAWC2 for a steady wind simulation of V_0 = 7 m/s.

Figure 52 and Figure 53 show qualitatively the last 10 s of the results from the steady windflow simulations for 7, 11, and 15 m/s using a flexible tower and flexible blades. These plots serve to assess how the main bearing response of the implemented HAWC2 model follows the trend of the SIMPACK sample model. The converged loads are not presented at this point. Instead, a more detailed load assessment across the entire operational wind speed range is presented at the end of section 4.

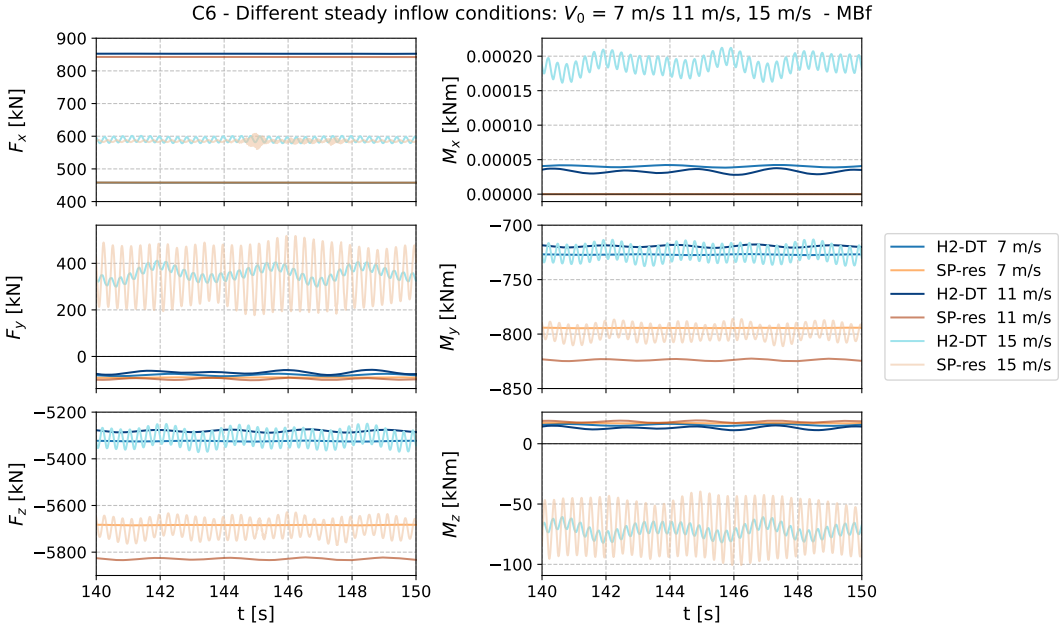

Figure 52: Front MB forces and moments for different steady inflow conditions.

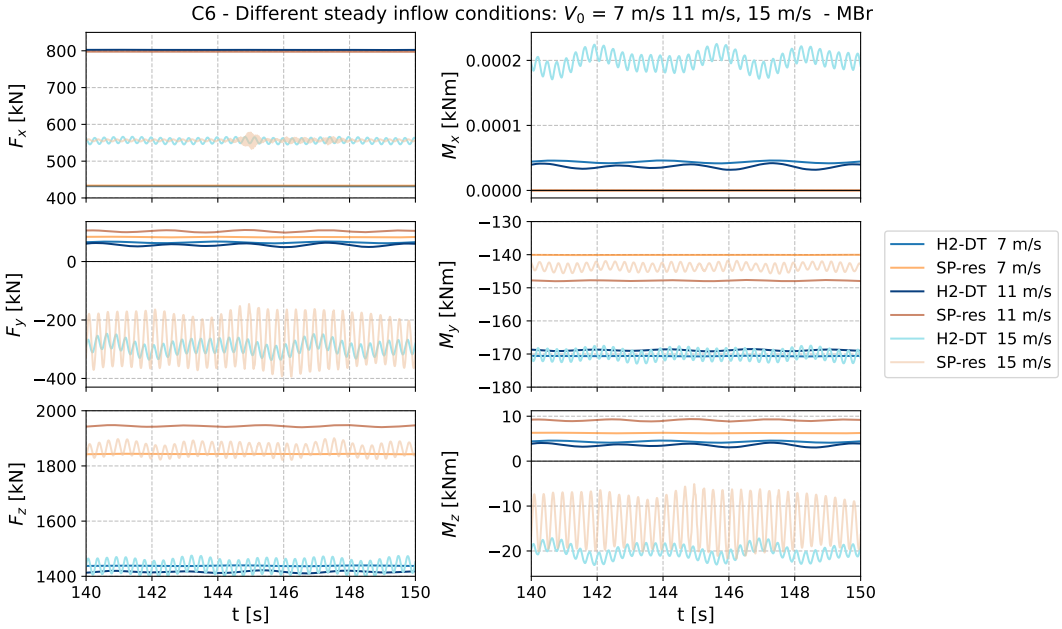

Figure 53: Rear MB forces and moments for different steady inflow conditions.

C7 - Impact investigation of implemented joint features

To close the comparison between the detailed HAWC2 model with the SIMPACK model, the effect of the implemented support structures, as discussed in Step II of section 3, is analyzed. Therefore, one simulation was done, where all implemented support beams were rigid and compared with the results of the structure that contained the derived elastic properties. The comparison is illustrated in Figure 54 and Figure 55 for the main bearings, and in Figure 73 and Figure 74 for the torque arms. The impact of the developed features is clearly visible.

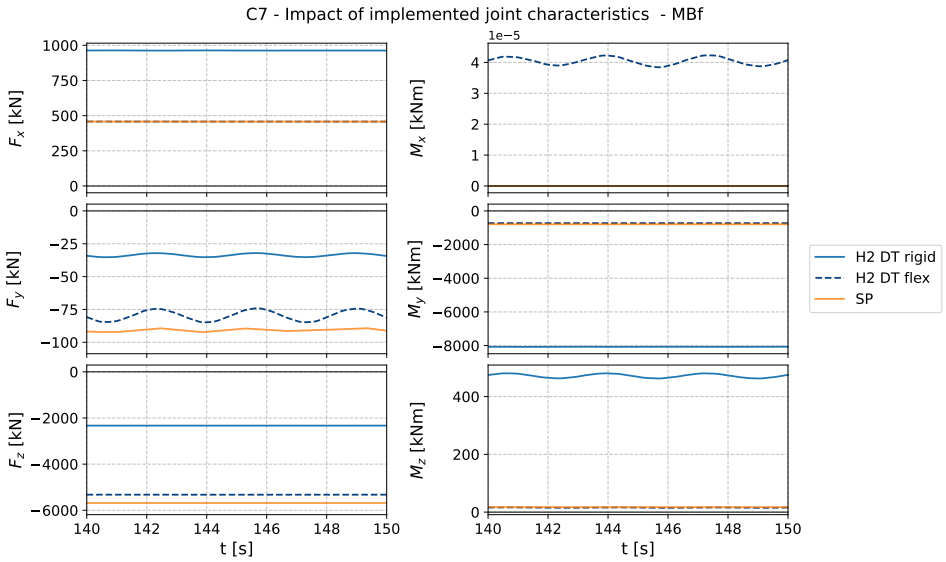

Figure 54: Comparison of rigid and flexible drivetrain structure for front main bearing, a rigid tower, and rigid blades.

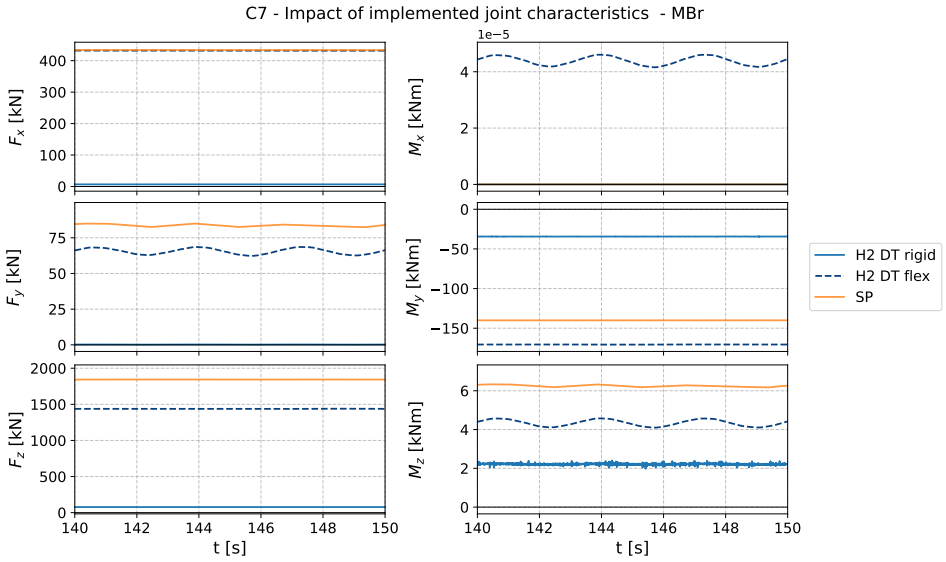

Figure 55: Comparison of rigid and flexible drivetrain structure for rear main bearing, a rigid tower, and rigid blades.

C8 - Turbulent simulation

The last individual simulation case involved comparing the main bearing loads under realistic wind conditions with turbulence. The main characteristics of the applied simulation parameters are summarized in Table 16. As previously shown, the instabilities in the response of the SIMPACK model occurr only for higher rotational speeds. Therefore, to be able to include the rotor speed in this comparison, a mean wind speed of 7 m/s was chosen.
Compared with the steady inflow scenario, for the time-marching turbulent simulation, a slightly different approach is used. Instead of using the converged values, first a 700s simulation is run in HAWC2, where the first 100 s are considered as the transient response. Then, the solution of the first timestep after this 100 s is used as steady input for the first 100 s for the SIMPACK simulation, followed by the remaining 600 s that represent the turbulent inflow scenario. Consequently, only the last 600 s of both simulations are compared.
Figure 56 and Figure 57 illustrate the time-marching reaction loads of both main bearings. While the mean values match fairly well for most of the channels, and hence follow the same trend as observed in the previous

cases, the extreme values show a lower level of agreement. The 10-second zoomed-in sections in Figure 58 and Figure 59 illustrate the mismatch in greater detail. This discrepancy highlights the importance of adequately modeling the natural frequency of the support structures, as outlined in Step III of section 2, as the presented comparison indicates that both the fatigue and extreme loads are affected.

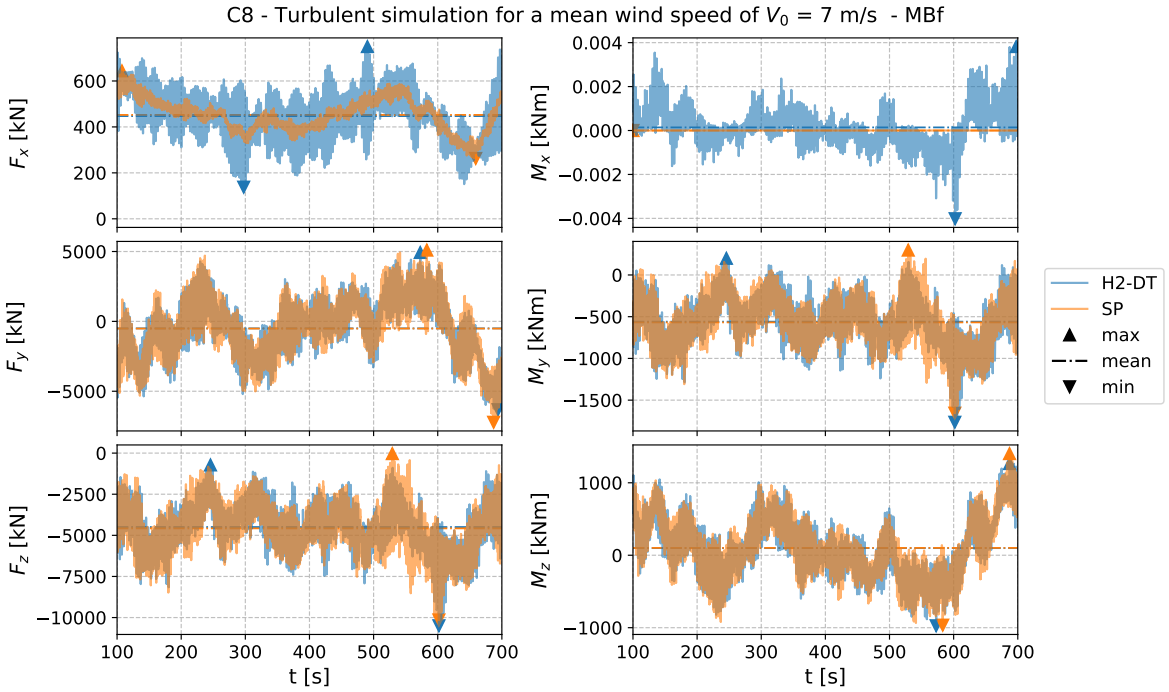

Figure 56: Comparison of front main bearing loads under turbulent conditions.

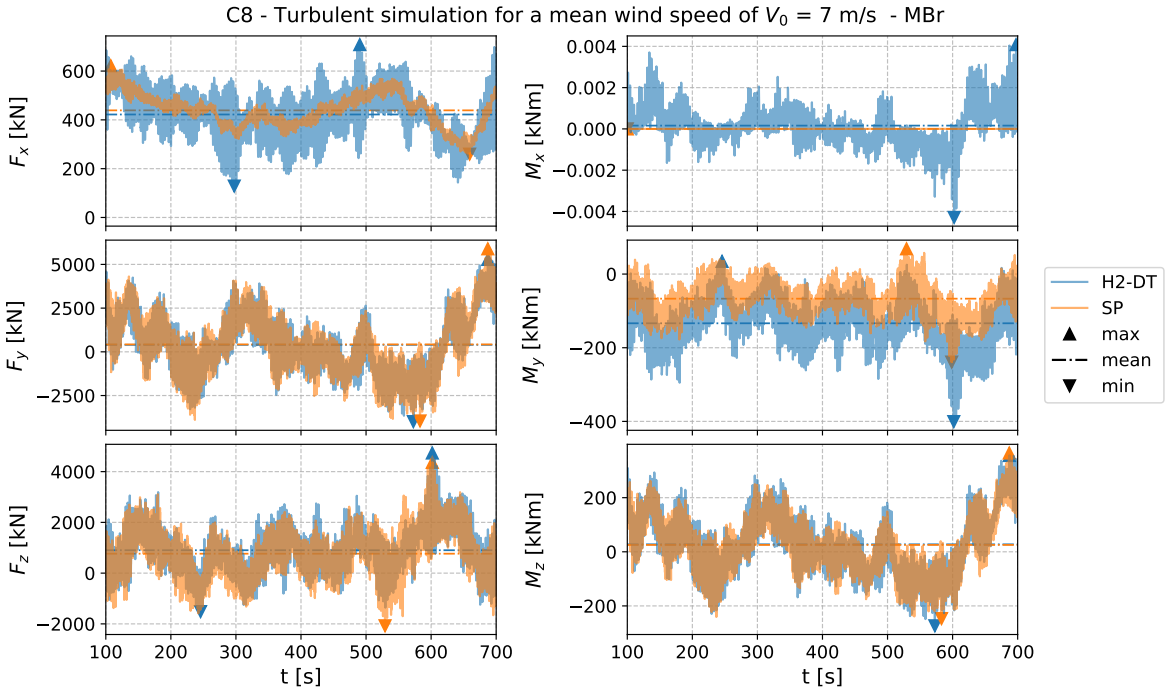

Figure 57: Comparison of rear main bearing loads under turbulent conditions.

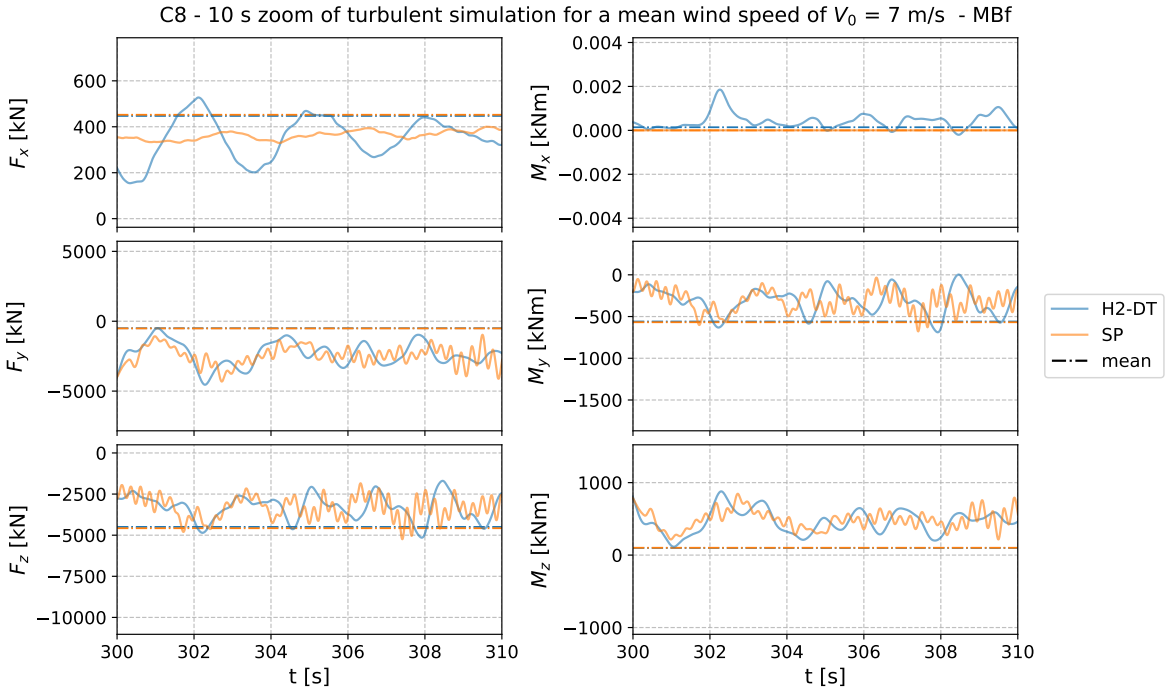

Figure 58: Zoomed-in section of front main bearing loads under turbulent conditions.

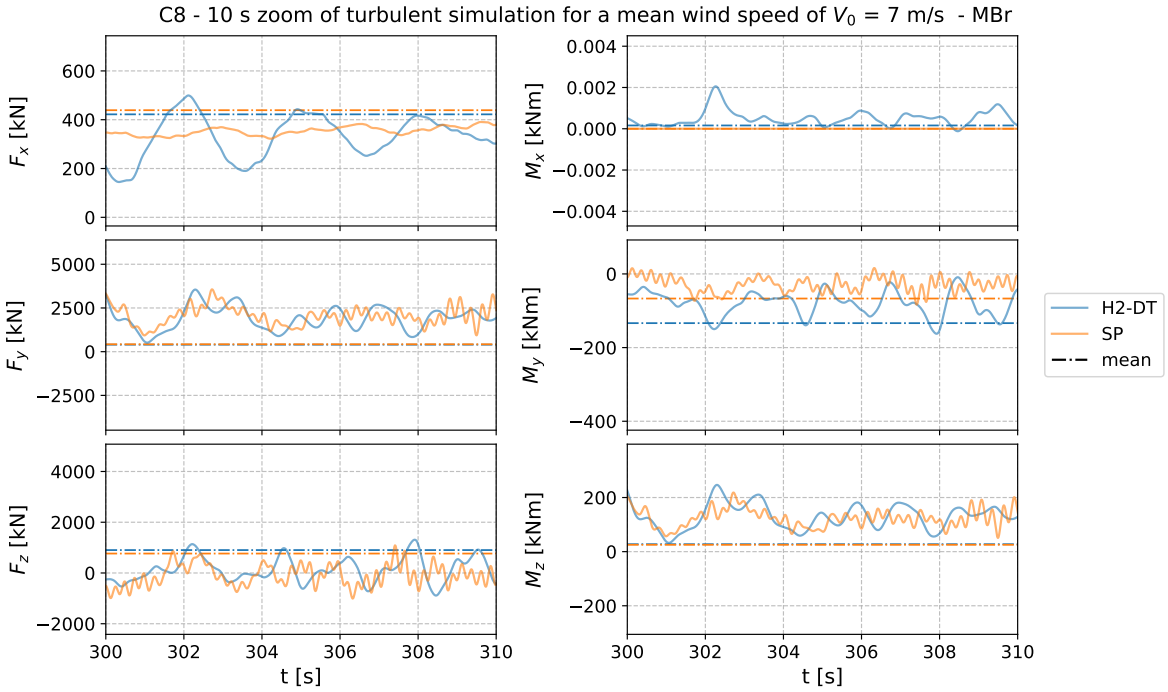

Figure 59: Zoomed-in section of rear main bearing loads under turbulent conditions.

4.3. Model comparison

Finally, a load assessment was made across the entire operational range of the DTU 10MW RWT, i.e. from V_0 = 5 to 25 m/s with increments of 2 m/s. More precisely, for each of these wind speeds, a simulation was carried out using a steady inflow, a flexible tower, and flexible blades. The same method as described for Case 6 was applied, and the mean values of the last 10 s of each load channel were calculated and considered

as the converged solution. To investigate the impact that the implementation of the enhanced drivetrain model has on the overall turbine response compared to the simple configuration, the adjusted HAWC2 model was included in this analysis. Figure 60 shows the integrated aerodynamic rotor loads with respect to the corresponding wind speed. Hence, the designated points in these curves represent the externally applied loads at the hub center in all three models. To identify the sources of the large aerodynamically induced moments My, and M_z, additional simulations were performed: (a) with a rigid tower and rigid blades (red line), and (b) with an additional 5° inflow angle to account for the tilted drivetrain (purple line).

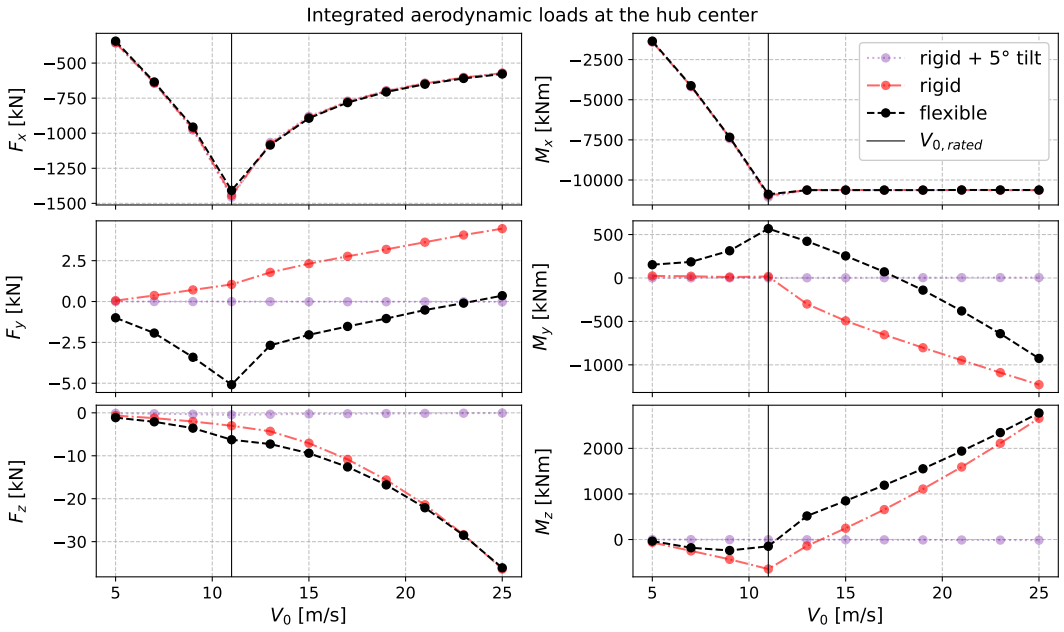

Figure 60: Resulting loads at hub center due to steady inflow conditions for different wind speeds.

This concluding analysis was used to evaluate the agreement among the three models in terms of the main bearing reaction forces and the resulting loads at the last tower node, i.e., at the yaw bearing position. To assess the plausibility of the results on the one hand, and to evaluate the extent to which the enhanced drivetrain model potentially influences the global turbine response, the yaw bearing loads are presented first. As illustrated in Figure 61 and Figure 62, the comparison is done both in absolute and in relative terms. Latter aims to quantify the load deviation $L\Delta\%$ of the HAWC2 models, compared to the SIMPACK configuration. To avoid amplifying regions with low absolute values, the local difference for each load channel $L_{H2}(V_0) - L_{SP}(V_0)$ was normalized, using the mean across the entire range of the SIMPACK response $\overline{L_{SP}}$ (see Equation 16 and Equation 17). This method enables visualizing the trend of the relative difference across the turbine operating range within a certain load channel. However, since $L\Delta\%$ is sensitive to the magnitude of the individual loads and the mean value of the corresponding channel, it does not allow for accurately cross-comparing the quality of the different load channels.

$$L\Delta\%(V_0) = \frac{L_{H2}(V_0) - L_{SP}(V_0)}{\overline{L_{SP}}} \cdot 100 \tag{16}$$

$$\overline{L_{SP}} = \sum_{V_0} \frac{L_{SP}(V_0)}{11} \quad V_0 = 5, 7, 9, .., 25\text{m/s} \tag{17}$$

Since the yaw bearing connects the tower to the rotating nacelle, it is oriented horizontally. Accordingly, a non-tilted coordinate system is used for the analysis of the associated loads. As a consequence, the coordinate systems used for presenting the hub and the yaw bearing loads differ slightly, being rotated by 5° around the y-axis. This misalignment introduces small shifts in the x- and z-load components. However, for this analysis, the effect is considered negligible, since $\cos 5° \approx 1$ and $\sin 5° \approx 0$.
When looking at the two figures below, it can be observed that, in general, all three models reasonably follow the same trend, especially for the dominating load components. All relative deviations, apart from the

F_y-component, lie within approximately 7 %, indicating that the application of external loads was done appropriately on the one hand, and on the other hand, that all three models transfer these loads to the tower top in a comparable manner. As expected, $F_{x,Yaw}$ corresponds almost exclusively to the negative thrust force at the hub, i.e., the $F_{x,Hub}$-component in Figure 60. The same applies for$M_{x,Yaw}$, being the reaction moment of the aerodynamic rotor torque $M_{x,Hub}$.
$F_{y,Yaw}$ is also directly related to $F_{y,Hub}$, and therefore purely aerodynamically caused. From Figure 60, it can be seen that the small lateral aerodynamic force is primarily caused by the flexibility of the tower and blades, as well as the tilt angle of the rotor. The z-force component of the yaw bearing is a result of the combined mass of rotor and drivetrain, superimposed with small aerodynamic forces (see $F_{z,Hub}$) and additional minor contributions from $F_{x,Hub}$ due to the deviating coordinate definition. The relative difference of F_z in Figure 62 is roughly in accordance with the calculated mass deviations of 0.3 %, presented in Table 13. The moment $M_{y,Yaw}$ is composed again of the aerodynamic counterpart, but additionally has contributions from the moments created by both perpendicular force components $F_{x,Hub}$ and $F_{z,Hub}$ and their spatial offset to the location of the yaw bearing (see Figure 34 where the yaw bearing location coincides with the node connecting the tower with the tower top). $M_{z,Yaw}$ is again aerodynamically induced and originates primarily from the tilt angle.
In general, it can be stated that the largest deviations, in both absolute and relative terms, occur close to the rated speed where the blade deflections are reaching their maximum. Figure 77 in Appendix A presents the tip deflections at the azimuthal position of the tower, where δ is the difference in tower clearance between the rigid (TC_{rigid}) and the inflow-dependent flexible blade scenario ($TC_{flex}(V_0)$). As previously mentioned, these deflections move the center of gravity of the rotor, which is not accounted for in the SIMPACK model.

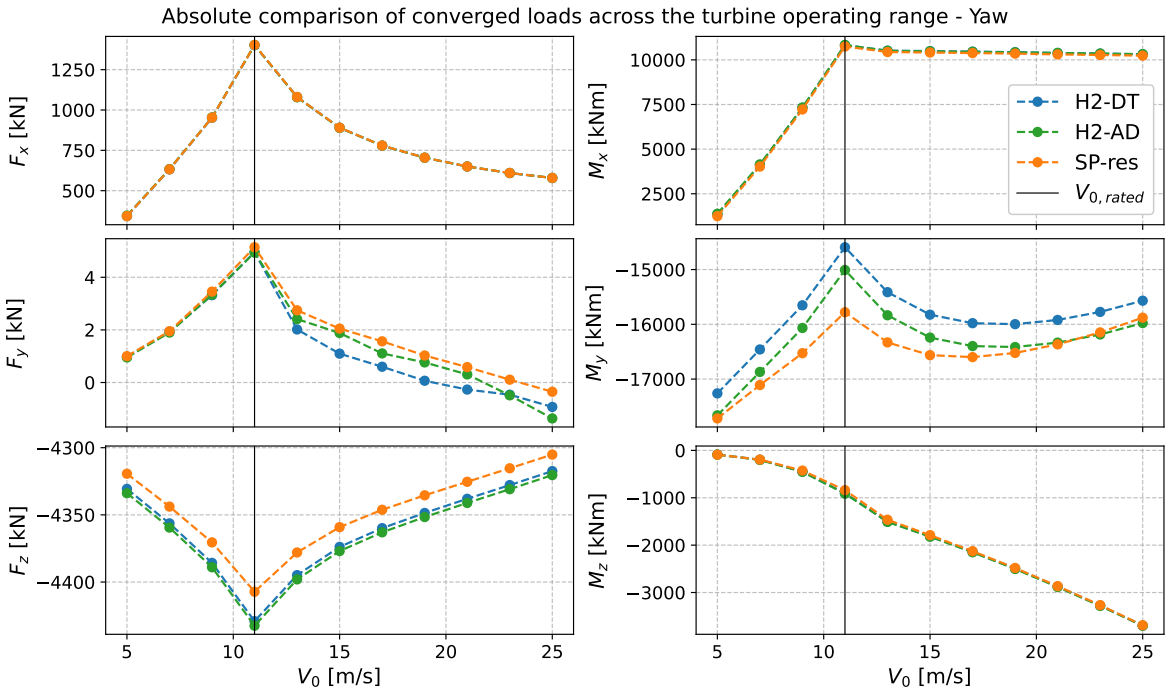

Figure 61: Absolute comparison of yaw bearing loads.

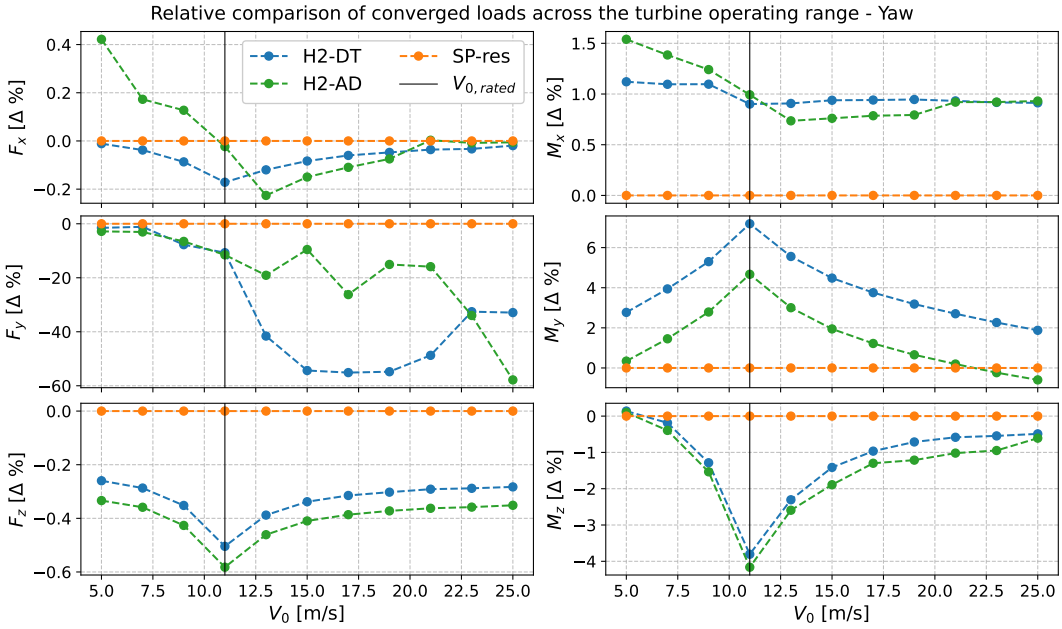

Figure 62: Relative comparison of yaw bearing loads.

Since the simplified HAWC2 representation, H2-AD, does not include main bearings, two nodes were introduced into the shaft body at their respective positions. These nodes were then used to compute the internal loads. As expected, however, the resulting forces and moments do not correspond to the main bearing loads of the SIMPACK model.

Since the simple HAWC2 representation, H2-AD, does not include the main bearings, two nodes were introduced at the shaft body at their respective positions. These nodes were then used for the computation of the internal loads. As expected, however, the resulting forces and moments do not map the SIMPACK model's main bearing loads accurately. In Figure 75 and Figure 76 in Appendix A, the load comparison for the main bearings of all three models is shown, while the four figures below focus on comparing the absolute and relative outcomes of the SIMPACK model and the detailed HAWC2 model.
Similar to the values of the yaw bearing, the best agreement between the two models for both main bearings can be found in the load channels F_x, F_y, M_x, and M_z. M_x corresponds to the free degree of freedom, yet the small, negligible residual loads in the H2-DT response are due to the limitations discussed in the Implementation Step III. Larger discrepancies are present in the rear bearing, as already noticed in previous load cases, and varying relative deviations around the rated wind speed can again be explained by the flexible CG of the rotor, being disregarded in the SIMPACK simulations.

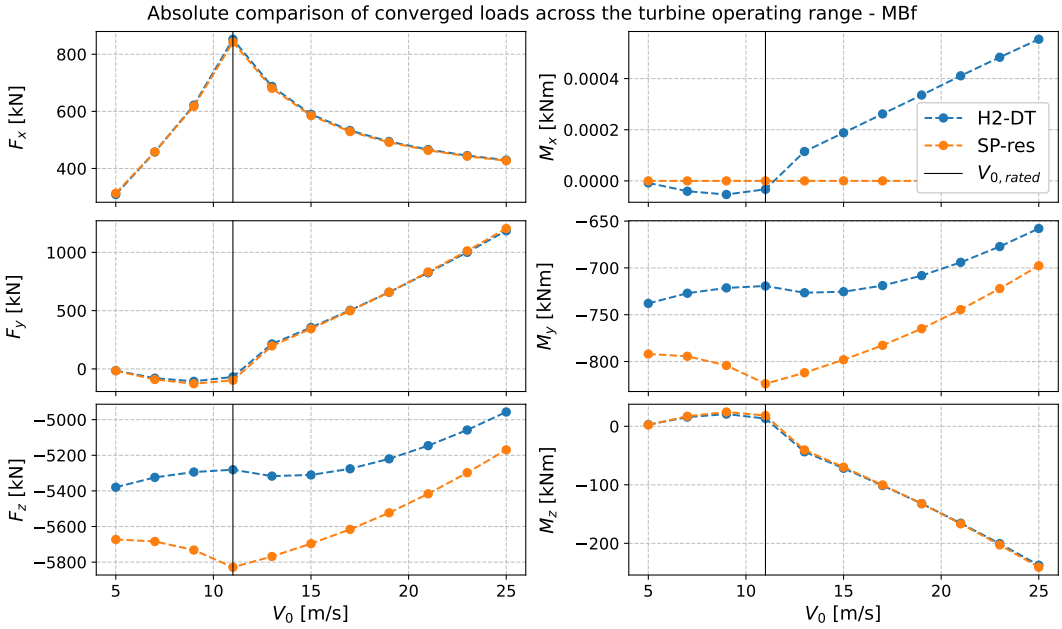

Figure 63: Absolute comparison of MBf loads across turbine operating range.

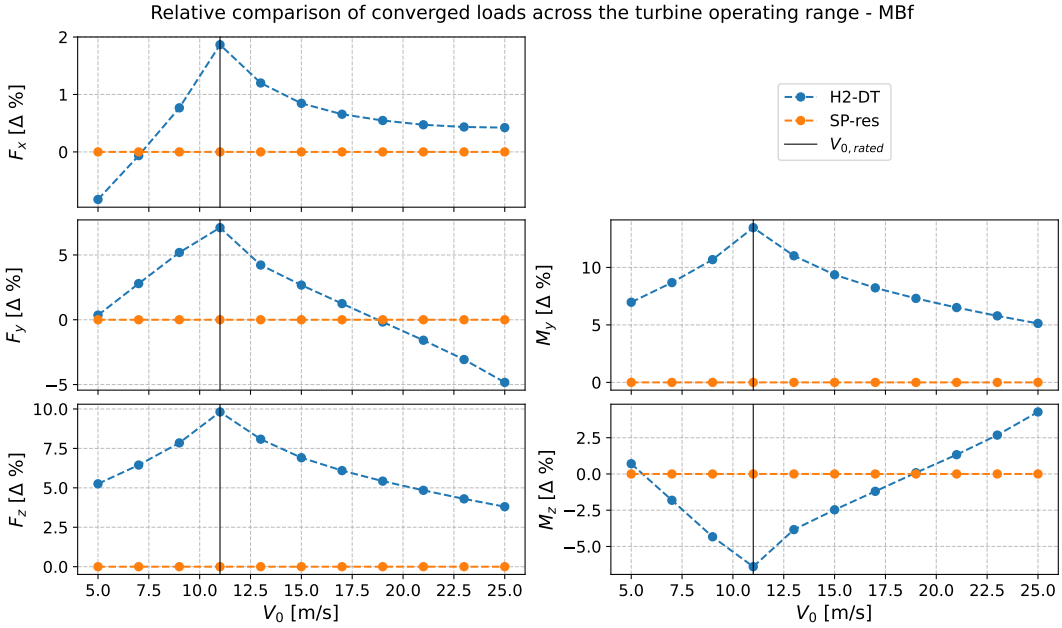

Figure 64: Relative comparison of MBf loads across turbine operating range.

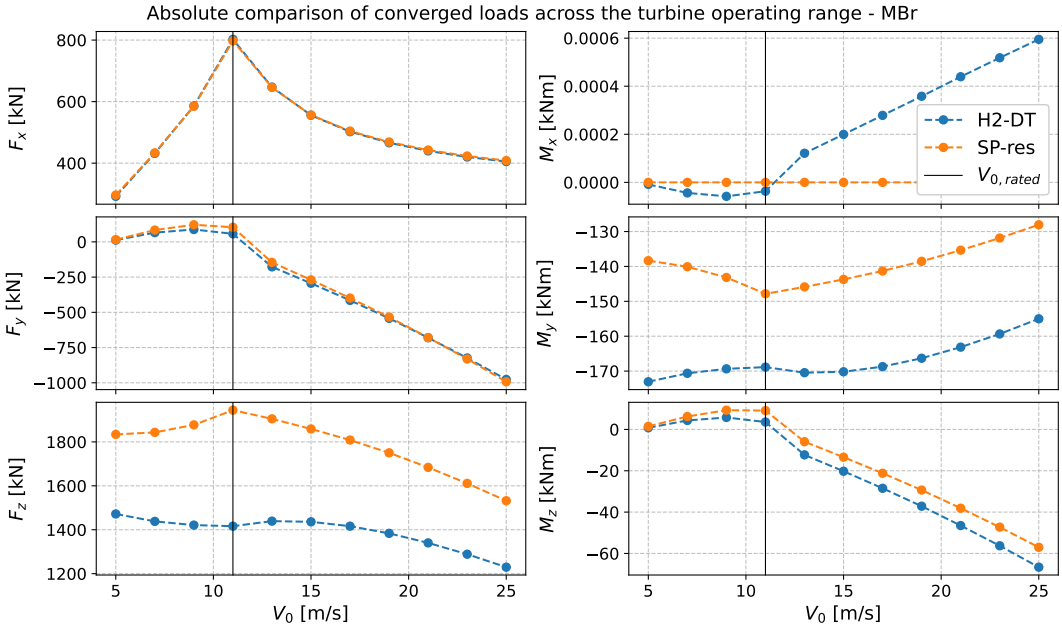

Figure 65: Absolute comparison of MBr loads across turbine operating range.

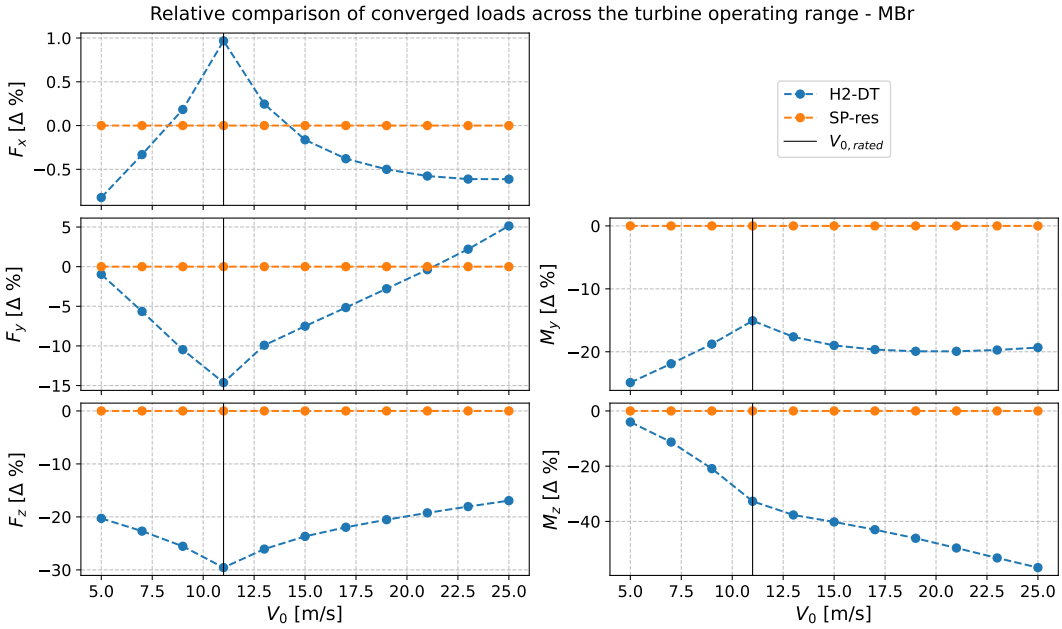

Figure 66: Relative comparison of MBr loads across turbine operating range.

Although the differences, especially in the converged loads, are small, the results are an indication that the implementation of a detailed drivetrain has an impact on turbine response. Naturally, in order to draw profound conclusions, extensive analyses would be necessary and were not carried out within the scope of this project.

5. Discussion

To evaluate the presented work, the overall quality of the developed drivetrain model is assessed, including its ability to reproduce key dynamic behaviors and its consistency with the reference SIMPACK model. While the main limitations of the five implementation steps have already been discussed, the most relevant model restrictions are summarized in this section, and potential improvements and suggestions for future research are outlined.

5.1. Model evaluation and limitations

All in all, the results demonstrate that it is feasible to incorporate additional drivetrain complexity into the HAWC2 model using simple Timoshenko beam representations. The approaches used improve the fidelity of the overall wind turbine model, particularly for the main bearings, where good agreement with the reference model was observed.
For the decoupled system, the isolated main bearing and torque arm structures capture the dynamic characteristics of the high-fidelity SIMPACK model effectively, supporting the validity of the chosen implementation method. However, when considering the coupled system, the agreement is reduced due to the complex internal dynamics of the driveshaft, and especially the gearbox. In general, the enhanced drivetrain model provides accurate results of the main bearing response for steady simulations and results with limited fidelity for turbulent simulations.
When examining the responses of the main bearings and the yaw bearing across the wind turbine's steady operating range, the HAWC2 model largely follows the trends observed in the SIMPACK model. However, the agreement could likely be improved if the rotor mass center in the SIMPACK model were represented as a function of the blade deflections. Differences in the response at the yaw bearing compared to the simple HAWC2 model were observed, but these results must be interpreted with caution due to the limited number of tests conducted. Compared to the original simple model, the detailed representation significantly increases the information obtained and offers a foundation for further fidelity improvements by incorporating additional features.

It must be noted that the implemented HAWC2 drivetrain model still relies on a number of simplifications and assumptions. When transforming a three-dimensional drivetrain representation, such as the SIMPACK model, into a one-dimensional beam-based structure, part of the geometric and stiffness-related information is inevitably lost. This reduction becomes particularly problematic for components that are not rotationally symmetric, as their anisotropic stiffness and mass distributions cannot be adequately represented by simplified beam elements. Moreover, the applied modeling approach is unable to capture the complex behavior of the gearbox, including its multiple stages, internal inertias, and the combination of flexible and rigid parts, which further limits the accuracy of the drivetrain representation. For instance, in SIMPACK, similar to a real gearbox, only the shafts of the first and last stages are directly connected to the neighboring drivetrain components. All other gearbox parts are supported internally by bearings and, ultimately, by the gearbox housing. In contrast, in the HAWC2 model, the simplified gearbox representation causes the mainshaft to connect directly to the entire gearbox body and consequently its full weight.
Other major limitations arise from the given set of predefined HAWC2 connection constraints between beams. In particular, the inability to directly assign stiffness values to constraints necessitated the use of additional support beams. While an adequate implementation of these auxiliary elements allows the flexibility properties of the reference constraints to be included, some unintended side effects remain. As observed in Phase III, the implemented support structures exhibited different response frequencies compared to their SIMPACK counterparts. To improve the model's accuracy, particularly to enable a reliable determination of damage equivalent and fatigue loads, a method for matching these frequencies has to be found.
Modeling the drivetrain remains a complex task, and the reliability of any HAWC2 implementation strongly depends on the available data from the SIMPACK reference model. While the SIMPACK model provided a valuable guideline, a deeper understanding of its structure, assumptions, and limitations would have been beneficial and could have facilitated the model comparison. In this context, special attention must be paid to the residual loads present in the SIMPACK drivetrain model. For a more accurate verification of the implemented HAWC2 drivetrain structure, a detailed analysis of these pre-stresses and the effects of driveshaft rotation on them is required.
Another limitation involves the fact that non-rotating components, such as the gearbox housing, stator, generator housing, and nacelle housing, are represented in the model. As a result, their associated masses are

not included. Furthermore, neglecting the flexibility of the mainframe introduced an additional simplification that reduces the fidelity of the model.
Regarding computational expense, experiments indicate that the detailed model requires approximately twice the simulation time of the simpler configuration, which may limit its applicability in scenarios with constrained computational capacities. Finally, although each implementation step was performed carefully, errors, incorrect assumptions, or inaccuracies cannot be entirely ruled out, particularly given the inherent complexity of wind turbine drivetrain dynamics.

5.2. Future work

Building on these findings and limitations, several approaches for potential model improvements and future work were identified. Direct and relatively straightforward improvements include correcting the 0.4 m offset of the connection point between the main shaft and the gearbox to match the SIMPACK reference model. Furthermore, certain characteristics identified during the development process could be incorporated to obtain more accurate estimates of the main bearing loads. These include fine-tuning the exact location of the gearbox center of gravity and integrating a coupling beam element with the exact stiffness terms to connect the main shaft and the gearbox, similarly to the approach used for the generator–gearbox coupling. Additionally, implementing the precise torsional stiffness for the generator–gearbox coupling could further improve the agreement with the SIMPACK model.
More challenging enhancements that could increase the fidelity of the HAWC2 drivetrain representation include incorporating mainframe flexibility to capture additional structural dynamics and developing a more detailed model of the gearbox. However, enhancing the complexity often leads to longer calculation times, necessitating a careful trade-off between model accuracy and computational efficiency.
Apart from the model adjustments, further analysis using the developed model would be beneficial. However, as discussed above, this requires a deeper understanding of the SIMPACK reference model, determining the exact origin of the detected residuals, and flexible adjustments of the rotor CG, depending on the blade deformations. Subsequently, conducting additional simulations and performing a more detailed analysis of the results could reveal valuable insights regarding both the capabilities and limitations of the developed model. Moreover, using an existing drivetrain as a reference for the applied implementation methods and comparing the outcomes with real measurement data would provide a great opportunity to test the accuracy of the developed concepts. At the same time, the methods used should be critically evaluated, and entirely different modeling approaches should also be considered.

Potential research questions that build on the findings of this project could be:

- How does the integration of the more realistic drivetrain structure in HAWC2 affect the dynamic response of the entire turbine for different design load cases, and how does it contribute to improving the fidelity of HAWC2 simulations?
- Does the inclusion of additional flexible drivetrain components have an impact on the natural frequencies of the turbine tower or the blades?
- To what extent can a more accurate wind turbine model in HAWC2 help to bridge the gap between overall system-response calculations and specific high-fidelity tools used to design and analyze individual components, by facilitating the transfer of simulation results?

6. Conclusion

The main objective of this thesis was the development of an enhanced drivetrain model in HAWC2 to enable the analysis of drivetrain loads, with a particular focus on main bearing loads. Furthermore, the goal was to improve the capability to capture dynamic coupling effects in modern wind turbines using HAWC2. For this purpose, the study was guided by a set of research questions that helped to structure the four major project phases: the Initialisation and Research phase, the Model Preparation phase, the Model Implementation Phase, and the Model Verification phase.

In the first phase, a detailed literature study was conducted to analyze the prevailing trends, essential components, and key characteristics of modern wind turbine drivetrains, as well as to identify existing modeling approaches. The core findings included the importance of holistic modeling strategies, the growing necessity to account for flexibility effects in drivetrain calculations, and the increasingly complex demands of large, modern wind turbines.

Second, in the Model Preparation phase, the DTU 10 MW RWT and the corresponding SIMPACK drivetrain model were identified as reference models for the project, fulfilling the previously defined requirements regarding availability and suitability. Subsequently, the underlying theoretical concepts and the associated software environments were studied.

The implementation phase was subdivided into five steps. Each of these contributed to accurately reproducing the dynamic behavior of the drivetrain while striving for consistency with the reference model. In the Model Structure Derivation step, an initial drivetrain beam model was derived in HAWC2, representing the main components and support structures of the guideline model. This was followed by the next step, the Cross-Platform Model Translation, in which effective methods were established to transfer the geometric specifications and material properties of the SIMPACK drivetrain to the corresponding HAWC2 beam elements. Depending on the available data of the component, the required parameters were either directly implemented or obtained using a cross-sectional analysis.
The third step involved the structural tuning of the essential drivetrain support structures, the main bearings, the torque arms, and the gearbox-generator coupling. An approach was found to assign the joint stiffness terms from the SIMPACK model to newly introduced three-beam models, using the longitudinal and torsional stiffness properties of Timoshenko beam elements. The related damping properties were then iteratively tuned to obtain similar characteristics.
In implementation step IV, adjustments were made to the simplified HAWC2 drivetrain to enable comparison with the new model. By assigning the mass and inertia properties of the individual components to their respective location in the simple model, good levels of agreement between the models were obtained. Finally, the stiffness of the gearbox beam in the detailed drivetrain model was adapted to ensure consistency with the first torsional eigenfrequency of the reference models.

The developed enhanced HAWC2 model demonstrated high accuracy in capturing main bearing loads under steady conditions and provided reasonable estimates in turbulent simulations. The torque arm response showed reduced agreement, mainly due to the simplified representation of the gearbox. Despite these limitations, the model successfully enhanced the fidelity of the drivetrain response compared to the original HAWC2 setup. It further revealed differences in the yaw bearing response compared to the simplified configuration, suggesting that the detailed drivetrain structure influences the overall turbine behavior.
The main challenges encountered in this project were the identification of a suitable division of the complex SIMPACK drivetrain model, the transfer of three-dimensional component characteristics into a one-dimensional beam representation, and the integration of the dynamic properties of key support structures such as the main bearings and torque arms. While potential approaches to address these challenges were explored, further work is required to refine the model. Nevertheless, the outcomes of this project provide a solid baseline for future research, offering both technical challenges and valuable opportunities for deeper insight into the understanding of coupling effects in wind turbine dynamics.

References

[1] Peter Yang. Renewable Energy: Challenges and Solutions. Springer Nature, 2024.

[2] International Renewable Energy Agency. IRENA. www.irena.org/. Accessed: 2024-11-22. 2024.

[3] Tony Burton et al. Wind Energy Handbook (3rd Edition). John Wiley Sons, 2021.

[4] Nejad Armir R. et al. "Wind turbine drivetrains: state-of-the-art technologies and future development trends". In: Wind Energy Science Journal (2022).

[5] Patrick J. Moriarty et al. "Wind Turbine Modeling Overview for Control Engineers". In: 2009 American Control Conference (2009).

[6] DTU Wind Energy. HAWC2. www.https://hawc2.dk/. Accessed: 2025-01-23. 2025.

[7] Taeseong Kim et al. "Development of an anisotropic beam finite element for composite wind turbine blades in multibody system". In: Renewable Energy Journal (2013).

[8] Shuaishuai Wang et al. "Effects of bedplate flexibility on drivetrain dynamics: Case study of a 10 MW spar type floating wind turbine". In: Renewable Energy Journal (2020).

[9] Shuaishuai Wang et al. "On Initial Design and Modelling of a 10 MW Medium Speed Drivetrain for Onshore Wind Turbines". In: Phys.: Conf. Ser. 1356 012024 (2019).

[10] Orla Donnelly et al. "Analysing the cost impact of failure rates for the next generation of offshore wind turbines". In: Wind Energy Journal (2024).

[11] Michiel Zaaijer et al. Introduction to Wind Turbines: Physics and Technology. University Script. 2023.

[12] Herbert Wittel et al. Roloff/Matek: Maschinenelemente. Normung, Berechnung, Gestaltung. German. 26. Auflage. Springer Vieweg, 2023.

[13] Yi Guo et al. "Improving Wind Turbine Drivetrain Reliability Using a Combined Experimental, Computational, and Analytical Approach". In: National Renewable Energy Laboratory (2014).

[14] Y. Guo et al. "A Systems Engineering Analysis of Three-Point and Four-Point Wind Turbine Drivetrain Configurations". In: Wind Energy Journal (2010).

[15] Edward Hart et al. "Wind turbine main-bearing loading and wind field characteristics". In: Wind Energy 22.11 (2019), pp. 1534–1547. DOI: https://doi.org/10.1002/we.2386. eprint: https://onlinelibrary.wiley.com/doi/pdf/10.1002/we.2386. URL: https://onlinelibrary.wiley.com/doi/abs/10.1002/we.2386.

[16] Edward Hart. "Developing a systematic approach to the analysis of time-varying main bearing loads for wind turbines". In: Wind Energy Journal (2020).

[17] Vincenzo Vullo. Gears - Volume 1: Geometric and Kinematic Design. Springer, 2020.

[18] Erich Hau. Windkraftanlagen: Grundlagen, Technik, Einsatz, Wirtschaftlichkeit. German. 6. Auflage. Springer Vieweg, 2016.

[19] Trevor M. Letcher. Wind Energy Engineering: A Handbook for Onshore and Offshore Wind Turbines. Second Edition. Academic Press, 2023.

[20] J. Gallego-Calderon. Electromechanical drivetrain simulation. PhD Thesis. 2015.

[21] Saeid Fadaei et al. "A Survey of Numerical Simulation Tools for OffshoreWind Turbine Systems". In: Wind (2024).

[22] Shuaishuai Wang et al. "On design, modelling, and analysis of a 10-MWmedium-speed drivetrain for offshore wind turbines". In: Wind Energy (2020).

[23] Veronica Liverud Krathe et al. "Investigation of Main Bearing Fatigue Estimate Sensitivity to Synthetic Turbulence Models Using a Novel Drivetrain Model Implemented in OpenFAST". In: Authorea (Aug. 2024).

[24] IEA Wind Systems. IEA Wind Systems - Github Repository for Reference Wind Turbines. https://github.com/IEAWindSystems. Accessed: 2025-01-30. 2025.

[25] Pietro Bortolotti et al. IEA Wind Task 37 on Systems Engineering in Wind Energy – WP2.1 Reference Wind Turbines. Tech. rep. International Energy Agency, 2019. url: https://www.nrel.gov/docs/fy19osti/73492.pdf.

[26] Evan Gaertner et al. Definition of the IEA 15-Megawatt Offshore Reference Wind Turbine. Tech. rep. International Energy Agency, 2020. url: https://www.nrel.gov/docs/fy20osti/75698.pdf.

[27] Frederik Zahle et al. Definition of the IEA Wind 22-Megawatt Offshore Reference Wind Turbine. Tech. rep. DTU Wind Report E-0243, https://doi.org/10.11581/DTU.00000317. Technical University of Denmark, International Energy Agency, 2024.

[28] Christian Bak et al. Description of the DTU 10 MW Reference Wind Turbine. Tech. rep. DTU Wind Energy Report-I-0092, https://orbit.dtu.dk/files/55645274/The_DTU_10MW_Reference_Turbine_Christian_Bak.pdf. Risø National Laboratory - Technical University of Denmark, 2013.

[29] J. Jonkman et al. Definition of a 5-MW reference wind turbine for offshore system development. Tech. rep. Technical Report NREL/TP-500-38060, https://www.nrel.gov/docs/fy09osti/38060.pdf. NREL, 2009.

[30] Shuaishuai Wang et al. "Effects of elastic support on the dynamic behaviors of the wind turbine drive train". In: Frontiers of Mechanical Engineering (2017).

[31] Wind Energy Generation Systems - Part 1: Design Requirements. IEC 61400-1:2019. 2019. url: https://webstore.iec.ch/en/publication/26423.

[32] Andreas Öchsner. Classical Beam Theories of Structural Mechanics. Springer, 2021.

[33] O. Gözcü et al. "The effects of blade structural model fidelity on wind turbine load analysis and computation time". In: Wind Energy Science (2020).

[34] Torben J. Larsen et al. How 2 HAWC2, the user's manual. Software Manual. 2023.

[35] Helge Aagaard Madsen et al. "Implementation of the blade element momentum model on a polar grid and its aeroelastic load impact". In: Wind Energy Science (2020).

[36] Francisco Oyague. Gearbox modeling and load simulation of a baseline 750-kW wind turbine using state-of-the-art simulation codes. Tech. rep. Technical Report NREL/TP-500-41160, https://www.nrel.gov/docs/fy09osti/ NREL, 2009.

[37] Dassault Systemès. SIMULINK software. https://www.3ds.com/products/simulia/simpack. Accessed: 2025-04-27. 2025.

[38] Dassault Systemès. SOLIDWORKS software. https://www.solidworks.com/. Accessed: 2025-04-28. 2025.

[39] Microsoft. VS Code. https://code.visualstudio.com/. Accessed: 2025-04-28. 2025.

[40] DTU Wind Energy. Tools. https://tools.windenergy.dtu.dk/home/. Accessed: 2025-01-30. 2025.

[41] G. R. Cowper. "The shear coefficient in Timoshenko's beam theory". In: Journal of Applied Mechanics 33.2 (1966), pp. 335–340.

[42] Robert D. Bitsche. An Introduction to Beam Cross Section Stiffness and Mass Properties. https://learn.inside.dtu.dk/d2l/le/content/24818/Home. Lecture notes, HAWC2 Selfstudy, Technical University of Denmark.

Appendix
A. Extra Figures

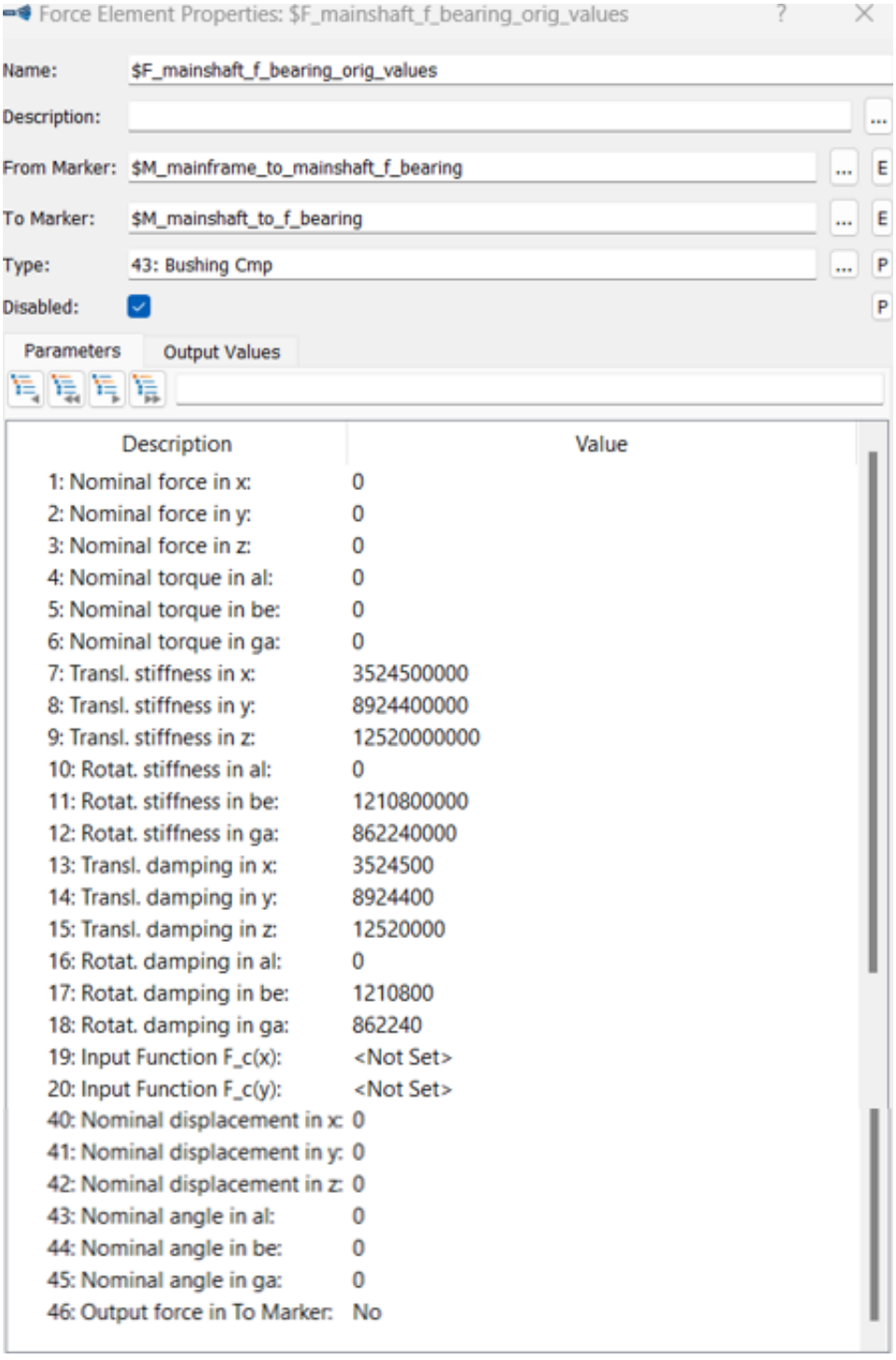

Figure 67: SIMPACK main bearing force element - Bushing Cmp.

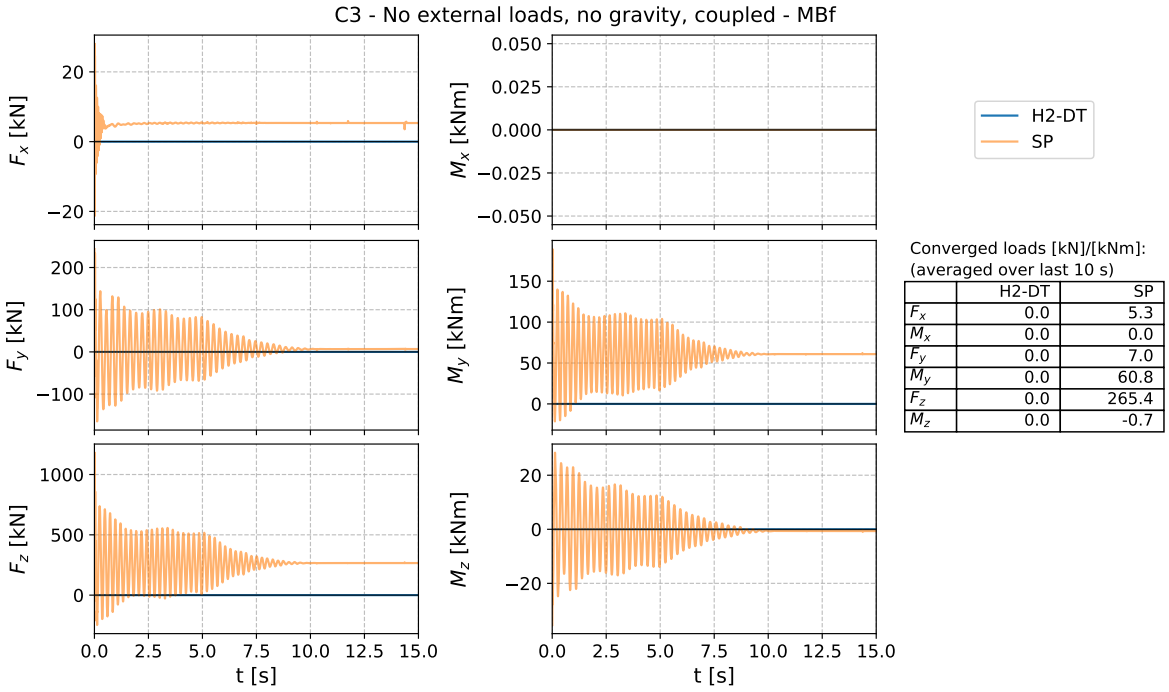

	H2-DT	SP
F_x	0.0	5.3
M_x	0.0	0.0
F_y	0.0	7.0
M_y	0.0	60.8
F_z	0.0	265.4
M_z	0.0	-0.7

Figure 68: Front main bearing residual forces and moments for the coupled drivetrain.

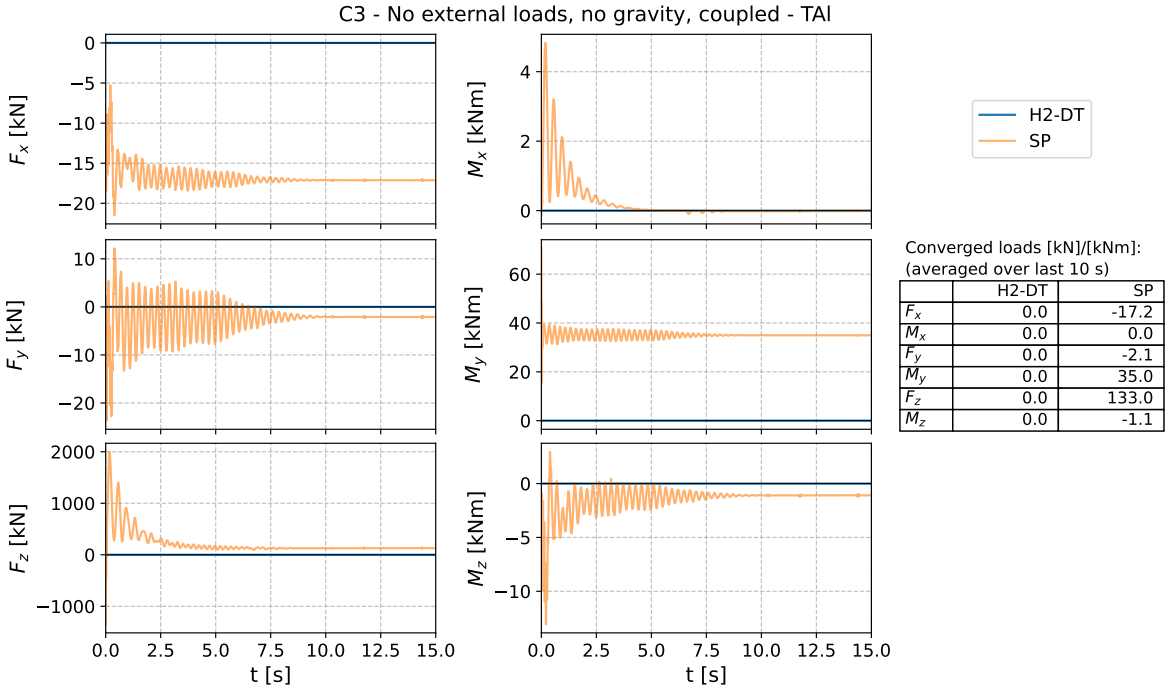

	H2-DT	SP
F_x	0.0	-17.2
M_x	0.0	0.0
F_y	0.0	-2.1
M_y	0.0	35.0
F_z	0.0	133.0
M_z	0.0	-1.1

Figure 69: Left torque arm residual forces and moments for the coupled drivetrain.

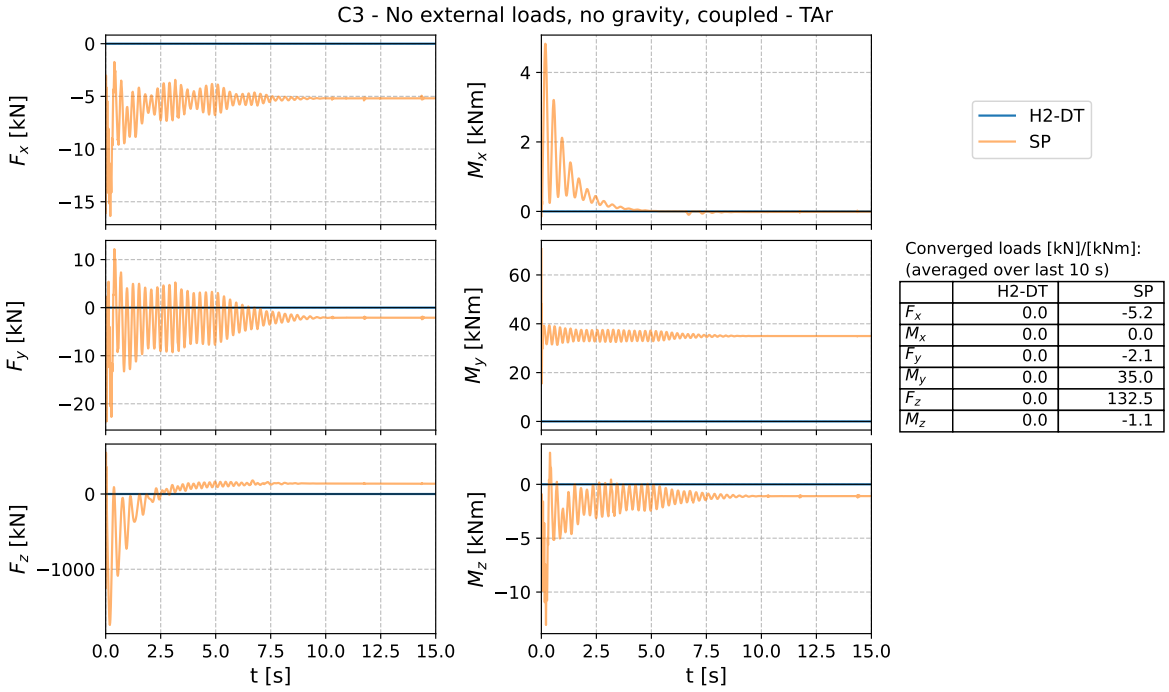

	H2-DT	SP
F_x	0.0	-5.2
M_x	0.0	0.0
F_y	0.0	-2.1
M_y	0.0	35.0
F_z	0.0	132.5
M_z	0.0	-1.1

Figure 70: Right torque arm residual forces and moments for the coupled drivetrain.

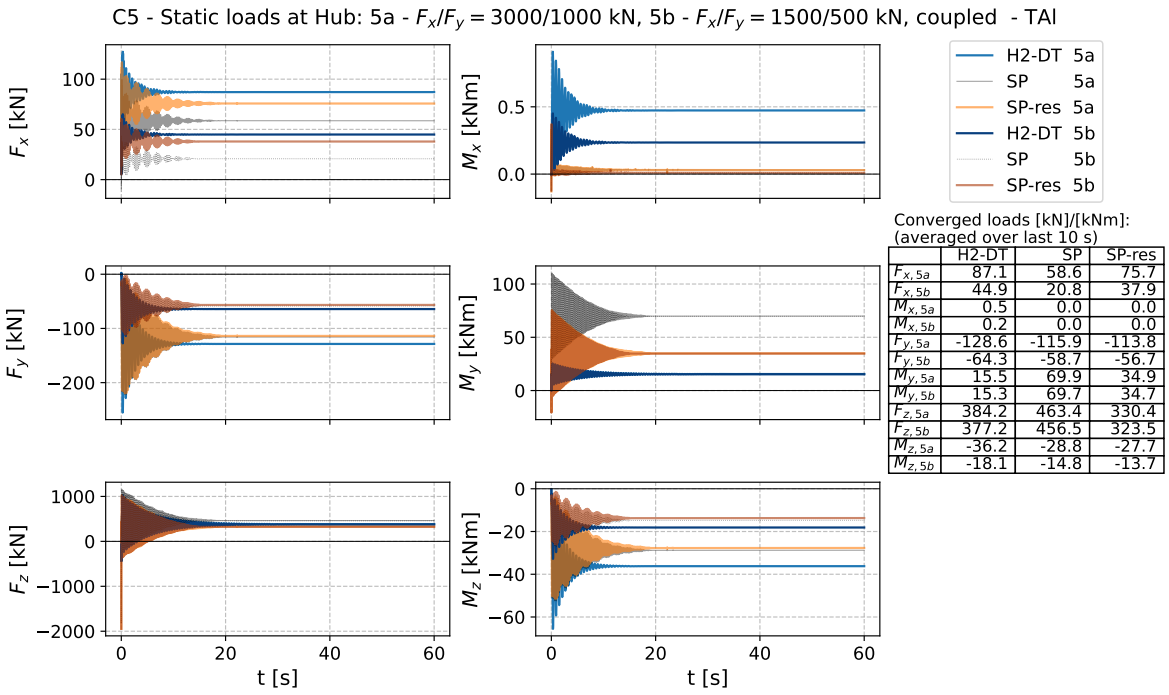

	H2-DT	SP	SP-res
$F_{x,5a}$	87.1	58.6	75.7
$F_{x,5b}$	44.9	20.8	37.9
$M_{x,5a}$	0.5	0.0	0.0
$M_{x,5b}$	0.2	0.0	0.0
$F_{y,5a}$	-128.6	-115.9	-113.8
$F_{y,5b}$	-64.3	-58.7	-56.7
$M_{y,5a}$	15.5	69.9	34.9
$M_{y,5b}$	15.3	69.7	34.7
$F_{z,5a}$	384.2	463.4	330.4
$F_{z,5b}$	377.2	456.5	323.5
$M_{z,5a}$	-36.2	-28.8	-27.7
$M_{z,5b}$	-18.1	-14.8	-13.7

Figure 71: Left TA forces and moments for the coupled drivetrain and different static external loads.

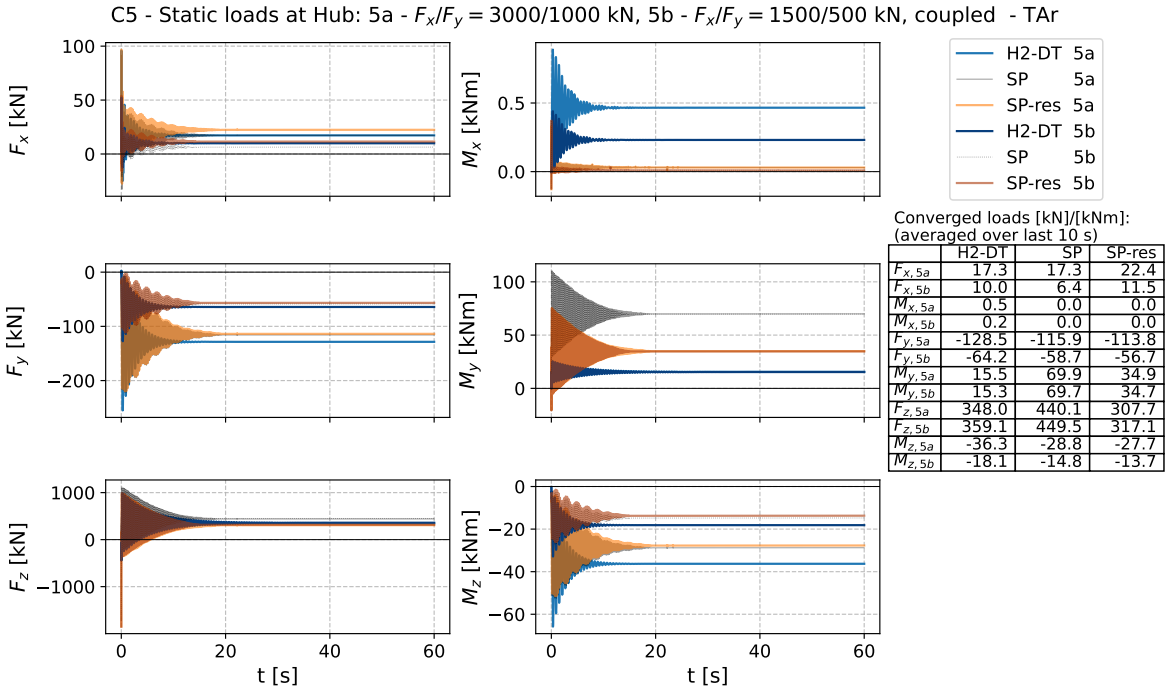

	H2-DT	SP	SP-res
$F_{x,5a}$	17.3	17.3	22.4
$F_{x,5b}$	10.0	6.4	11.5
$M_{x,5a}$	0.5	0.0	0.0
$M_{x,5b}$	0.2	0.0	0.0
$F_{y,5a}$	-128.5	-115.9	-113.8
$F_{y,5b}$	-64.2	-58.7	-56.7
$M_{y,5a}$	15.5	69.9	34.9
$M_{y,5b}$	15.3	69.7	34.7
$F_{z,5a}$	348.0	440.1	307.7
$F_{z,5b}$	359.1	449.5	317.1
$M_{z,5a}$	-36.3	-28.8	-27.7
$M_{z,5b}$	-18.1	-14.8	-13.7

Figure 72: Right TA forces and moments for the coupled drivetrain and different static external loads.

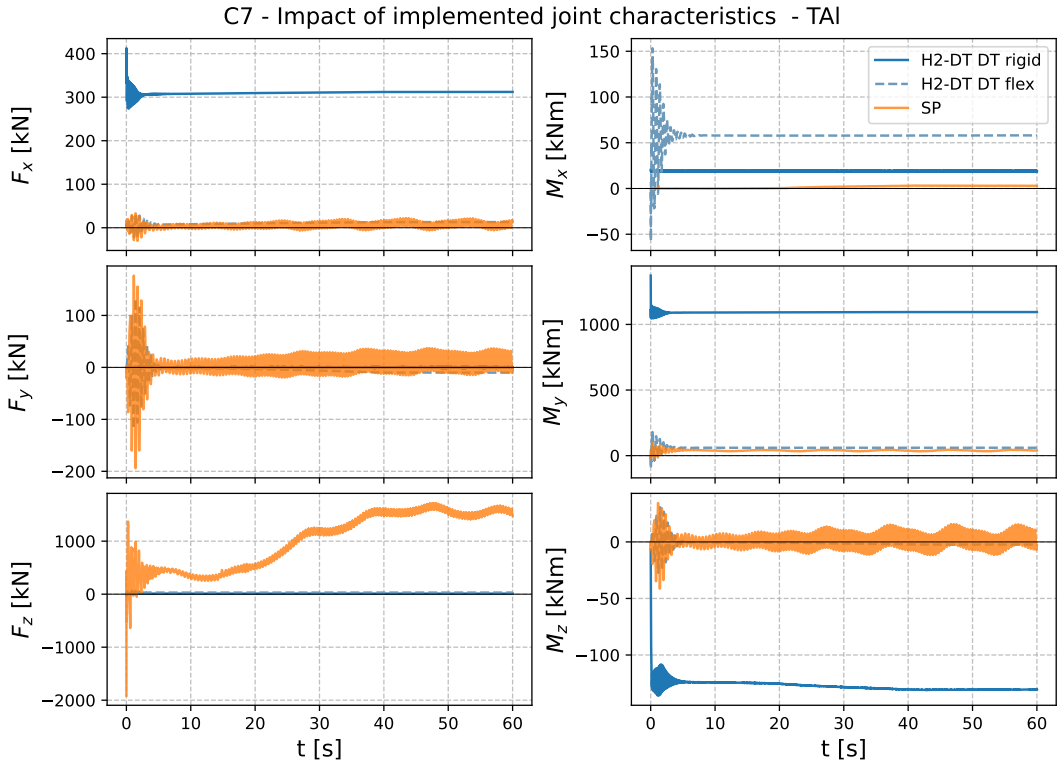

Figure 73: Comparison of rigid and flexible drivetrain structure for left torque arm, a rigid tower, and rigid blades.

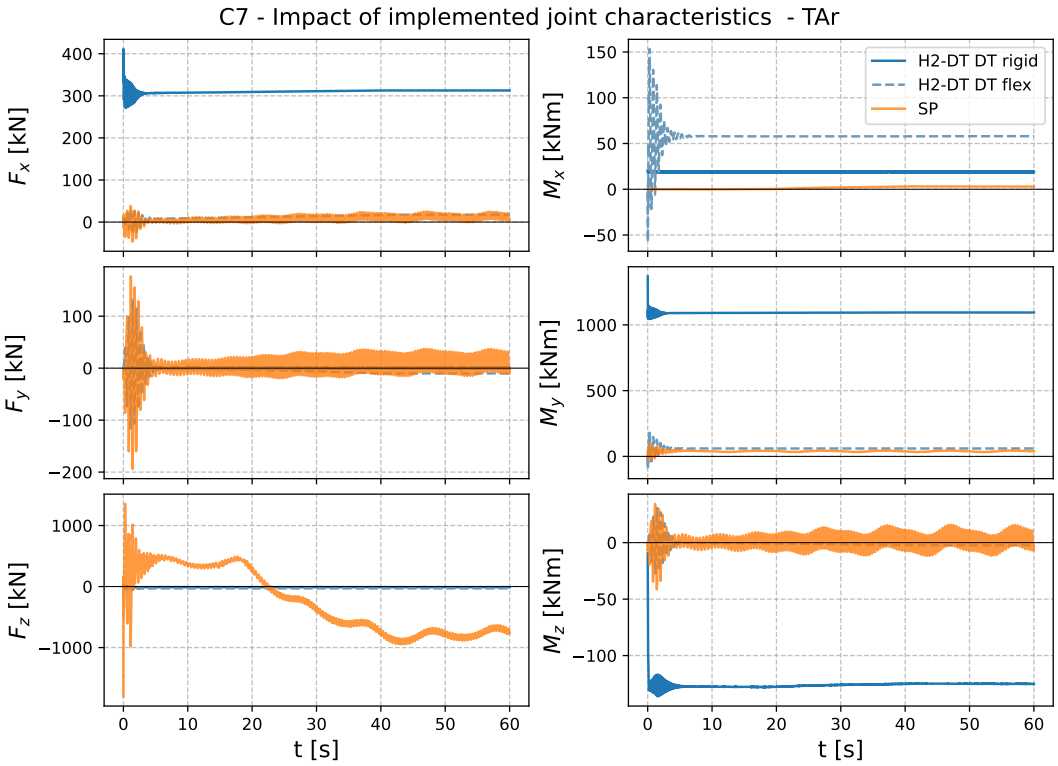

Figure 74: Comparison of rigid and flexible drivetrain structure for right torque arm, a rigid tower, and rigid blades.

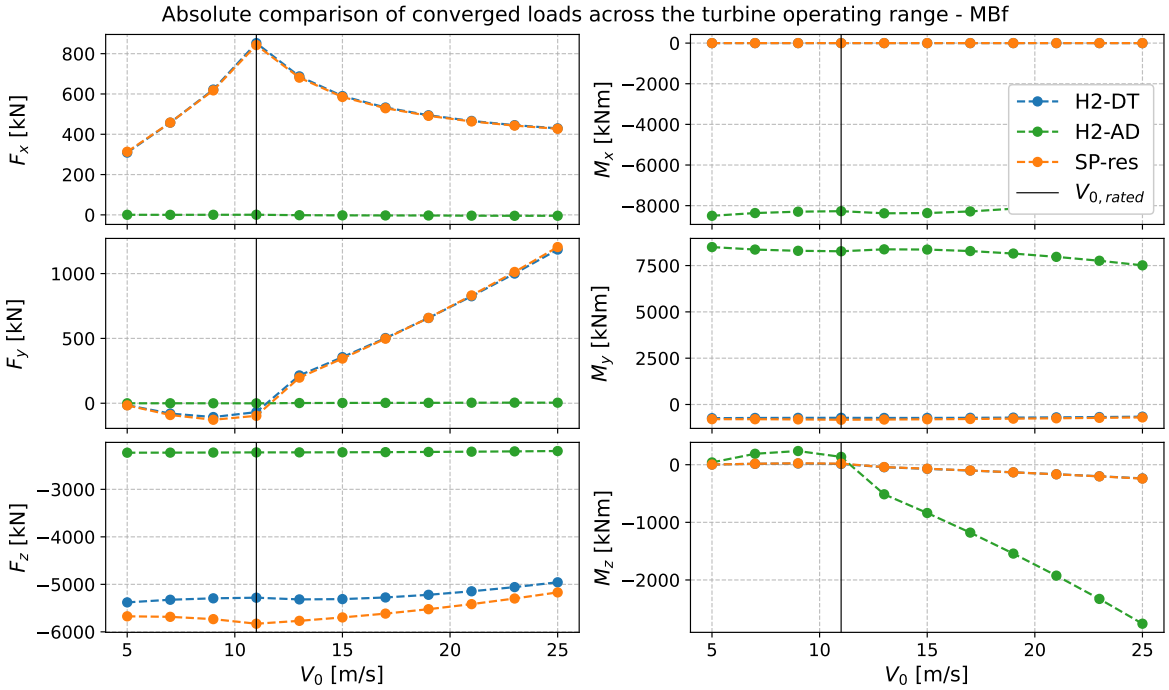

Figure 75: Absolute comparison of MBf loads across turbine operating range, including the results from the adjusted HAWC2 model.

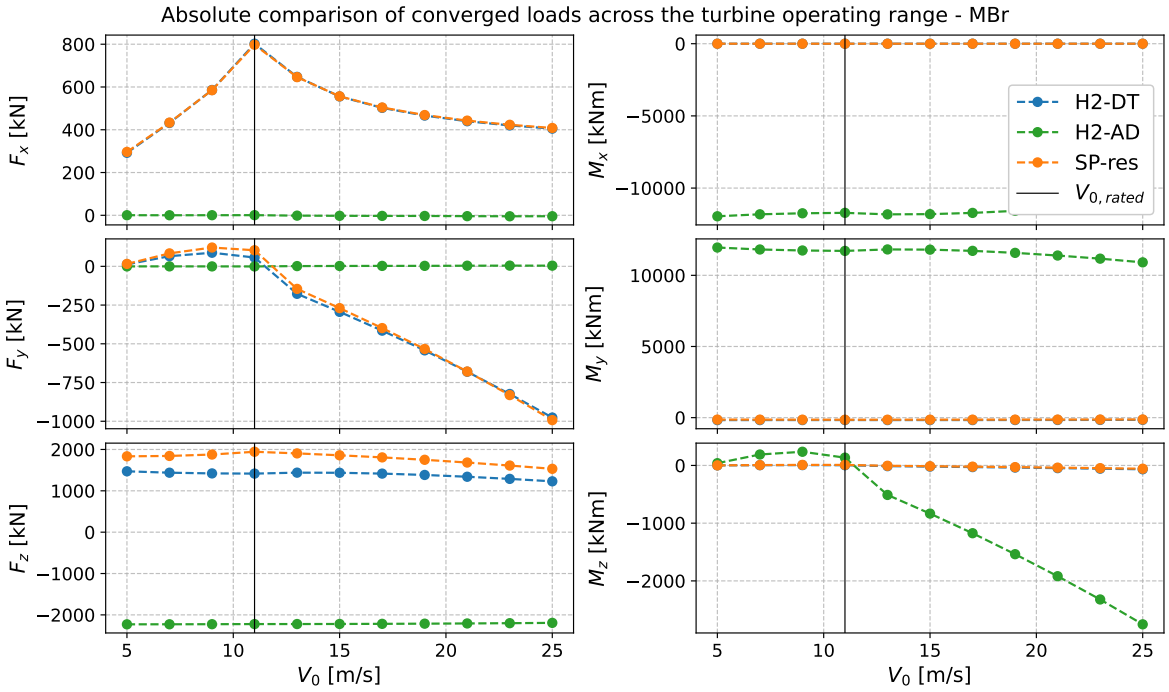

Figure 76: Absolute comparison of MBr loads across turbine operating range, including the results from the adjusted HAWC2 model.

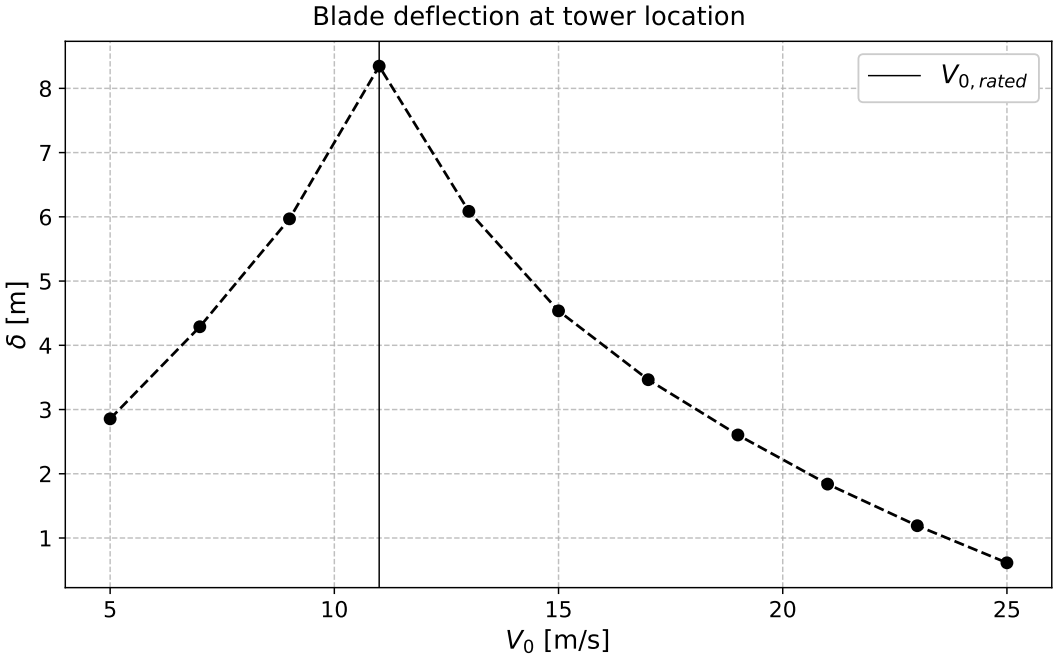

Figure 77: Blade deflection at the azimuthal position of the tower: $\delta = TC_{rigid} - TC_{flex}(V_0)$

B. Extra Tables

Table 19: Comparison of DFIG with Partial Power Converter and PMSG with Full Power Converter [4]

Type	**DFIG with Partial Power Converter**	**PMSG with Full Power Converter**
Power Range	Common for medium-sized turbines (3–6 MW)	Increasingly common for large turbines (5–10 MW)
Rotor Magnetic Field	Generated using rotor currents	Produced using permanent magnets
Converter Type	Partial power converter (30–40% of total power)	Full power converter (100% of total power)
Efficiency	Lower due to rotor Joule losses	Higher due to the absence of rotor Joule losses
Maintenance	Requires carbon brushes and slip rings, which need frequent inspection and replacement	Avoids carbon brushes and slip rings, reducing maintenance

Table 20: Applied aerodynamic models in HAWC2 [6]

Model	**Key Features**
Dynamic Inflow	Accounts for fast changes in rotor load by correcting the induced velocity.
Skew Inflow	Implements corrections for skewed wake effects due to non-axisymmetric inflow.
Shear Effect on Induction	Applies a linear interpolation of Ct to account for shear effects.
Effect from Large Blade Deflections	Considers the impact on the dynamics if the rotor diameter changes due to large blade deflections.
Tip Loss	Accounts for the reduction in lift at the tip of the blades resulting from pressure-driven air flow.
Dynamic Stall	Considers non-linear effects caused by rapid changes in angle of attack (stall separation lag, shed vorticity from the trailing edge, etc.).
Near Wake Model	Combines lifting-line near wake model with far wake model from the BEM theory to improve the dynamic blade loading under all conditions.